Unveiling the heart of (U)LIRGs with high-angular resolution radio observations

Memoria presentada por

Cristina Romero Cañizales

realizada en el Instituto de Astrofísica de Andalucía, Consejo Superior de Investigaciones Científicas, bajo la dirección de

Antonio Alberdi Odriozola & Miguel Ángel Pérez Torres,

para optar al grado de Doctora en Física y Matemáticas

Departamento de Física Teórica y del Cosmos
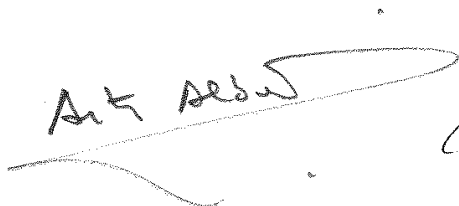
Granada, 18 de noviembre de 2011.

ANTONIO ALBERDI ODRIOZOLA, Profesor de Investigación del Instituto de Astrofísica de Andalucía, Consejo Superior de Investigaciones Científicas, y

MIGUEL ÁNGEL PÉREZ TORRES, Científico Titular del Instituto de Astrofísica de Andalucía, Consejo Superior de Investigaciones Científicas,
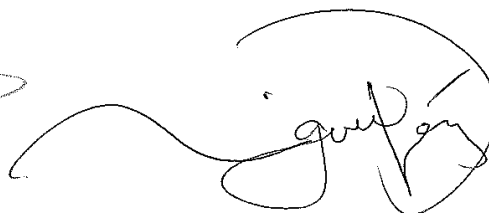
CERTIFICAN:

Que la presente memoria: *Unveiling the heart of (U)LIRGs with high-angular resolution radio observations* ha sido realizada en el Instituto de Astrofísica de Andalucía, Consejo Superior de Investigaciones Científicas por Cristina Romero Cañizales bajo nuestra dirección, y constituye su Tesis Doctoral para optar al grado de Doctora en Física y Matemáticas.

Granada, 18 de octubre de 2011

Fdo. Antonio Alberdi Odriozola   Fdo. Miguel Ángel Pérez Torres

Probablemente sin entender mis historias de estrellas lejanas, siempre estuviste orgullosa de mí. A ti va dedicada esta tesis, mamá.

Resumen

La muerte de estrellas de masa similar o mayor que 8 $M_\odot$ está marcada por su explosión como supernovas de colapso gravitatorio (CCSNe). Dado que la vida de estrellas masivas es mucho más corta que la edad del Universo, la tasa a la que explotan puede utilizarse como un trazador directo de la tasa de formación estelar actual en la galaxia anfitriona. A su vez, midiendo la tasa de formación estelar en galaxias a diferentes corrimientos al rojo, será posible trazar la historia de la formación estelar en el Universo. Es por ello que la detección de supernovas de colapso gravitatorio es una tarea crucial. En particular, el estudio de galaxias luminosas (LIRGs: $L_{IR} > 10^{11}$ $L_\odot$) y ultra-luminosas (ULIRGs: $L_{IR} > 10^{12}$ $L_\odot$) en el infrarrojo es de suma importancia para alcanzar este objetivo, ya que gran parte de la formación de estrellas masivas a altos corrimientos al rojo tuvo lugar en dichas galaxias.

En la mayoría de (U)LIRGs, los intensos brotes de formación estelar están concentrados en las regiones nucleares y circunnucleares, y en muchos casos están acompañados por la presencia de núcleos activos de galaxias (AGNs), que en conjunto son responsables del calentamiento del polvo en (U)LIRGs. Por un lado se tiene que la detección de CCSNe, o incluso de un AGN, está limitada en longitudes de onda del óptico y del infrarrojo principalmente por la presencia de polvo y, por otro lado, la emisión de CCSNe en longitudes de onda de radio (que no tiene problemas de absorción), es más potente en regiones densas, ya que es generada por la interacción del viento pre-supernova con el medio circunestelar. Por lo tanto, una CCSN que explota en regiones alejadas al núcleo (regiones galácticas y circumnucleares), será más fácilmente detectada en el óptico/infrarrojo, mientras que una CCSN que explota en las regiones nucleares (y circumnucleares, si la densidad del gas es alta), es susceptible de ser detectada en longitudes de onda de radio. En esta memoria se ha resaltado la importancia de usar técnicas complementarias (por ejemplo, observaciones en radio e infrarrojo) para estimar tasas completas de explosión de CCSNe, que a su vez nos lleven a determinar con mayor precisión la tasa de formación estelar en las galaxias anfitrionas.

La presente tesis versa sobre el estudio de las (U)LIRGs, con el objetivo de lograr un mayor entendimiento sobre la conexión entre los brotes de formación estelar y la actividad

RESUMEN

AGN en los núcleos de estas galaxias, así como de la contribución de ambas componentes al calentamiento del polvo. El trabajo realizado está orientado al estudio de las regiones más internas de las (U)LIRGs, donde tanto gas como polvo se encuentran en grandes cantidades, por lo que las observaciones a longitudes de onda de radio son idóneas al estar exentas de problemas de extinción.

Una de las contribuciones científicas de la presente tesis al estudio de las (U)LIRGs ha sido la detección directa e indirecta de CCSNe en las regiones nucleares de dichas galaxias. Utilizando la red interferométrica del EVN (European VLBI Network), se descubrieron factorías de supernovas en dos LIRGs cercanas: IC 694 (también llamada Arp 299-A, es el núcleo más brillante del sistema de galaxias denominado Arp 299) a 45 Mpc de distancia, cuya factoría se revela en nuestras observaciones como muy prolífica, e IC 883 a 100 Mpc. En convivencia con el intenso brote de formación estelar, en ambas galaxias se detectaron también AGNs de baja luminosidad. Estos resultados representan un paso importante en la determinación del mecanismo dominante del calentamiento del polvo en (U)LIRGs, ya que sólo en las galaxias más cercanas es posible resolver la emisión difusa y detectar sus componentes compactas; de hecho, el número de factorías de supernovas reportado actualmente en la literatura, es muy bajo. Es de resaltar el descubrimiento de un brote de formación estelar en la galaxia IC 883, dado que observaciones interferométricas de muy larga base (VLBI) realizadas en el pasado, lograron solamente inferir la existencia del AGN. Esto se debe probablemente a la baja sensibilidad de dichas observaciones.

Con datos de archivo del VLA (Very Large Array), hemos realizado un estudio piloto en los núcleos del sistema en interacción Arp 299 con el fin de dar un paso adelante y detectar indirectamente la explosión de supernovas. Mediante el monitoreo de la densidad de flujo del núcleo de una galaxia, es posible separar la emisión difusa de la emisión proveniente de las componentes compactas (por ejemplo supernovas). Con este método, estimamos la tasa de explosión de CCSN en uno de los núcleos de Arp 299 (B1). Este trabajo abre una vía de investigación muy interesante para el futuro, ya que podrá explotarse la alta sensibilidad de nuevos instrumentos, al permitir la determinación de tasas de explosión de CCSN en galaxias que no pueden ser resueltas a la más alta resolución posible.

En este trabajo, extendemos nuestro estudio a las ULIRGs más brillantes y más lejanas del Universo local. Presento en esta tesis los resultados de tres épocas de observaciones de IRAS 23365+3604 ($D = 252$ Mpc) con el EVN realizadas simultáneamente a dos frecuencias. Las imágenes presentadas son las más profundas y con mayor resolución jamás obtenidas de dicha galaxia. Aunque no es posible resolver la emisión difusa, nuestras observaciones han revelado la naturaleza mixta de su núcleo a través de las mediciones de luminosidad, temperatura de brillo, y evolución del índice espectral. Hasta un radio de 50 pc aproximadamente, el núcleo está dominado por brotes de formación estelar y posible-

mente de un AGN; a partir de ahí y hasta un radio de 100 pc, domina una población más envejecida de emisores en radio, probablemente remanentes de supernova (SNR). Además, hemos encontrado que la vida de la fuente en radio está limitada por pérdidas de radiación, por lo que la reaceleración, o la inyección de nuevos electrones, resulta necesaria. Dado que la magnitud del campo magnético que encontramos tanto a escalas nucleares como galácticas, es similar a la estimada para otras ULIRGs en estado avanzado de fusión, concluimos que el escenario de reaceleración/inyección necesaria de electrones, debe ser común para este tipo de galaxias, como sugiere la existencia de SNe y SNRs en las zonas nucleares.

Presento también en esta tesis nuestras observaciones de emisión máser de vapor de agua en LIRGs que se sabe contienen un AGN: Arp 299 (núcleos A y B1) y NGC 7469. Los máseres de agua extragalácticos con luminosidades superiores a 10 $L_\odot$, son excelentes trazadores de chorros o discos, cuya presencia está relacionada con actividad AGN. Las observaciones hacia Arp 299 han supuesto un gran reto, tanto por la complejidad de la técnica usada (VLBI) como por la debilidad intrínseca de la línea que intentábamos detectar (~ 3.5 mJy). Complicaciones técnicas con las antenas utilizadas en las observaciones, han resultado en una baja calidad de los datos, por lo que las observaciones no cumplieron los objetivos planteados. Este proyecto continúa y estamos a la espera de una nueva época de observación. En el caso de NGC 7469, nuestras observaciones con el telescopio de 100 m de Effelsberg representaron un intento más por detectar vapor de agua en esta galaxia, mejorando en un factor tres la sensibilidad de observaciones previas. Recientemente se propuso que la no-detección de vapor de agua en galaxias de tipo Seyfert 1 (como NGC 7469) se debía a la baja sensibilidad de las observaciones hasta ahora realizadas. Nuestras observaciones demuestran que incluso con una alta sensibilidad no es suficiente, por lo que la detección podría estar limitada principalmente por la inclinación propia de las galaxias Seyfert 1, de manera que de haber emisión máser de agua, no se tiene ninguna componente en nuestra línea de visión y por lo tanto dicha emisión no es detectable.

En esta tesis se han aprovechado al máximo diferentes instrumentos con el objetivo de contribuir al entendimiento de (U)LIRGs en general, pero también se han marcado vías de acción de cara al advenimiento de nuevos instrumentos con los que se pretende el estudio de galaxias luminosas en el infrarrojo a distancias cosmológicas.

CONTENTS

CONTENTS

List of acronyms and abbreviations

LIST OF ACRONYMS AND ABBREVIATIONS

Abstract

This thesis contributes to the study of luminous (LIRGs: $L_{\mathrm{IR}} > 10^{11}$ L$_\odot$) and ultra luminous (ULIRGs: $L_{\mathrm{IR}} > 10^{12}$ L$_\odot$) infrared galaxies, with the aid of high angular resolution, high sensitivity radio observations. The aim is to gain insight into the dominant dust heating mechanism (star formation and/or an AGN) in these galaxies.

The work presented here has emphasized the need of using complementary techniques (such as near-IR and radio observations) if we are to obtain complete core-collapse supernova (CCSN) rates in (U)LIRGs, which yield more accurate star formation rates (SFRs) in the host galaxies. This is because near-IR observations are more likely to aid in the detection of CCSNe in regions with low gas density which are not heavily affected by dust extinction, whereas radio observations are of better use when attempting CCSN detections in dense gas regions, regardless of the dust extinction. However, this thesis focuses on the study of the innermost nuclear and circumnuclear regions of (U)LIRGs, for which the use of radio observations results ideal.

One of the scientific contributions of the present thesis to the study of (U)LIRGs has been the direct and indirect detection of CCSNe in the nuclear regions of such galaxies. Radio observations with the European very long baseline interferometry Network (EVN) have allowed the discovery of supernova factories in two nearby LIRGs: Arp 299-A (which has proved to be more prolific than previously thought) at a distance of 45 Mpc, and IC 883 at 100 Mpc. In coexistence with the intense star formation, we have also detected a low-luminous AGN in each of these two galaxies. These results represent an important step in determining the dominant heating mechanism of dust in (U)LIRGs, since milliarcsec resolution observations are able to resolve out the diffuse emission (thus unveiling compact sources, e.g., SNe) of only the nearest galaxies. The discovery in IC 883 is particularly outstanding, since previous VLBI observations were only able to infer the existence of an AGN compact component, likely because of low sensitivity.

Making use of archival VLA (Very Large Array) data, we have performed a pilot study in the nuclei of the interacting system Arp 299, aimed at detecting indirectly CCSN explosions. We have monitored the flux density variations, and were able to separate the contribution of the diffuse emission from that arising from compact components (e.g., SNe).

Abstract

Thus, we could estimate the CCSN rate in one of the nuclei of Arp 299. This simple technique can be of use to determine CCSN rates in distant galaxies that cannot be resolved into individual components even at the highest possible resolution.

I also present our results from three epochs of EVN observations made simultaneously at two different frequencies, of IRAS 23365+3604 ($D = 252$ Mpc), one of the brightest and farthest ULIRGs in the local Universe. We have obtained the deepest and highest resolution radio images ever of this galaxy. Even though it is not possible to resolve the diffuse emission of this galaxy, our observations have revealed the mixed nature of its nucleus (starburst-AGN) via its luminosity, brightness temperature and evolution of its spectral index distribution. We have additionally analysed complementary Multi-Element Radio Linked Interferometry Network (MERLIN) and archival Very Large Array (VLA) data. We have found that radiation losses in this galaxy are important, indicating that re-acceleration and/or replenishment of new electrons is necessary. The magnetic field strength we have estimated at both nuclear and galactic scales is typical for galaxies in advanced mergers, suggesting that radiation losses must be important in this kind of ULIRGs, and that re-acceleration/replenishment mechanisms must exist (such as SNe and SNRs).

We have performed water maser emission observations in an attempt to trace and characterize the AGN activity (in the form of disks or jets) in the nuclear regions of two LIRGs (Arp 299 and NGC 7469) known to contain an AGN. The observations towards Arp 299 have proved to be very challenging due to the complexity of the technique we used (VLBI), and the requirement of very high sensitivity in order to detect the feeble emission ($\sim$ 3.5 mJy). No detections were achieved. In the case of NGC 7469, we attempted the detection of water maser emission with Effelsberg 100 m telescope observations. We improved the sensitivity achieved in previous observations by a factor of three. Our non-detection suggests that sensitivity has not been the limiting factor hampering water maser emission detection towards Seyfert 1 galaxies, as argued in other studies.

The work presented in this thesis has greatly profited from current radio facilities, contributing to a general understanding of (U)LIRGs. At the same time, it offers new paths to the detection of CCSN in distant supernova host galaxies, which cannot be resolved at the highest angular resolution.

CHAPTER I

INTRODUCTION

This thesis deals with the study of very luminous infrared (IR) galaxies which, due to extreme conditions, display intense star formation (SF), in particular, massive SF. In this chapter, I introduce some basic properties of these interesting galaxies, towards an understanding of the results presented in the following chapters.

I.1   The beacons of star formation rate

Star formation is a common phenomenon among galaxies having large reservoirs of gas, and meeting the physical conditions (e.g., density and pressure) to turn the gas into stars. Different processes regulate the number of stars formed, their masses, and the rate at which they are formed within each galaxy.

Whilst long-lived (a few tens of Myr up to a few Gyr), low and intermediate mass stars ($M_{\mathrm{init}} < 8$ M$_\odot$) basically lock up the gas and prevent a rapid recycling of material, short-lived (up to a few tens of Myr), massive stars ($M_{\mathrm{init}} \gtrsim 8$ M$_\odot$) can control the evolution of their host galaxy. The powerful wind of massive stars and the ejected material as they die in supernova (SN) events can replenish the galaxy with energy, momentum and new materials, which can be reprocessed. Furthermore, the shock waves created by the wind of massive stars, can trigger the formation of new molecular clouds whose physical and chemical conditions will control the nature and the formation rate of new generations of stars, the possible formation of planetary systems and the evolution of the host galaxy.

Due to their short lifetimes, massive stars can be used as tracers of the current rate at which gas from the interstellar medium (ISM), per unit volume and per unit time, is converted into stars in their host galaxies, i.e., the star formation rate (SFR). Massive stars tend to form in clusters, and their cradles are very obscured regions. In practical grounds, it is very difficult to count the number of massive stars in a galaxy; hence, alternative tracers are used to infer their presence and to probe the SFR.

Different SFR tracers involve the use of observations at different wavelengths with their own advantages and disadvantages. For instance, the integrated colours and optical spectra are required to estimate/assume reliable values for the extinction towards the zones where SF is taking place, the metallicity, etc. (see e.g., Kennicutt, 1983; Moustakas *et al.*, 2006). Emission lines in the mid-infrared (MIR) are being used as SFR indicators (see e.g., Peeters *et al.*, 2004; Calzetti *et al.*, 2007; Pereira-Santaella *et al.*, 2010), however MIR emission due to massive SF might be contaminated by non-ionizing stellar populations and from active galactic nucleus (AGN) emission. Rosa-González *et al.* (2002) have reviewed different SFR estimators covering wavelengths from the ultraviolet (UV) up to the far-infrared (FIR). More recently, Murphy *et al.* (2011) have assessed the reliability of different SFR estimators, and compared them against the thermal radio emission at 33 GHz for the nearby galaxy NGC 6946. One of their findings, is that the different estimators behave differently in the nuclear and extra-nuclear regions, probably due to extinction effects.

At radio and near-infrared (NIR) wavelengths, massive SF can be traced via core-collapse supernova (CCSN) detections. However, CCSN emission might be heavily affected by dust extinction, thus hindering its detection in the NIR. On the other hand, not all CCSNe will necessarily result in bright radio supernova (RSN) events (see §I.1.1.2).

IR ($L_{\mathrm{IR}} = L[8\text{--}1000\,\mu\mathrm{m}]\,\mathrm{L}_\odot$) and FIR ($L_{\mathrm{FIR}} = L[40\text{--}400\,\mu\mathrm{m}]\,\mathrm{L}_\odot$) luminosities, scale with the rate at which CCSNe explode (ν_{SN}), and thus can also serve as SFR estimators. For example, Mattila and Meikle (2001) found an empirical relation between L_{IR} and ν_{SN} for galaxies with intense SF,

$$\left(\frac{\nu_{\mathrm{SN}}}{\mathrm{yr}^{-1}}\right) = 2.7 \times 10^{-12} \times \left(\frac{L_{\mathrm{IR}}}{\mathrm{L}_\odot}\right). \tag{I.1}$$

A similar relation between L_{FIR} and ν_{SN} is found from the relations given by Condon (1992) between ν_{SN} and SFR of massive stars, and between the latter and L_{FIR}, resulting in

$$\left(\frac{\nu_{\mathrm{SN}}}{\mathrm{yr}^{-1}}\right) \sim 3.7 \times 10^{-12} \times \left(\frac{L_{\mathrm{FIR}}}{\mathrm{L}_\odot}\right). \tag{I.2}$$

However, none of these relations account for the presence of an AGN, which could in principle contribute to either luminosity. Therefore, the previous estimates should be considered as upper limits

Besides of the inherent systematic errors associated with the different assumptions made in all cases, a reliable birthrate of stars with different masses (m) at a given time is also needed, i.e., the initial mass function (IMF),

$$\Phi(m) \propto \frac{\mathrm{d}N}{\mathrm{d}m},$$

for which several models are available (e.g., Salpeter, 1955; Kroupa, 2001, etc.). Assumptions made on the IMF, further contribute to the SFR uncertainties.

I.1.1 Core-collapse supernovae

The death of stars more massive than 8 $M_\odot$ is marked by their explosion as CCSNe resulting in a release of kinetic energies of typically $\sim 10^{51}$ erg s^{-1} ($\sim 2.6 \times 10^{17}$ L$_\odot$) per supernova (see e.g., the review by Smartt, 2009).

The initial mass (M_{init}) and metallicity of the progenitor star (and the implied mass loss) give rise to different SN types, which are primarily characterised by their optical spectra (see figure 1 in Turatto, 2003). The main division of SNe was made according to the absence or presence of hydrogen features in their spectra (Minkowski, 1941), namely type I and type II SNe, respectively. Type I was further subdivided into type Ia (showing Si absorption and no He features) and type Ib/c (showing He features and no Si absorption); on the other hand type II were subdivided according to the shape of their light curves: IIL (linear decay), IIP (plateau phase) and IIn (strong narrow profile). Type Ia SNe occur by thermonuclear explosion (associated with white dwarfs), whereas the rest are different kinds of the so-called CCSNe.

The stellar models by Heger *et al.* (2003), have set limits on the M_{init} and metallicity of the different SN progenitor stars. These models, based on single-star evolution, indicate that neutron stars are formed from progenitor stars covering a wide range of metallicities and M_{init}. At low metallicities and $M_{\mathrm{init}} \gtrsim 40$ M$_\odot$, stars end their lives as black holes. At higher metallicities but lower M_{init}, black holes can also be formed by fall-back. Recently, Smith *et al.* (2011) have estimated M_{init} ranges for the different SN types by examining different stellar evolutionary scenarios (involving stellar winds and evolution in binaries) and adjusting them to the observed fractions of different CCSN types. They found that progenitors of type IIP SNe have $8.5 \lesssim M_{\mathrm{init}}[\mathrm{M}_\odot] \lesssim 18$; type Ib plus transitional SNe called IIb come from stars having $8.5 \lesssim M_{\mathrm{init}}[\mathrm{M}_\odot] \lesssim 25$ and type Ic progenitors being more massive and leading to stronger winds; progenitors of type IIn would have $23 \lesssim M_{\mathrm{init}}[\mathrm{M}_\odot] \lesssim 150$ and those of type IIL correspond to $18 \lesssim M_{\mathrm{init}}[\mathrm{M}_\odot] \lesssim 23$.

Statistics from volume-limited samples of nearby SNe (Li *et al.*, 2011; Smith *et al.*, 2011) indicate that type IIP are the most common CCSNe ($\approx 48.2\%$), followed by type Ib/c plus type IIb ($\approx 36.6\%$), type IIn ($\approx 8.8\%$) and finally by the less numerous type IIL ($\approx 6.4\%$). However, dust extinction is an important bias factor in these estimates, causing that basically all the SNe occurring in the innermost nuclear regions of galaxies are missed if we restrict SN surveys to optical observations, or even to less extinguished, NIR observations (see §I.2.1 and Chapter II).

I.1.1.1 Relation between CCSN rate and massive SFR

As it was mentioned in §I.1.1, the progenitor stars giving origin to the different types of CCSNe have different M_{init}, hence, ν_{SN} will give information on the rate at which their progenitor stars are born (e.g., Condon, 1992; Madau *et al.*, 1998). If we are interested in how many CCSNe explode, independently of their type, we can use the approaches by e.g., Kewley *et al.* (2000), Mattila and Meikle (2001), Pérez-Torres *et al.* (2009a), etc., to obtain CCSN rates by integrating the SFR over the IMF.

For a SFR, $\Psi(t)\,[\text{M}_\odot\,\text{yr}^{-1}]$, of stars with $M_{\text{init}} \gtrsim 8\ \text{M}_\odot\ (\equiv m_{\text{CCSN}})$ and assuming that the IMF does not vary with time, we have,

$$\nu_{\text{SN}} = \frac{\int \int_{m_{\text{CCSN}}}^{m_{\text{max}}} \Phi(m)\Psi(t)\mathrm{d}m\mathrm{d}t}{\int_{m_{\text{l}}}^{m_{\text{u}}} m\Phi(m)\mathrm{d}m},$$

where m_{u} and m_{l} are the upper and lower limits, respectively, for the range of masses of stars formed, and m_{max} is the maximum progenitor mass of CCSNe.

For galaxies which are preferentially forming intermediate and high mass stars, it is fair to assume a Salpeter IMF (Salpeter, 1955):

$$\Phi(m) = \Phi_0 \left(\frac{m}{m_0}\right)^{-x},$$

with slope $x = 2.35$ and mass cut-offs $m_{\text{u}} \approx 150\ \text{M}_\odot$ (Weidner and Kroupa, 2004) and $m_{\text{l}} \approx 1\ \text{M}_\odot$. Furthermore, if we assume that the SFR remains constant with time, and that the maximum mass for a CCSNe progenitor is 100 $\text{M}_\odot$ (e.g., the mass of SN 2006gy progenitor, Smith *et al.*, 2007) the relation for ν_{SN} becomes,

$$\nu_{\text{SN}} = \Psi \left(\frac{2-x}{1-x}\right) \left(\frac{m_{\text{max}}^{1-x} - m_{\text{CCSN}}^{1-x}}{m_{\text{u}}^{2-x} - m_{\text{l}}^{2-x}}\right)$$

$$\Rightarrow \left(\frac{\nu_{\text{SN}}}{\text{yr}^{-1}}\right) \approx 0.018 \left(\frac{\Psi}{\text{M}_\odot\,\text{yr}^{-1}}\right) \tag{I.3}$$

Whilst assuming a realistic IMF, the detection of new CCSNe can yield information on the SFR for massive stars in the host galaxy, provided that the number of detections over time allows a reasonable statistical estimate (since the approximation of a constant SFR with time is not necessarily valid). Note also that the values for the different mass cut-offs are metallicity-dependent. For instance, Pindao *et al.* (2002) found a maximum value for m_{u} of about 90 $\text{M}_\odot$ in regions with solar metallicities. Consequently, the IMF might become more top-heavy (i.e., favouring the production of massive stars) in low metallicity cases.

Equation I.3 is not adequate when the contribution of low mass stars is significant against the contribution of massive stars. For instance, in our own Galaxy massive stars are not very copious: the nearest one is at about $500\,\mathrm{pc}$ distance from the Sun, and at most one out of 100 stars is massive (see e.g., Osorio, 2000). Therefore, the expectations for SNe in our Galaxy, in particular CCSN explosions, are low ($1\,\mathrm{SN}$ every $50\,\mathrm{yr}$ Diehl *et al.*, 2006).

I.1.1.2 CCSN emission at radio wavelengths

When a massive star is born, it begins to produce a radiation field in the extreme UV thus giving rise to an ionization front that quickly propagates through the gas. This leads to the destruction of all molecular species whose bound energies are less than the characteristic energy of the radiation field. Due to the amount of available ionizing radiation, a region of ionized gas called HII region is created around the star. A star is able to ionize the region if it produces photons with energy greater than $13.6\,\mathrm{eV}$ (which corresponds to the ionization potential of the hydrogen), i.e., photons with wavelengths $< 912\,\text{Å}$. This condition is fulfilled by massive stars of type OB.

The winds generated as massive stars evolve will result in different mass loss rates depending on M_{init} and the ambient conditions. The pre-SN wind (ionized media) constitutes the circumstellar medium (CSM), and has typical values of $\sim 10^4\,\mathrm{K}$ for temperature, $\sim 10\,\mathrm{km\,s^{-1}}$ for its expansion velocity and $\sim 10^7\,\mathrm{H\text{-}atoms\,cm^{-3}}$ for density, which decreases with the distance r from the photosphere of the star ($\rho_{\mathrm{CSM}} \propto r^{-s}$, with a typical value of $s \sim 2$).

The origin of the radio emission (extinction free) from CCSNe can be explained by the Standard Interaction Model (SIM) proposed by Chevalier (1982). The SN ejecta interacts first with the CSM, giving rise to CCSN radio emission, and later, as it continues propagating outwards, interacts with the ISM, giving rise to the supernova remnant (SNR) phase. The cartoon in Figure I.1 (from Weiler *et al.*, 2002), is the representation of the different media that the SN ejecta traverses, with the subsequent generation of shocks.

The SN ejecta is characterized by much larger temperatures ($\sim 10^9\,\mathrm{K}$) than the pre-SN wind, and moves ~ 1000 faster ($v \approx 10,000\,\mathrm{km\,s^{-1}}$), expanding self-similarly with time according to the SIM ($R \propto t^m$, with $m \leq 1$). The deceleration parameter m, depends on both the density profiles of the CSM (ρ_{CSM}) and the SN ejecta itself ($\rho_{\mathrm{SN}} \propto r^{-n}$, $7 \leq n \leq 12$).The CSM will act as a thermal absorber of the SN radio emission, with an optical depth which varies with frequency ($\tau \sim \nu^{-2.1}$) and decreases rapidly with distance. I refer the reader to Chevalier (1982) and Weiler *et al.* (2002) for details.

The difference in velocities and temperatures between the SN ejecta and the CSM
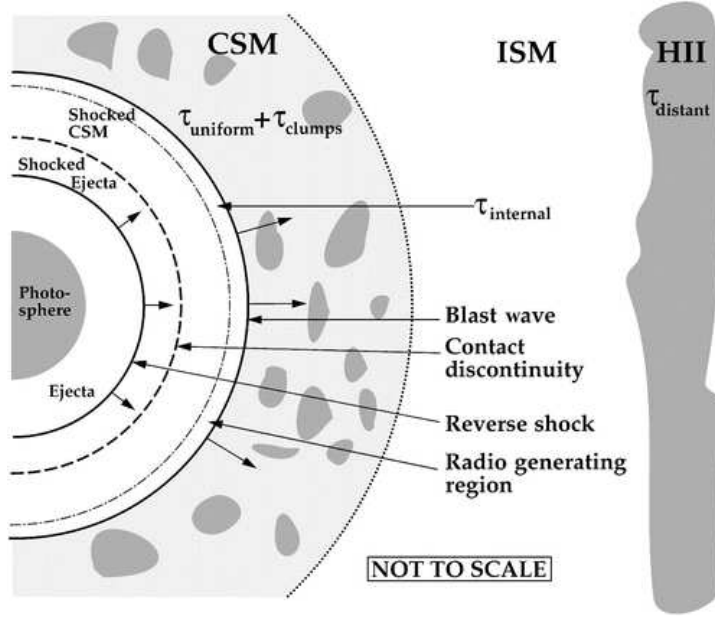
FIGURE I.1: Scheme of propagation of the SN ejecta through the different surrounding media (taken from Weiler *et al.*, 2002). The SN radio emission, generated near the blast-wave front, is subject to attenuation from different components of the surrounding media.

generates a discontinuity region. As the back layers of the SN expanding shell reach the front ones, a reverse shock is generated (see Figure I.1). The radio emission is produced in the region delimited by the reverse and the front shocks. At the shock front, the magnetic field lines are compressed, thus enhancing the magnetic energy and providing a re-acceleration mechanism for relativistic electrons (with a population distribution following a power law with energy), and giving origin to the synchrotron emission that we observe at radio wavelengths.

SN radio light curves have been parametrized by Weiler *et al.* (2002). Different factors of attenuation (see Figure I.1) are taken into account to deal with the physical properties of both the CSM and the ISM. A decrease in absorption with time while the shocked region expands is observed, implying that SN radio emission becomes transparent first at high frequencies, and later at shorter frequencies. The optically thick ($\tau > 1$) part of the light curve is dominated by synchrotron emission which is partially self-absorbed and/or absorbed by thermal free-free emission from the ionized CSM. After reaching its peak of radio brightness, the supernova becomes optically thin ($\tau < 1$) and the synchrotron emission is characterised by a rather steep spectrum at centimetre wavelengths ($\alpha \lesssim -0.7$; $S_\nu \propto \nu^\alpha$).

Whilst a spectral identification is only possible for those nearest, less extinguished SNe, some of their properties have been drawn from their radio light curves, including information on the progenitor's nature, the magnetic field involved in the shocks, the

spectral evolution, etc. For instance, type Ib SNe are characterised by a strong, steep spectrum (ν^{-1}) and a rapid decay ($t^{-1.6}$), whereas type IIL SNe display a strong, flatter spectrum ($\nu^{-0.6}$) and a slow decay ($t^{-0.7}$) (e.g., Weiler and Sramek, 1988). Most SNe display luminosities ranging from $\lesssim 10^{26}$ (e.g., type IIP), up to 10^{28} erg s^{-1} Hz^{-1} (e.g., type IIn). No radio emission has been detected arising from type Ia SNe (Panagia et $al.$, 2006), and the limiting factor might be their intrinsic low radio-luminosity ($\lesssim 10^{25}$ erg s^{-1} Hz^{-1}), which is not detectable with the majority of current instruments. In the last couple of years, many unsuccessful attempts have been made to detect type Ia SNe with the Expanded Very Large Array (EVLA), thus pointing to another limiting factor: a very short (e.g., a few days) RSN lifetime.

At any rate, it seems that the more luminous the RSN is, the longer it takes to reach its peak. This is the conclusion drawn from observations of peak radio luminosity vs. time to reach the peak for different types of RSN (see e.g., figures 2 and 5 in Chevalier et $al.$, 2006; Alberdi et $al.$, 2006, respectively, and Figure III.4 in this thesis). In Chapter III, I have made an extensive use of this tool.

I.1.2 SED in star forming galaxies and the FIR-radio correlation

From the previous sections, we can bundle up a number of characteristics in the emission of a galaxy, which originate from the presence of massive stars:

- Synchrotron emission from relativistic electrons originated/re-accelerated in shocks, i.e., via SN and SNR events (dominating at cm wavelengths).

- Free-free thermal emission from HII regions (dominating at cm–mm wavelengths).

- Thermal emission from dust, which absorbs UV and optical light, and re-radiates it at IR wavelengths, especially in the FIR (dominating at mm–submm wavelengths).

These elements dominate the spectral energy distribution (SED) of star forming galaxies, as shown in Figure I.2.

Radio (non-thermal) and FIR (thermal) emission are manifestations of massive SF processes. The so-called FIR-radio correlation emerges from this fact (see Condon, 1992, and references therein). The correlation is linear (described by the parameter q) and its relevance relies on its validity for a great variety of FIR selected galaxies (Figure I.3). The performance of this correlation as a SFR tracer depends (alike other tracers) on the optical obscuration towards star forming regions.
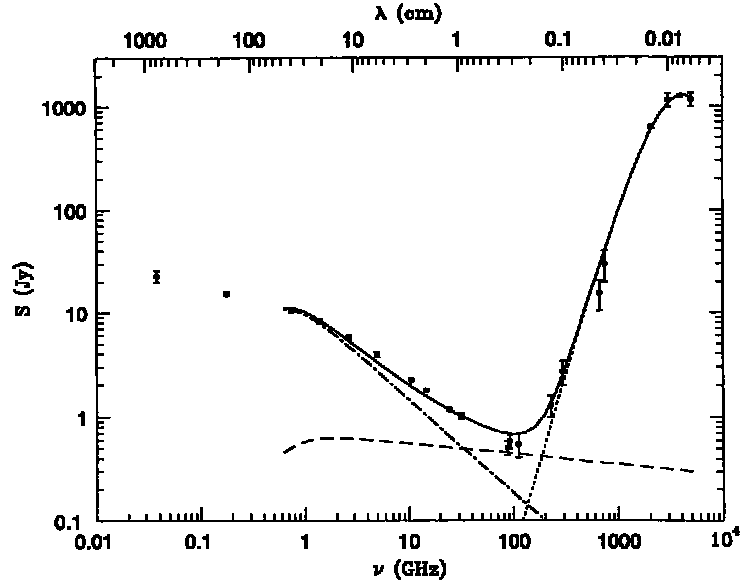
FIGURE I.2: Observed radio/far-IR spectrum of the galaxy M82 (from Condon, 1992). The synchrotron emission (dash-dotted line) dominates at low frequencies, and appears slightly diminished at frequencies around 1 GHz due to free-free absorption. The free-free emission from HII regions (dashed line) dominates between 30 and 200 GHz, being then overtaken by thermal emission from dust (dotted line).
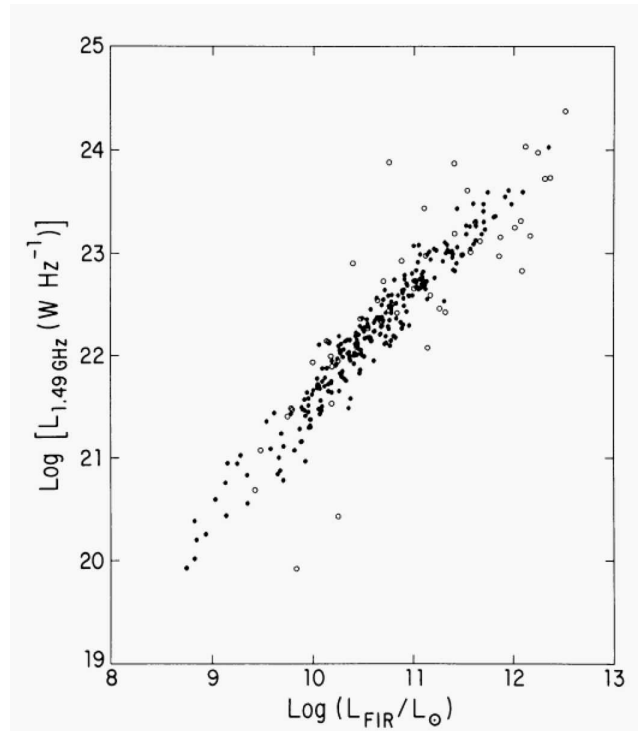
FIGURE I.3: The FIR-radio correlation for strong sources at 60 μm which do not suffer strong free-free absorption at low frequencies (~ 1.4 GHz) and not known AGN contribution (taken from Condon, 1992). Deviations from this correlation, might indicate a larger or lower contribution from an AGN.

The q parameter has been defined (Helou *et al.*, 1985) as,

$$q \equiv \log \left(\frac{\mathrm{FIR}}{3.75 \times 10^{12}\,\mathrm{W\,m^{-2}}} \right) - \log \left(\frac{S_{1.4\,\mathrm{GHz}}}{\mathrm{W\,m^{-2}\,Hz^{-1}}} \right),$$

where $S_{1.4\,\mathrm{GHz}}$ is the observed flux density at $1.4\,\mathrm{GHz}$, and

$$\mathrm{FIR} \equiv 1.26 \times 10^{-14} \left(2.58 S_{60\,\mu m} + S_{100\,\mu m} \right)$$

with $S_{60\,\mu m}$ and $S_{100\,\mu m}$, the Infrared Astronomical Satellite (*IRAS*) flux densities at 60 and 100 μm, respectively. Yun *et al.* (2001) have constrained the q value to 2.34 ± 0.01 for an *IRAS* sample with $S_{60\,\mu m} > 2\,\mathrm{Jy}$, and $S_{1.4\,\mathrm{GHz}}$ fluxes obtained from the NRAO VLA Sky Survey (NVSS), providing an angular resolution of 45 arcsec (close to the resolution attained by *IRAS*). It is worth to note that different values of q are to be obtained, when using $S_{1.4\,\mathrm{GHz}}$ measurements from radio observations with higher resolution, which resolve the diffuse emission and thus result in lower flux densities.

I.1.3 Inducing bursts of star formation

The SFR is different from galaxy to galaxy. For instance, the SFR in the Milky Way is 0.68–1.45 $\mathrm{M_\odot\,yr^{-1}}$ (Robitaille and Whitney, 2010). If the entire ISM in a galaxy (10^{10}–$10^{11}\,\mathrm{M_\odot}$) would be converted into stars at this low SFR, the SF could be maintained for a few 10^9 yr in a normal disk galaxy. Galaxies with prolific star formation have SFRs at least two orders of magnitude larger than in our Galaxy. Although it is usually assumed that the SFR remains constant over the SF history of a galaxy (as done in equation I.3), consuming the gas at high SFRs (e.g., 10–100 $\mathrm{M_\odot\,yr^{-1}}$) implies that the SFR can only be maintained in a period ($\sim 10^7$–10^8 yr; Kennicutt, 1998) much shorter compared to a Hubble time; thus, an instantaneous burst, where all the mass is converted into stars, i.e., a starburst, is suggested.

Sudden, violent SF, often accompanied by AGN activity, can be triggered by the interaction (mergers, or close encounters) of gas rich galaxies (see e.g. Di Matteo *et al.*, 2007). Numerical simulations point to the bars in galaxies as the probable via to feed the starburst (e.g., Shlosman *et al.*, 1990). Large amounts of gas comparable to the mass of the entire ISM in a galaxy are brought to a $\approx$1 kpc size region (the nuclear and circumnuclear regions), with the subsequent compression of gas and its rapid consumption.

I.2   Luminous and ultra-luminous infrared galaxies

The Infrared Astronomical Satellite (*IRAS*), launched in 1983 (Neugebauer *et al.*, 1984), brought the discovery of a new class of galaxies displaying large IR luminosities (Soifer *et al.*, 1984). A galaxy whose IR luminosity ($L_{\mathrm{IR}} = L[8\text{–}1000]\ \mu$m) is $> 10^{11}$ L$_\odot$, is called luminous infrared galaxy (LIRG); with a larger luminosity ($> 10^{12}$ L$_\odot$), the galaxy receives the name of ultra-luminous infrared galaxy (ULIRG). These are scaled-up versions of the so-called starbursts galaxies.

(U)LIRGs exhibit two main facets. These galaxies radiate most of their energy in the FIR (40–500 μm) and display optical quasi-stellar object (QSO)-like luminosities. Nevertheless, (U)LIRGs also have FIR, mm, and radio characteristics which resemble those of star-forming galaxies (see e.g., Soifer *et al.*, 1987; Sanders and Mirabel, 1996).

Most (U)LIRGs seem to be the products of galaxy-galaxy interactions, mergers or bar instabilities, i.e., when no recent merger activity is found. Low redshift LIRGs are rare, but at $z \sim 1$ (Le Floc'h *et al.*, 2005) they are found to dominate the IR background, as well as the SFR density. The same is true for ULIRGs, but at $z \sim 2$ (Caputi *et al.*, 2007).

It is thought that ULIRGs represent a key stage in the formation of QSOs and powerful radio galaxies (e.g., Sanders *et al.*, 1988). A study based on Hubble Space Telescope (*HST*) observations and *N*-body simulations point to diverse evolutionary paths, not necessarily including a QSO phase (Farrah *et al.*, 2001). There is however a general agreement on gas-rich galaxy merging as the origin of (U)LIRGs (Sanders and Mirabel, 1996), and on the ubiquity of enhanced SF, which can be found in combination with different flavours of AGN activity (e.g., Farrah *et al.*, 2003). Which of these two contributions dominates and is thus the main responsible for the overall dust heating, is still an open question.

Kewley *et al.* (2006) presented a classification scheme of galaxies based on optical emission line ratios of a robust sample of galaxies from the Sloan Digital Sky Survey (SDSS). This scheme allows to discriminate between starbursts, Seyferts, low-ionisation narrow emission-line regions, and composite starburst-AGN types. More recently, Yuan *et al.* (2010) used Kewley *et al.* scheme to classify a sample of IR selected galaxies, as a function of IR luminosity and merger stage. Their results support an evolutionary scenario in which ULIRGs are dominated by starburst activity at an early merger stage; at intermediate stages, ULIRGs would be powered by a composite of starburst-AGN activity; and finally, at later stages, an AGN would dominate the emission.

Although uncommon at lower redshifts, the presence of (U)LIRGs in the local Universe offers the opportunity of investigating their parsec scale structure, while profiting from the high angular resolution provided by current instrumentation. Studying (U)LIRGs in

the local Universe is of great importance since it can aid to understand their high-redshift analogues which dominate the sub-mm sky (see e.g., Lilly *et al.*, 1999).

I.2.1 The hidden population of SNe in (U)LIRGs

The detection of SNe occurring in the nuclear regions of LIRGs is in most cases not feasible at optical wavelengths due to severe dust extinction. Observations in the NIR K-band where the extinction is strongly reduced ($A_K \sim 0.1 \times A_V$) can be used for their successful detection (e.g., Mattila and Meikle, 2001; Maiolino *et al.*, 2002). However, the tight concentration of the SF within the innermost nuclear regions of LIRGs (e.g., Soifer *et al.*, 2001) means that the detection of such SNe even at NIR wavelengths in natural seeing conditions is often not feasible. Recent SN search programmes, benefiting from the high spatial resolution offered by adaptive optics (AO) observations at NIR wavelengths, have already discovered several obscured SNe close to LIRG nuclei. For example, SN 2004ip with a likely high extinction $A_V > 5$ mag (Mattila *et al.*, 2007) was detected at a projected distance of 1.4 arcsec, or 500 pc, from the K-band nucleus of the nearby LIRG, IRAS 18293−3413. Its core-collapse nature was confirmed by a Very Large Array (VLA) detection at 8.4 GHz (Pérez-Torres *et al.*, 2007). Two SNe, SN 2004iq and SN 2008cs (Kankare *et al.*, 2008) were detected in the circumnuclear regions of the nearby LIRG IRAS 17138−1017. SN 2008cs was shown to suffer from a record high extinction of $A_V \sim 18$. Its core-collapse nature was again confirmed by a radio detection at 22.4 GHz using the VLA (Pérez-Torres *et al.*, 2008). SN 2010cu detected at 0.4 arcsec (180 pc) from the K-band nucleus of the nearby LIRG IC 883 (Ryder *et al.*, 2010a), has also a likely high extinction. More recently, another probable SN (PSN J13203538+3408222) was detected at 0.8 arcsec (360 pc) from the centre of the K-band nucleus of the same galaxy (Kankare *et al.*, 2011b).

Radio (i.e., extinction free) observations represent the most direct way to distinguish between a starburst and an AGN, via the detection of SNe, SNRs and/or compact sources at mas-resolution with a high brightness temperature (T_B), possibly accompanied by a core-jet morphology (usually associated with a high X-ray luminosity and a flat spectral index). Observations made with the very long baseline interferometry (VLBI) technique have resulted particularly useful, for instance, to discover a population of bright radio SNe (RSNe) and SNRs in the nuclear regions of the (U)LIRGs Arp 220 (Smith *et al.*, 1998b) and Mrk 273 (Carilli and Taylor, 2000). This has also been the case for LIRGs, such as Arp 299 where a prolific starburst and a low luminosity AGN (LLAGN) were discovered (Neff *et al.*, 2004; Pérez-Torres *et al.*, 2010, respectively) through VLBI observations, or the recent detection of AGN activity in a number of LIRGs from the Compact Objects in Low-power AGN sample (COLA) (Parra *et al.*, 2010). High sensitivity is also important: radio

observations towards Arp 299 (Pérez-Torres *et al.*, 2009b) and Arp 220 (Parra *et al.*, 2007; Batejat *et al.*, 2011) have discovered even a larger number of compact sources populating the nuclei of these galaxies, thus agreeing better with the high expectations of CCSN explosions in (U)LIRGs.

I.3 Guide through the chapters of this thesis

In the previous sections I have given a conceptual framework for the objects of study in this thesis. Chapter II contains an overview of the observational techniques used in this thesis to investigate (U)LIRGs. In Chapter III, I present the observations (radio, and one epoch of infrared data) towards the LIRG Arp 299 which allowed the direct and indirect detection of supernovae in the nuclear regions of this LIRG. In the Chapter IV, I present our radio observations that aimed at detecting water masers towards two LIRGs (Arp 299 and NGC 7469) with the goal of characterising the warm gas around the AGN in each galaxy. In Chapter V, I introduce our study towards four of the most luminous and farthest ULIRGs in the local Universe, and present the results from radio observations covering different scales (nuclear, circumnuclear and galactic) in one of the galaxies of our sample: the ULIRG IRAS 23365+3604. Chapter VI contains our results from radio observations of the LIRG IC 883, in which we discovered a LLAGN in coexistence with a nuclear starburst (alike the case of Arp 299-A presented in Chapter III). Chapter VII contains the general conclusions and prospectives for the work presented in this thesis. In VII, I summarize and discuss the results obtained in the different publications in which this thesis is based, and describe my contributions to each publication. Appendix A provides the base to understand the radiative transport of radio emission, and introduces some nomenclature that is continuously used throughout this thesis. Appendix B is meant as a reference for the approximation of brightness temperature adopted in this thesis, given that different ones abound in the literature.

CHAPTER II

OBSERVATIONAL TECHNIQUES

The study of (U)LIRGs implies to deal with dusty environments, usually placed at large distances (a few tens to a few hundreds of Mpc) in the local Universe. High angular resolution observations are thus necessary: i) to resolve out the diffuse emission of the galaxy itself, and ii) to disentangle the different components in the nuclear and circumnuclear regions of these galaxies. On top of that, the observations are required to provide high sensitivity, since the individual components (e.g., SNe) are expected to have flux densities of the order of a few mJy (see Fig. II.1).
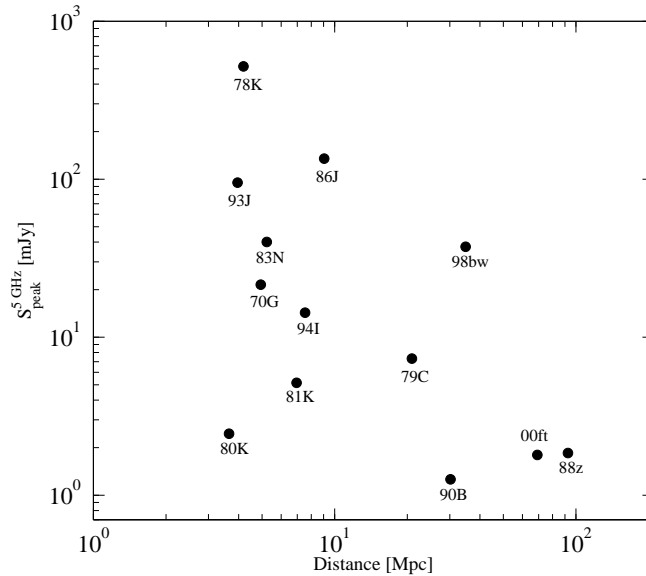
FIGURE II.1: 5 GHz peak flux density for a representative number of SNe in starburst galaxies at different distances (values from Weiler *et al.*, 2002). The need for high sensitivity and angular resolution becomes more evident and important when studying objects at larger distances. Note for instance that a higher sensitivity would be needed to detect the emission of SN 1990B (at a distance of ~ 30 Mpc) than that of SN 1983N (at ~ 5 Mpc), although these two have intrinsically similar luminosities. Likewise, a higher angular resolution is needed to resolve two objects (e.g., a supernova exploding close to the nucleus of a galaxy), when the distance to them increases.

High angular resolution and high sensitivity are not the only factors needed to observe deep in the nuclei of (U)LIRGs. The large amount of dust present in those regions is a key factor, which will restrict the observations to be done at certain wavelengths. The dust scatters and absorbs the light, i.e., extinguishes it. This effect is more notorious at UV and optical wavelengths. Typically, the extinction at NIR wavelengths is about one tenth of the extinction in the optical. The study of the innermost nuclear and circumnuclear regions of (U)LIRGs at optical or shorter wavelengths is thus heavily affected by dust extinction. Within the NIR, the K-band ($\sim 2.2\,\mu$m) is the least affected by dust and hence it represents a good option to perform observations of the most obscured regions.

Radio observations are extinction-free, and hence represent an excellent choice to study (U)LIRGs, as well as K-band NIR observations, which are not heavily affected by dust extinction. In this thesis, I make use of these two complementary tools.

II.1   Radio observations

In radio astronomy, we study phenomena which radiate energy at wavelengths above $\sim 1\,$mm in the electromagnetic spectrum.

Observations at radio wavelengths profit from the transparency of the Earth's atmosphere (see Fig. II.2) and from the non-interaction of radio wavelengths with dust particles. The latter advantage comes from the fact that dust grain sizes are smaller than a few μm (Weingartner and Draine, 2001), and hence only radiation at wavelengths comparable to, or smaller than, the dust grains will be subject to absorption and scattering (i.e., to extinction). Since the dust grains are much smaller than the size of radio wavelengths, these are not affected by dust extinction.
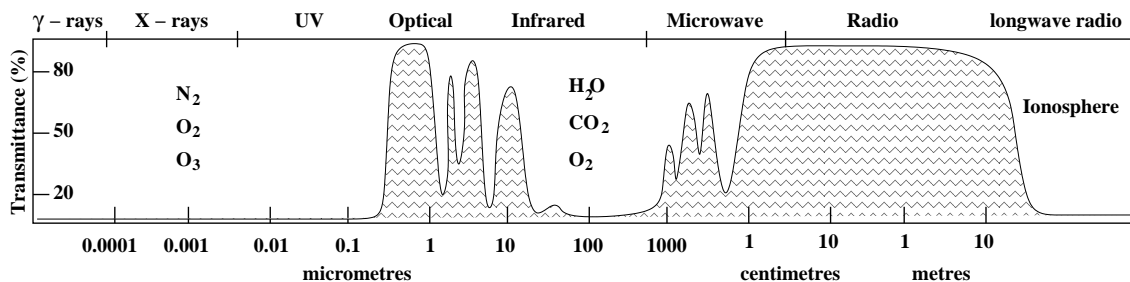
FIGURE II.2:   Atmospheric transmittance of the Earth at different wavelengths (adapted from Burke and Graham-Smith, 2010). Ground-based observations can be performed when the transmittance is high (e.g., 80%). Apart from the optical, infrared and radio windows, radiation at other wavelengths is absorbed by different molecules in the atmosphere, or scattered by the ionosphere.

The radio window is divided into different bands, the most common ones are listed

in Table II.1. Note that the central frequencies, as well as the widths of each band, may vary from one radio telescope to another, depending on the characteristics of their receivers.

TABLE II.1: Division of the radio window. Electronic filters, or frequency bands, can be tuned to amplify a specific frequency range, being centred at a specific frequency. The most commonly used central frequencies for each band are listed here (excluding mm-frequencies).

Band name	Frequency (GHz)	Wavelength (cm)
L	1.7	18
C	5.0	6
X	8.3	3.6
U	15	2
K	23	1.3
Q	43	0.7

Although the atmosphere is quite transparent to radio wavelengths (see Fig. II.2), some problems arise at the edges of the radio window. For example, at high radio frequencies ($\gtrsim 20\,\text{GHz}$) the water content of the troposphere has to be taken into account, while at low radio frequencies ($\lesssim 5\,\text{GHz}$) it is the electron content of the ionosphere which mainly affects our measurements.
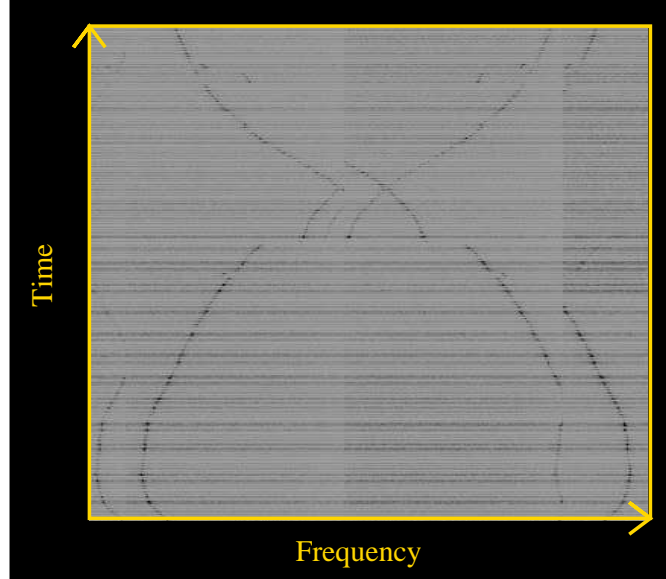
FIGURE II.3: Example of severe radio frequency interference, on data obtained with a radio telescope used for observations presented in this thesis. The plot shows the result of two external signals which travel in time from the edges of the band towards the centre, interfere generating further ripples, and then continue their way towards opposite edges.

One of the major threats for radio astronomical measurements is radio frequency

interference (RFI) generated by radio transmitters, such as military radars, mobile phones, microwave ovens, televisions, security systems, etc. RFIs can effectively mask and/or corrupt the radio emission from our objects of study (see an example of this in Fig. II.3). Restricting technologies to the use of frequencies outside the radio window is a way of mitigating RFIs, however there is still the danger of some 'spillover' into the receiver's frequency bandwidth at radio telescopes. Thus, the most sensitive thing to do is to build radio telescopes in radio quiet zones to avoid interferences between the radio emission that comes from the sky and that resulting from the use of different technologies.

II.1.1   Radiation mechanisms at radio wavelengths

The radiation mechanisms in radio are classified as thermal and non-thermal. If we consider the optically thin flux density (S_ν) emitted by a source to be related with the frequency (ν) as $S_\nu \propto \nu^\alpha$, then, the thermal radiation, which increases with ν, is characterised by $\alpha > 0$, whilst the non-thermal radiation decreases with ν, i.e., $\alpha < 0$.

The thermal radiation (resulting from the thermal motion of particles) can be explained by comparing the emission of the source with that of a black body. In that case, we define a temperature (brightness temperature, T_B), such that the intensity of the emission at each frequency, is the intensity given by the Planck function at T_B (see Appendix B). Non-thermal radiation can have larger intensities, regardless of the physical temperature of the emitting source, since different processes govern its nature.

The radiation, either thermal or non-thermal, can be found in two different modes: as broadband emission (continuum), or frequency dependent, i.e., occurring only in a narrow range of frequencies (spectral line). For instance, free-free (bremsstrahlung) radiation is thermal continuum radiation from ionised gas, as occurs in HII regions. Thermal spectral line radiation can be observed through atomic and molecular transitions occurring in cold dense molecular clouds, for example, the HI 21 cm line. Regarding non-thermal continuum radiation, synchrotron is the most important mechanism in radio, and it is due to relativistic electrons spiralling along magnetic field lines. Finally, non-thermal spectral line radiation can be observed in the form of Microwave Amplification by Stimulated Emission of Radiation (MASER), meaning that the particles (atoms, molecules, etc.) composing a system, occupy preferentially a state with higher energy than that corresponding to the ground-state level. The interaction of such inverted population with a photon matching their excitation energy, produces further photons with the same energy/direction as the interacting photon, thus amplifying its emission by large factors.

The radiation from the different processes outlined above interacts with matter in their way to the observer. The radiative transfer equation accounts for the changes in intensity

(I_ν) that the radiation undergoes while it propagates through matter, and can be expressed by the equation A.3 in Appendix A,

$$I_\nu(\tau_\nu) = I_\nu(0)e^{-\tau_\nu} + \mathbb{S}_\nu \left(1 - e^{-\tau_\nu}\right).$$

The observed intensity (I_ν) has two components: one corresponding to the emitted radiation intensity $(I_\nu(0))$ that is attenuated by the traversed matter, and a second term corresponding to the contribution of the traversed matter itself (incorporated in $\mathbb{S}_\nu$, the source funtion). The basics of radiative transfer are found in Appendix A.

There is a great variety of instruments used nowadays to detect radio emission. In the following sections, I briefly describe those which have been used for the observations presented in this thesis.

II.1.2 Single-dish observations

The energy associated with radio photons is much lower than that of optical photons; therefore, the direct detection of radio photons by means of their conversion to thermal energy, or by the photoelectric effect, is not feasible. Instead, we detect radio photons as waves, i.e., we obtain information on their phase and amplitude.

A single-dish radio telescope (i.e., an antenna), can be thought of as an aperture that intercepts a plane wave (since radio sources are far away), coming from a specific direction. The response of an antenna to the radiation coming from different directions is described by the antenna pattern (see Fig. II.4), which is maximum in the direction of the symmetry axis.
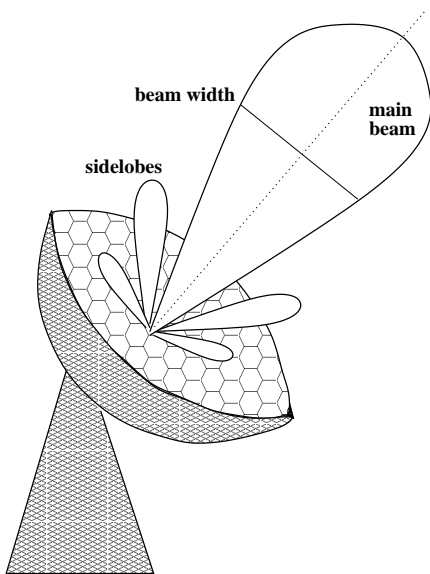
FIGURE II.4: Illustration of the antenna pattern. The dotted line represents the pointing direction in which the antenna is most sensitive for incoming radiation. Plane waves arriving to the antenna in directions different to the symmetry axis will also contribute to the measured signal, but to a lesser extent (depending on the strength of the sidelobes). The beam width of the main lobe (or beam) is a measure of the resolution power of the antenna.

II.1 Radio observations

The width of the main beam is characterised by its full width at half maximum (FWHM). This gives the angular resolution that the antenna can provide, and is proportional to λ/D, where D is the diameter of the antenna, and λ the observed wavelength. The beam width accounts for the smallest structure that can be resolved with a radio telescope, and ranges from a few tens of arcsec, up to a few arcmin for radio wavelengths. For instance, observing at $22\,\mathrm{GHz}$ with a $25\,\mathrm{m}$ antenna will result in an angular resolution of $\approx 2\,\mathrm{arcmin}$, whilst an angular resolution of $\approx 30\,\mathrm{arcsec}$ can be obtained observing with a $100\,\mathrm{m}$ antenna.

The detection of a radio signal consists in reflecting the incoming radiation in the central focus of the antenna to generate an electric current (normally very weak), which has to be amplified in the receiver of the radio telescope before it can be detected. This current needs to be calibrated with respect to the incoming radiation.

The intensity of the radiation of an emitting source, I_ν ($\mathrm{erg\,s^{-1}\,cm^{-2}\,sr^{-1}\,Hz^{-1}}$), is the energy emitted per unit time, per unit intercepting area, per unit solid angle, per unit frequency interval. Comparing the emitting source to a black body (see Appendix A), we can express I_ν in terms of a temperature, which we call brightness temperature (T_B). If the intercepting area is that of an antenna, we must consider the characteristics of the antenna itself, as well as the characteristics of the ambient medium where the antenna is placed, in order to determine T_B.

I have mentioned before that an antenna is characterised by its antenna pattern. The better the main beam represents the antenna pattern, the smaller the contribution of the sidelobes, and the better the antenna quality will be. This is measured by the main beam efficiency,

$$\eta_\mathrm{B} = \frac{\Omega_\mathrm{MB}}{\Omega_\mathrm{A}},$$

where Ω_MB is the solid angle subtended by the main beam, and Ω_A is the solid angle subtended by the whole antenna pattern. Using the same analogy between I_ν and T_B, we can describe the power received by the antenna in terms of the so called antenna temperature, which is related to the power received by the main beam (also expressed in terms of a temperature) as,

$$T_\mathrm{A} = \eta_\mathrm{B} T_\mathrm{MB}$$

In turn, T_MB is related to T_B emitted by a source of size Ω_s, through

$$T_\mathrm{B} = T_\mathrm{MB}\,\frac{\Omega_\mathrm{obs}}{\Omega_\mathrm{s}},$$

where Ω_obs is the observed size of the source by the antenna (see Appendix B).

T_A contributes to the output signal of the radio telescope, and it is ultimately the value

we need in order to calculate T_B. However, T_A suffers contamination from different sources of noise, which we collectively call system temperature (T_{sys}). The sky, the atmosphere, the ground noise pick-up, the receiver, etc., contribute to T_{sys}. The calibration process, consists in determining these noise factors to obtain the signal that originally came from the source. T_{sys} will set a limit on the minimum temperature (or intensity) which we can detect with a given antenna.

Following the Nyquist theorem, when observing a source in a range of frequencies $\Delta\nu$, the time-resolution Δt_{int} (duration of a sample) needed to have statistically independent samples, and be able to recover the signal, must fulfil

$$\Delta\nu\Delta t_{int} = 1,$$

Observing a source for a total time, t_{int}, will result in N samples ($t_{int} = N\Delta t_{int}$), each one with an error given by $\mathbb{K}T_{sys}$, where $\mathbb{K}$ is a constant which depends on the sensitivity of the receiver and the frequency at which it operates. Following Gaussian statistics, the associated error to N samples would be

$$\Delta T \simeq \frac{\mathbb{K}T_{sys}}{\sqrt{N}} \simeq \frac{\mathbb{K}T_{sys}}{\sqrt{t_{int}\Delta\nu}} \tag{II.1}$$

which is called the Radiometer equation (see e.g., Burke and Graham-Smith, 2010).

As I mentioned above, the smallest detail we can resolve with single-dish observations, is of the order of a few tens of arcsec at most. This resolution is suitable to study large structures, or for observations meant as detection experiments. The latter is the case for the data presented in §IV.2 of this thesis, which has been obtained with the Effelsberg radio telescope.

II.1.2.1 The Effelsberg 100 m radio telescope

The Effelsberg radio telescope is one of the most sensitive and largest fully steerable antennas in the world (Fig. II.5). It has a Gregorian design consisting of a 100 m paraboloid (the primary mirror) and a 6.5 m concave ellipsoid (the secondary mirror). There are 22 receivers available at the antenna, covering frequencies between 300 MHz and 90 GHz. Technical details on the receivers and observing modes can be found at: http://www.mpifr.de/div/effelsberg/receivers/receiver.html.

For all the observing modes, the calibration of Effelsberg data consists on applying successive corrections to T_A, accounting for the different sources of noise encompassed by T_{sys}. This can be done following four basic steps (Kraus, 2009):

FIGURE II.5: The Effelsberg 100 m radio telescope of the Max Planck Institut für Radioastronomie (MPIfR). Image courtesy of Marcel S. Pawlowski (Argelander Institute for Astronomy).

i) *Noise tube calibration.* This step consists in the periodic injection of a constant signal in the horn of the receiver. This is done to find out the noise contribution of the receiver itself in the measurements, and to correct T_A for this effect.

ii) *Opacity correction.* At $\nu \gtrsim 15\,\mathrm{GHz}$, the transmittance of the atmosphere is not optimal (see Fig. II.2). Hence, T_A has to be corrected by the attenuation of the atmosphere, taking into account the air mass ($AM = 1/\sin(EL)$) traversed by the incoming radio emission at different elevations (EL), and the zenith opacity (τ_z):

$$T_A' = T_A \left(e^{\tau_z AM} \right).$$

iii) *Gain-elevation correction.* Small scale distortions of the dish during the observations due to, e.g., changes in temperature and gravity effects, will distort the antenna pattern, thus causing a loss of sensitivity. These effects are described by the gain-elevation curve, $G(EL)$, and a correction to account for them has to be applied to the data:

$$T_A^* = \frac{T_A'}{G(EL)}.$$

iv) *Conversion from temperature units to flux density units.* The antenna temperature resulting from the process described above, can be converted into flux density following,

$$S(\mathrm{Jy}) = \frac{T_A^*(\mathrm{K})}{\Gamma(\mathrm{K/Jy})},$$

20

where Γ is the sensitivity of the radio telescope, and depends on the diameter of the antenna, and on the aperture efficiency, which is the ratio of the effective area, in the direction of the maximum gain, to the actual geometrical area.

II.1.3 Interferometric observations

This thesis deals mainly with radio interferometric observations of (U)LIRGs. In the following I give an overview on interferometry, principally based on Thompson *et al.* (2004), unless stated otherwise. I also introduce the radio interferometers used for the observations presented in Chapters III–VI of this thesis.

A radio interferometer is formed by two or more antennas separated from each other a few metres, up to thousands of kilometres (limited to the Earth's own size), observing the same source of radiation. This is equivalent to a large radio telescope, with the longest separation between antennas (maximum baseline) as diameter, hence allowing a better resolution than when observing with a single-dish. The beam of such a 'telescope', is called synthesised beam.

As explained in §II.1.2, in each antenna, the intercepted signal is converted into a voltage, which is amplified in order to be detected. To combine (multiply and average) the data from all the antennas involved in the observation in a constructive way, the phases of the antennas output signals must be aligned in the time-frequency plane, in order to maximise the combined amplitude (see Fig. II.6). This is the purpose of the so called correlation. For each pair of radio telescopes, the response to the incoming signal is the multiplication of the resulting voltages per unit time (correlated visibilities[1]) once frequency and time have been aligned. This gives rise to an interferometer pattern, whose structure changes as the Earth rotates, thus depicting the structure of the observed astronomical source through the use of the Fourier transform.

Typically, interferometers whose maximum separation between antennas is just a few kilometres, have their antennas wired connected (see §II.1.3.1). This situation eases the correlation process and is done in real time. On the other hand, interferometers whose antennas are separated by thousands of kilometres, defining the VLBI, present further difficulties. The processed signal by each antenna has to be time-tagged, with a high accuracy (normally using maser clocks), before being disk-recorded and brought to the location of the correlator, to be then finally correlated. Nevertheless, a colossal effort has made possible the real-time, high-speed communication between some antennas around

---

[1]The visibility is a mathematical function defined in the *uv*-plane, which results from the projection of the baseline vectors on the plane of the sky (x,y), and are given in wavelengths. The more antennas pairs are available, the better the *uv*-plane will be covered at a given time.

the world (see §II.1.3.2) by means of a wide system of optical fibre connections, permitting the real-time correlation between signals. This is the so called electronic VLBI.

The treatment of the data obtained with connected interferometers and through VLBI is somewhat different, but pursues the same goal: to recover the true brightness distribution (amplitude and phase) of the radiation source, taking as a starting point the measured visibilities which form the *uv*-plane.
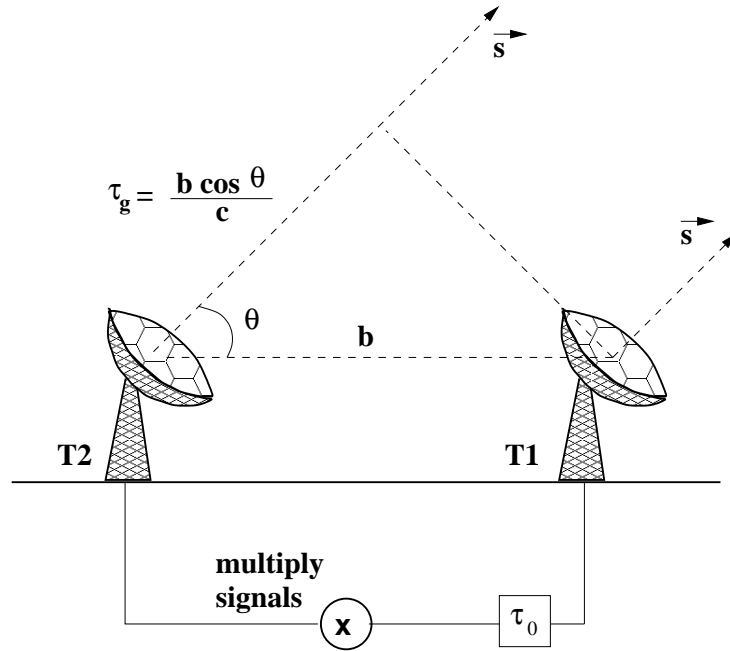
FIGURE II.6: The plane wave front coming from the direction $\bar{s}$ has a different arrival time at the different antennas (T1 and T2); this difference in time is called geometrical delay (τ_{g}). Additionally, the antennas move at different speeds as the Earth rotates, thus producing a Doppler shift effect. To compensate for these differences in delay and rate, thus having the signals from T1 and T2 arriving at the same time (i.e., interfering constructively) at the multiplier, we equalise their paths by introducing an artificial delay (τ_0) for antenna T1. this gives rise to an interference pattern with bright and dark fringes, such as in the Young's double slit experiment.

As mentioned above, in the correlation process the combination of antennas outputs has been made as to maximise the resulting signal. However, some residuals affecting the phases in time and frequency (rate and delay, respectively) might be left. The particularities of the electronic system of each antenna, plus different atmospheric (troposphere and ionosphere) conditions which are uncorrelated (especially in the VLBI case), as well as inaccurate positions for both target sources and the antennas themselves, are further sources of error in the visibilities. Additionally, when using antennas with altitude-azimuthal mounting, we need to take into account the rotation of the antenna feed with respect to the sky while slewing (parallactic angle), which introduces further errors in the phases. The so called fringe fitting procedure, corrects the visibility phases to account for the previously

mentioned issues, with the purpose of maximising the fringes.

Regarding the amplitude of the visibilities, an a priori calibration that takes into account the characteristics of each antenna and the environment surrounding the antenna (gain and system temperature) is needed. This is basically the same calibration followed when observing with single-dish (see §II.1.2.1). Then, we also have to apply corrections due to the response of the interferometer as a whole.

Each pair of antennas might be measuring different amplitudes due to their inherent electronic systems. To find out these differences, and thus calibrate the array, we need to observe additional sources besides the target source, called calibrators. An ideal calibrator is one which has the same amplitude as seen with the different baselines, i.e., with different angular resolution (and throughout the whole observing time and observed frequency interval), and to which a single phase is associated (equal to zero, if its position is coincident with the axis of the synthesised beam). It is also desired that the calibrator is strong (e.g., a few Jy). These requirements are fulfilled by unresolved sources such as quasars. However, the higher the frequency and the longer the baselines included in the array, the more difficult will be to find sources which are strong, unresolved, and non-variable. In addition, target sources are usually very faint and can display an extended structure and/or be composed of several sources, each of these with a different assigned phase. Thus, a phase reference calibrator source as close as possible (to ensure having the same atmospheric conditions) should be observed. The smaller is the angular separation between target and phase-reference calibrator, the better the phase-referencing will work.

II.1.3.1 Radio linked/connected interferometry

VLA - The VLA[2] was an array consisting of 28 antennas (25 m diameter) operated by the National Radio Astronomy Observatory (NRAO), and located in New Mexico, USA. Due to maintenance, only 27 antennas were available at a time for observations, thus, a total of 351 visibilities were produced per integration time (typically 10 sec). Eight different frequency bands were offered, covering frequencies between 73 MHz and 50 GHz.

The antennas were (and still are, for the upgraded array EVLA) distributed along three arms, simulating an inverted 'Y' shape pointing towards the North (Fig. II.7). Approximately every four months, the antennas are redistributed along each arm in the array, by changing the separation between antennas. These changes in configuration imply different angular resolutions. The basic configurations are called A ($B_{\mathrm{max}} = 36$ km), B ($B_{\mathrm{max}} = 11$ km), C ($B_{\mathrm{max}} = 3.4$ km) and D ($B_{\mathrm{max}} = 1$ km). Observing at 5 GHz with the

---

[2]The VLA has undergone a major upgrade and has been renamed as EVLA as of 2010. Information on the characteristics of the EVLA can be found at: https://science.nrao.edu/facilities/evla/index.

most extended configuration, results in a angular resolution of about 0.4 arcsec. There are also hybrid configurations (BnA, CnB and DnC), where the South-east and South-west arms have been changed to the next configuration, while the north arm continues to be in a more extended configuration. This is very useful when observing sources at low-declinations.

FIGURE II.7: The VLA. Image courtesy of NRAO/AUI and Photographer: John Littell.

MERLIN and e-MERLIN - The Multi-Element Radio Linked Interferometry Network (MERLIN) is an heterogeneous array of seven antennas[3], operated by the Science and Technology Facilities Council (STFC) and distributed over Great Britain, with a maximum baseline of about 215 km (see Fig. II.8). Comparing with the VLA at 5 GHz, MERLIN achieves about 10 times better angular resolution. Very recently, MERLIN started its transition to its upgraded version: the electronic Multi-Element Remotely Linked Interferometry Network (e-MERLIN), which is still in a commissioning phase. The main differences between the two arrays are:

i) The available observing bands: MERLIN operated at five different bands, covering frequencies between 150 MHz and 22 GHz, whereas e-MERLIN will offer three bands centred at 1.5, 5 and 22 GHz.

ii) The total bandwidth: 1 to 16 MHz for MERLIN vs. 4 GHz for e-MERLIN, thus increasing the sensitivity by a factor larger than 10.

---

[3]Four antennas (Mark II, Defford, Knockin, Darnhall and Pickmere) of 25 m of diameter, one of 32 m (Cambridge), and one of 76 m (Lovell).

iii) The connection between the radio telescopes: in MERLIN, the transmission of data from the different antennas to the correlator (based at Jodrell Bank), was made via microwave links. The signals were intercepted at a tower equipped with parabolic reflectors at Jodrell Bank, and locked to the hydrogen maser standard at Jodrell Bank for phase stability. e-MERLIN has now dedicated optical fibre connections between telescopes, so that transmission of data is faster and suffers less losses. This has permitted to increase substantially the bandwidth.

More details can be found at `http://www.merlin.ac.uk/` and `http://www.e-merlin.ac.uk/tech/`.
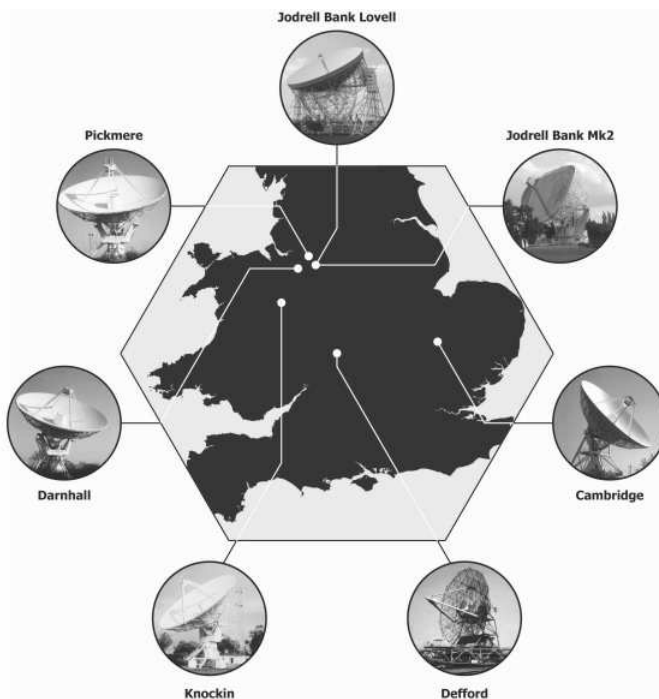
FIGURE II.8: The antennas distribution over UK of the MERLIN (and e-MERLIN) array. Credit: University of Manchester, STFC.

II.1.3.2 Very long baseline interferometry

Back in 1980, the quest for higher angular resolution motivated the foundation of the European VLBI Network (EVN) by five European radio astronomy institutes. The EVN continues to grow as more antennas join the effort. Nowadays, the EVN consists of 18 independent antennas (see Fig. II.9), most of them located in Europe, which work together in three sessions per year for a few weeks, in the so called VLBI sessions. In addition, the EVN often participates with other interferometers: together with MERLIN, it provides a better *uv*-coverage at short baselines, and together with the Very Long Baseline Array (VLBA) –Global VLBI–, or with HALCA[4] –Space VLBI– in the past, to pursue

---

[4]HALCA was a Japanese 8 m radio telescope, on board of a spacecraft, which operated between 1997 and 2003.

even higher angular resolution.

FIGURE II.9: Current EVN participating and associated stations. Credit: JIVE.

Due to the diversity of antennas in the EVN, different stations are available at different frequencies (see http://www.evlbi.org/user_guide/EVNstatus.txt), so that different EVN arrays are possible. Observations can be carried out at six main bands, which cover frequencies between ∼1.7 and 22 GHz. Maximum baselines above 8000 km (by including, e.g., the Chinese and/or South African antennas) allow angular resolution of a few mas. A sensitivity of the order of μJy/beam can be achieved when including very sensitive antennas in the array, such as Effelsberg and the Lovell radio telescopes.

The EVN, through the Express Production Real-time e-VLBI Service (EXPReS) project, has undertaken the great labour of connecting several radio telescopes around the world through an optical fibre network and thus provide real-time VLBI, with a data transfer ∼1 Gbps. This has given origin to the electronic EVN (e-EVN). Thirteen antennas are currently connected, and e-VLBI sessions are carried out regularly once per month.

Both EVN and e-EVN data are primarily correlated at the EVN MkIV Data Processor at the Joint Institute for VLBI in Europe (JIVE), based in the Netherlands.

II.2   Near-infrared observations

As seen in Fig. II.2, IR radiation is somewhat hampered by molecules in the troposphere. This effect can be alleviated by building telescopes on top of high mountains. Additionally, IR wavelengths are subject to dust extinction effects; this is less severe at

certain wavelengths, like those corresponding to the NIR. The most common bands in the NIR are called J, H, K and L, and are centred at 1.2, 1.7 , 2.2 and 3.5 μm approximately.

Unlike in radio, the NIR images have their pixel size as a measure of angular resolution; in radio, the pixel size merely represents a sampling of the beam size. Optical and IR telescopes are not diffraction-limited instruments, and the equivalent to the radio beam, called point spread function (PSF) in this case, is rather limited by the changes in the atmosphere, which distorts the wave front that arrives to the instrument. A technique called AO is currently used to diminish the distortions created by the atmosphere.

Gemini-N. The Gemini-North telescope (Frederick C. Gillett), part of the Gemini Observatory, is an 8.1 m diameter, altitude-azimuth mounted telescope located in Hawaii, USA (see Fig. II.10). The telescope is equipped with different instruments to perform observations in the optical, NIR and in the MIR. For this thesis, I made use of observations obtained with the instrument NIR imager (NIRI) which works with wavelengths between 1 and 5 μm. Three different cameras (f/32, f/14, and f/6) allow for three different angular resolutions (0.022, 0.050, and 0.117 arcsec pixel^{-1}) in the 1024×1024 NIRI detector array. The NIRI instrument can be used together with the AO system of the telescope, called ALTAIR. Further information can be found at
http://www.gemini.edu/sciops/instruments/?q=sciops/instruments.

FIGURE II.10: The Gemini-North telescope. Credit: Gemini Observatory/Association of Universities for Research in Astronomy.

CHAPTER III

ARP 299: A VERY WEALTHY MERGER

This chapter is devoted to our work on the LIRG Arp 299. §III.1 contains relevant information about this LIRG. §III.2 is based on observations with the e-EVN (published in Pérez-Torres *et al.*, 2009b), in which we investigate the compact radio sources within the brightest nucleus of Arp 299 (A). §III.3 is based on archival VLA data (published in Romero-Cañizales *et al.*, 2011), in which we revisit the CCSN rate in Arp 299 through the monitoring of flux density variability. In §III.4 I show complementary Gemini-N NIR observations (published in Romero-Cañizales *et al.*, 2011) as an attempt to detect the NIR counterpart of the nuclear SNe found by Pérez-Torres *et al.* (2009b).

III.1   The merging system Arp 299

Arp 299 is an early merger stage system (Keel and Wu, 1995) composed of the pair of galaxies IC 694 (east component) and NGC 3690 (west component), whose interaction is inducing a powerful SF (Alonso-Herrero *et al.*, 2000, and references therein). Four separate cores can be distinguished in VLA radio images of Arp 299 (see Figure III.1): A (IC 694), B (= B1 + B2) plus C (NGC 3690) and C′ (in the overlapping region). Hereafter we will refer to the NGC 3690-nucleus as B1, since this is the brightest core in that galaxy. In the same field of view (FOV) a probable background source named D is also found, which to our knowledge has not been detected in any radio spectral line observation made towards the system (see e.g., Casoli *et al.*, 1999; Aalto *et al.*, 1997), indicating that its redshift differs from that of Arp 299. In fact, source D was first detected at radio wavelengths by Huang *et al.* (1990) and identified as a probable SN, but Ulvestad (2009) has found that D has characteristics of a Palomar-Green (PG) quasar. The positions of the cores in Arp 299 and the probable background source D, as measured from the deep combined VLA image at 8.46 GHz (see Figure III.1), are listed in Table III.1.

At a luminosity distance of 44.8 Mpc ($H_0 = 73\,\mathrm{km\,s^{-1}\,Mpc^{-1}}$; Fixsen *et al.*, 1996), Arp 299 has an IR luminosity ($L_{\mathrm{IR}} = L[8\text{–}1000\,\mu\mathrm{m}]) \approx 6.7\times10^{11}\,\mathrm{L_\odot}$ (as resulting from
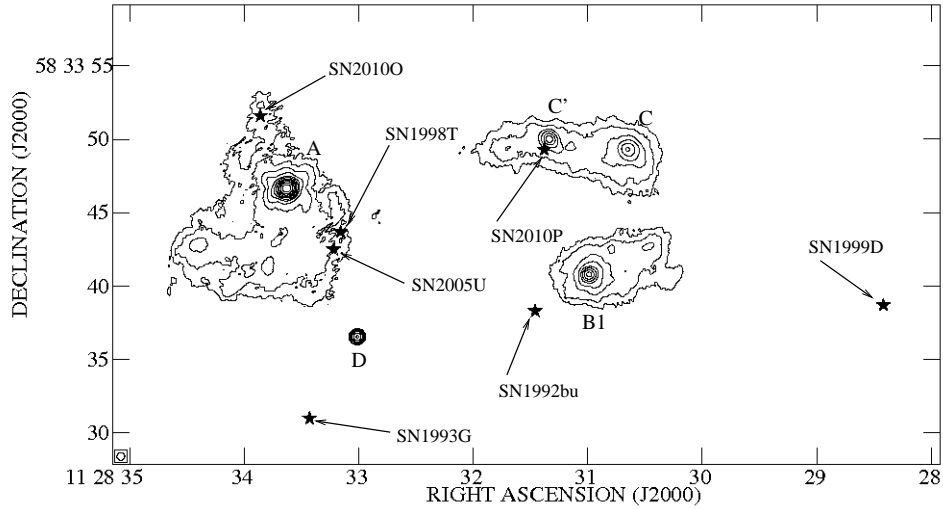
FIGURE III.1: Deep image of the 8.46 GHz radio continuum of Arp 299 resulting from combining (in the *uv*-plane) the archival VLA observations (11 epochs) which have an image rms < 150 μJy (see Table III.5). Cores A, B1, C′, and C are indicated, as well as the probable background source D (see Table III.1). The locations of previous optical and NIR SNe (see Table III.3) are indicated by five-pointed stars. The contours are $(3,3\sqrt{3},9,...)\times 45$ μJy/beam, the off-source rms flux density per beam. The restoring beam size is 0.54×0.52 arcsec^2 with a position angle of $80°$.

TABLE III.1: Positions of the Arp 299 cores measured from the image shown in Figure III.1 and their uncertainties. The position of the probable background source D is also given.

| Core | Peak Position | | $\Delta[\alpha,\delta]$ |
	α(J2000)	δ(J2000)	(mas)
A	11 28 33.626	58 33 46.65	0.2
B1	11 28 30.987	58 33 40.80	1.6
C′	11 28 31.332	58 33 50.00	4.5
C	11 28 30.648	58 33 49.30	5.8
D	11 28 33.013	58 33 36.55	5.6

TABLE III.2: Radio based SN rate estimates for nuclei A and B1.

| ν_{SN} (yr^{-1}) | | References | Notes |
A	B1		
0.65	0.12	Alonso-Herrero *et al.* (2000)	[1,2]
0.5 - 1.0	0.1 - 0.2	Neff *et al.* (2004)	[1]

[1]The estimates are based on VLA measurements.
[2]No errors have been reported for the given rates.

30

scaling the value for the same wavelength interval given by Sanders *et al.*, 2003, to the distance we adopted here), which makes it one of the most luminous LIRGs of the local Universe. Charmandaris *et al.* (2002) found that nucleus A emits approximately 40% of the total IR luminosity of Arp 299, whereas nucleus B1 accounts for approximately 20%. Making use of these estimates together with the empirical relation between CCSN rate and L_{IR} for starburst galaxies obtained by Mattila and Meikle (2001) (equation I.1), we have a total CCSN rate of $1.8\,\mathrm{yr}^{-1}$ for the whole system, and we expect SN rates of $\approx 0.7\,\mathrm{yr}^{-1}$ and $\approx 0.4\,\mathrm{yr}^{-1}$ for A and B1, respectively. These SN rates based on IR luminosity are similar for the nucleus A, but higher for nucleus B1, than those determined in previous studies (see Table III.2), which bear some dependency on the radio spectral behaviour of the cores. We notice though, that these IR luminosity based SN rate estimates assume no AGN contribution to the IR luminosity. However, the presence of AGNs in both nuclei is clear (see Pérez-Torres *et al.*, 2010; Alonso-Herrero *et al.*, 2009, for A and B1, respectively), and therefore the true SN rate could be lower than what has been estimated above.

Over the past 20 yr, Arp 299 has been the target of many SN search campaigns which can also provide important insight into its dominating energy source (AGN and/or starburst). In that period, a number of SNe have been detected in the circumnuclear regions at optical (Treffers *et al.*, 1993; Li *et al.*, 1998; Qiu *et al.*, 1999; Newton *et al.*, 2010) or NIR (van Buren *et al.*, 1994; Mattila *et al.*, 2005; Mattila and Kankare, 2010) wavelengths (see Table III.3). All of these SNe have been spectroscopically classified as core-collapse events of either type II or Ib, except SN 1992bu, whose type is unknown. The detection of seven SNe over a period of less than 20 yr, already indicates a very high SN rate in the circumnuclear regions of Arp 299. The relatively high fraction of stripped envelope SNe (types Ib/IIb) and their distribution with respect to the host galaxy properties are discussed in Anderson *et al.* (2011).

Very high resolution radio studies by Neff *et al.* (2004), Ulvestad (2009) and by our own group, Pérez-Torres *et al.* (2009b; 2010), have shown that at high angular resolution the brightest cores of the Arp 299 merger (A and B1), consist of a wealth of compact components within the innermost regions of these nuclei.

III.2 The prolific supernova factory in Arp 299-A

In 2008, we started an observing campaign with the e-EVN to monitor the nuclear region of Arp 299-A (PI: Pérez-Torres), given that this is the component that accounts for most of the IR and radio emission of the Arp 299 system, and it is thus the region that is most likely to reveal new SNe (Condon, 1992).

TABLE III.3: Optical and NIR Supernova history of Arp 299. The references covering discovery, type determination and position are given.

SN designation	Type	Position α, δ (J2000)
1992bu (NIR)[1]	-	11 28 31.46, 58 33 38.3[1]
1993G (optical)[2]	IIL[3]	11 28 33.43, 58 33 31.0[4]
1998T (optical)[5]	Ib[5]	11 28 33.16, 58 33 43.7[6]
1999D (optical)[7]	II[8]	11 28 28.42, 58 33 38.7[9]
2005U (NIR)[10]	IIb[11]	11 28 33.22, 58 33 42.5[10]
2010O (optical)[12]	Ib[13]	11 28 33.86, 58 33 51.6[12]
2010P (NIR)[14]	Ib/IIb[15]	11 28 31.38, 58 33 49.3[14]

[1]van Buren *et al.* 1994
[2]Treffers *et al.* 1993
[3]Tsvetkov 1994
[4]Forti *et al.* 1993
[5]Li *et al.* 1998
[6]Yamaoka *et al.* 1998
[7]Qiu *et al.* 1999
[8]Jha *et al.* 1999
[9]Prosperi 1999
[10]Mattila *et al.* 2005
[11]Modjaz *et al.* 2005; Leonard and Cenko 2005
[12]Newton *et al.* 2010
[13]Mattila *et al.* 2010
[14]Mattila and Kankare 2010
[15]Ryder *et al.* 2010b

Since optical and NIR observations are likely to miss a significant fraction of CCSNe in the innermost regions of Arp 299-A due to large values of extinction ($A_V \sim 34 - 40$, e.g., Gallais *et al.*, 2004; Alonso-Herrero *et al.*, 2009) and the lack of the necessary angular resolution, high sensitivity radio observations of Arp 299-A at high angular resolution are the only way of detecting new CCSNe and measuring directly and independently of models its CCSN and SF rates. In fact, VLBA observations carried out during 2002 and 2003 resulted in the detection of five compact sources (Neff *et al.*, 2004), one of which (A0) was identified as a young SN.

III.2.1 e-EVN observations: data calibration and analysis

We observed Arp 299-A at a frequency of 5 GHz with the e-EVN on 8-9 April 2008 (experiment code RP009) and on 5 December 2008 (experiment code RP014A), aiming at directly detecting recently exploded CCSNe through the variability of their individual radio emission.

The first epoch of observations included the following antennas (location, diameter):

Cm-Cambridge (UK, 32 m), Mc-Medicina (Italy, 32 m), Jb1-Lovell (UK, 76 m), On-Onsala (Sweden, 25 m), Tr-Torun (Poland, 32 m), and Wb-Westerbork array (NL, 14×25 m). Our second observing epoch included additionally Ef-Effelsberg (Germany, 100 m), Kn-Knockin (UK, 25 m) and Sh-Shanghai (China, 25 m).

Both epochs were phase-referenced experiments, using a data recording rate of 512 Mbps with two-bit sampling, for a total bandwidth of 64 MHz. The data were correlated at the EVN MkIV Data Processor at JIVE using an averaging time of 1 s. The first consisted of ∼8.0 hr on target. The telescope systems recorded both left-hand circular polarisation (LCP) and right-hand circular polarisation (RCP) which, after correlation, were combined to obtain the images shown in Figure III.2. Scans of 4.5 min for our target source, Arp 299-A, were alternated with 2 min scans of our phase reference source, J1128+5925 (0.86°, projected distance from the target). Both 3C345 and 4C39.25 were used as fringe finders and band-pass calibrators. Our second epoch consisted of ∼4.5 hr on target. The telescope systems also recorded in dual polarization, and 4.5 min on-source scans were alternated with 1 min scans of J1128+5925. The bright sources 3C84, 3C138, 4C39.25 and 3C286 were used as fringe finders and band-pass calibrators.

We analysed the correlated data for each epoch using the NRAO Astronomical Image Processing System (AIPS). The visibility amplitudes were calibrated using the system temperature and gain information provided for each telescope. Standard inspection and editing of the data were done within AIPS. The bandpasses were corrected using the bright calibrator 4C39.25. We applied standard corrections to the phases of the sources in our experiment, including ionosphere corrections (using total electron content measurements publicly available).

Because of the limited bandwidth of Cm and Kn, the usable data of these antennas was found in a single subband with very noisy edges. To improve the quality of the bandpass calibration, we removed the edges of Cm for the first epoch, and the edges of Cm and Kn for the second epoch. After fringe-fitting, the data of the different calibrators were exported to the Caltech program for differential mapping (DIFMAP) to test the performance of each antenna and to determine gain corrections, which were then applied to the data within AIPS.

The fringe solutions (delays and rates) determined for J1128+5925 were interpolated and applied to the source Arp 299-A. J1128+5925 is essentially point-like at the angular resolution (≲9 mas) provided by our 5 GHz e-EVN observations, and its phase-contribution to the solutions is therefore negligible.

The imaging of Arp 299-A was done with the AIPS task IMAGR (Figure III.2), using natural weighting and a ROBUST parameter equal to zero. We attained an off-source

root-mean-square (rms) noise level of 39 and 24 μJy/beam for the 8 April 2008 and 5 December 2008 observations, respectively. The higher sensitivity achieved in the second epoch is primarily due to the addition of Ef to the observing array, over compensating the significantly smaller amount of total observing time.

Our e-EVN observations resulted in the detection of various compact sources. We considered as real sources those resulting in a signal to noise ratio (SNR) equal to, or above five times the rms in either of our two observing epochs. The higher sensitivity achieved in the second epoch allowed the detection of a larger number of compact components (26) with respect to the first epoch (15). We placed small boxes across the 8 April 2008 image, around the positions of those components detected on 5 December 2008, to extract the flux density of the counterparts initially detected only in the second epoch (components A15 through A25 in Figure III.2). This procedure allowed us to recover four components above 3σ (A15, A18, A22, and A25), based on a positional coincidence with the peak of emission in our second epoch with better precision than 0.5 mas; and for those components not detected on 8 April, to derive 3σ upper limits for the emission.

The flux density extraction was done using the task IMFIT within AIPS, by fitting a Gaussian component to each source. Since all the sources are unresolved, the integrated flux densities coincide with the peak intensities. The flux density values (S_{tot}) are listed in III.4. Since it was not possible to obtain deconvolved sizes for most of the sources, we calculate lower limits to the brightness temperature (T_{B}) of each source, using as their subtended solid angle that corresponding to the beam size (see Appendix B), i.e., $\Omega_{\text{s}} = \pi \, (4\log 2)^{-1} \, (\text{FWHM}_{\text{M}} \times \text{FWHM}_{\text{m}})$.

III.2.2 Results from the e-EVN observations

Our observations reveal the existence of 26 compact components above 5σ (see Figure III.2), 15 of which were detected on our first epoch, and 25 on the second epoch. In Figure III.2 we show a VLA image that helps to place within the Arp 299 system, the compact components we detected in this study, and the images resulting from our high angular resolution e-EVN observations.

Our results demonstrate the existence of a very compact rich nuclear starburst in Arp 299-A which in general, are in excellent agreement with independent results reported by Ulvestad (2009). The angular size encompassed by the radio emitting sources in Arp 299-A is less than $0.7 \times 0.4 \, \text{arcsec}^2$, corresponding to a projected linear size of $150 \times 85 \, \text{pc}$. To ease comparisons, we define a fiducial supernova radio luminosity equal to three times the image rms in the 8 April 2008 epoch, which corresponds to $2.9 \times 10^{26} \, \text{erg s}^{-1} \, \text{Hz}^{-1}$. In this way, the radio luminosities for the VLBI components range between 1.1 (A25) and

TABLE III.4: Compact radio emitting sources in the central region of Arp 299-A. *Notes:* [a]Coordinates are given with respect to α(J2000)= $11^h28^m33^s.0000$ and δ(J2000)= $58°33'46''.000$, and were obtained from the 5 December 2008 image. The positions for those sources also detected in 8 April 2008 coincide within the errors ($\lesssim 0.5$ mas) with all of them. [b]The uncertainty in the reported flux density for the detected compact components corresponds to 1σ, where σ was determined by adding in quadrature the off-source rms in each image and a 5% of the local maximum, to conservatively account for possible inaccuracies of the e-EVN calibration. [c]We define the significance of the flux density variability between the two consecutive epochs as $V = | S_{\mathrm{Dec}} - S_{\mathrm{Apr}} | / \sqrt{\sigma_{\mathrm{Dec}}^2 + \sigma_{\mathrm{Apr}}^2}$, where S_{Apr} and σ_{Apr} (S_{Dec} and σ_{Dec}) are the values in columns 5 and 6 (9 and 10), respectively. [d] Source names are given in right ascension order, except for the five components reported previously (A0 through A4) by Neff *et al.* (2004).

Source Name[d]	Source Type	$\Delta\alpha$[a] (J2000)	$\Delta\delta$[a] (J2000)	S_{tot} (μJy)[b] 8 Apr 2008	5 Dec 2008	$\log[T_B(K)] >$ 8 Apr 2008	5 Dec 2008	L_ν (10^{26} erg s^{-1} Hz^{-1}) 8 Apr 2008	5 Dec 2008	V[c]
(1)	(2)	(3)	(4)	(5)	(6)	(7)	(8)	(9)	(10)	(11)
A0	SN	0.6212	0.707	318±42	446±33	5.5	5.5	7.9±1.0	11.1±0.8	2.4
A1	SNR	0.6199	0.699	855±58	901±51	6.0	5.8	21.3±1.4	22.4±1.3	0.6
A2	SNR	0.6219	0.655	708±53	713±43	5.9	5.7	17.6±1.3	17.7±1.1	0.1
A3	SNR	0.5942	0.560	398±44	353±30	5.6	5.4	9.9±1.1	8.8±0.7	0.8
A4	SNR	0.6501	0.537	558±48	628±40	5.8	5.6	13.9±1.2	15.6±1.0	1.1
A5	SN?	0.6176	0.693	278±41	143±25	5.5	5.0	6.9±1.0	3.6±0.6	2.8
A6	SN	0.6206	0.597	208±40	≤72	5.3	4.7	5.2±1.0	≤1.8	3.4
A7	SNR	0.6300	0.786	496±46	468±34	5.7	5.5	12.3±1.2	11.6±0.8	0.5
A8	SNR	0.6306	0.401	226±41	264±27	5.4	5.3	5.6±1.0	6.6±0.7	0.8
A9	SNR	0.6306	0.620	294±42	282±28	5.5	5.3	7.3±1.0	7.0±0.7	0.2
A10	SNR	0.6392	0.551	550±48	436±32	5.8	5.5	13.7±1.2	10.9±0.8	2.0
A11	SNR	0.6403	0.583	300±42	351±30	5.5	5.4	7.5±1.0	8.7±0.7	1.0
A12	SN	0.6495	0.590	449±45	639±40	5.7	5.6	11.2±1.1	15.9±1.0	3.2
A13	SN?	0.6531	0.733	251±41	118±25	5.4	4.9	6.2±1.0	2.9±0.6	2.8
A14	SNR	0.6825	0.571	292±42	260±27	5.5	5.2	7.3±1.0	6.5±0.7	0.6
A15	SN	0.5991	0.638	159±40	304±28	5.2	5.3	4.0±1.0	7.6±0.7	3.0
A16	uncl.	0.6149	0.516	≤117	147±25	5.1	5.0	≤2.9	3.7±0.6	1.2
A17	uncl.	0.6179	0.561	≤117	179±26	5.1	5.1	≤2.9	4.5±0.6	2.4
A18	uncl.	0.6192	0.464	151±40	129±25	5.2	4.9	3.8±1.0	3.2±0.6	0.5
A19	SN?	0.6196	0.659	≤117	191±26	5.1	5.1	≤2.9	4.8±0.6	2.8
A20	uncl.	0.6278	0.789	≤117	146±25	5.1	5.0	≤2.9	3.6±0.6	1.2
A21	uncl.	0.6291	0.836	≤117	133±25	5.1	5.0	≤2.9	3.3±0.6	0.6
A22	uncl.	0.6354	0.678	173±40	217±26	5.3	5.2	4.3±1.0	5.4±0.7	0.9
A23	uncl.	0.6360	0.560	≤117	137±25	5.1	5.0	≤2.9	3.4±0.6	0.8
A24	uncl.	0.6361	0.764	≤117	166±25	5.1	5.1	≤2.9	4.1±0.6	2.0
A25	SN?	0.6524	0.701	132±40	209±26	5.1	5.2	3.3±1.0	5.2±0.7	1.6
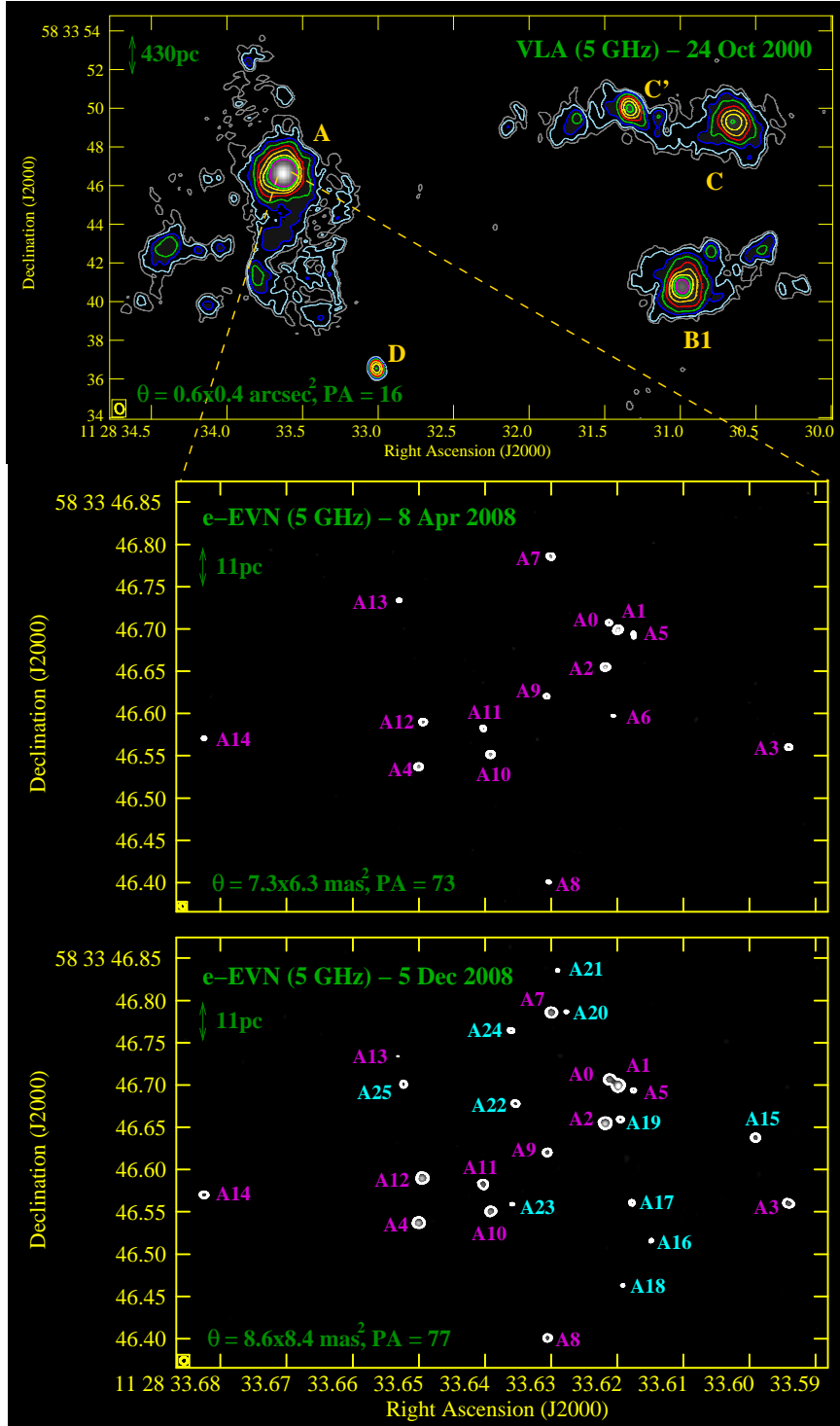
FIGURE III.2: *Top:* Contour map of VLA archival observations of the merging system Arp 299 on 24 October 2000 at 5 GHz (convolving beam: $0.6 \times 0.4 \, \text{arcsec}^2$ at a position angle of 16°), displaying the different radio emission components. The contours are $(3, 3\sqrt{3}, 9, ...) \times 22 \, \mu\text{Jy beam}^{-1}$, the off-source rms. *Middle and bottom:* Contour maps of the e-EVN observations on 8 April and 5 December 2008 towards Arp 299-A. The convolving beam was $7.3 \times 6.3 \, \text{mas}^2$ at 73° in the first epoch, and $8.6 \times 8.4 \, \text{mas}^2$ at 77° in the second. To guide the reader's eye, we show in cyan the components detected only on the 5 December 2008 epoch.

7.3 (A1), and between 1.0 (A13) and 7.7 (A1) times the fiducial value, for the VLBI observations on 8 April 2008 and 5 December 2008, respectively (see Table III.4 for details).

III.2.3   The radio emission of the compact sources in Arp 299-A

The radio emission from the compact sources detected in our VLBI observations can be explained in principle within two different physical scenarios: (i) thermal radio emission from super star clusters (SSCs) hosting large numbers of HII regions (where massive SF is taking place); (ii) non-thermal radio emission from young RSNe and/or SNRs, i.e., synchrotron radio emission originated by the interaction of SN ejecta with the surrounding CSM (SNe), or with dense ISM (SNRs).

The existence of SSCs in Arp 299-A is inferred by their apparent detection with 2.2 μm AO imaging (Lai *et al.*, 1999). Further evidence comes from *HST* Faint Object Camera (FOC) and Near Infrared Camera and Multi-Object Spectrometer (NICMOS) images, which reveal a population of young stellar clusters (4–15 Myr) in the central regions of Arp 299 (Alonso-Herrero *et al.*, 2000). The total 5 GHz radio luminosity in compact sources is 1.7×10^{28} erg s^{-1} Hz^{-1} and 2.0×10^{28} erg s^{-1} Hz^{-1} on the first and on the second epoch, respectively. However, the high flux densities and small sizes of the compact sources in Arp 299-A indicate T_B values (see Table III.4) which greatly exceed the thermal temperatures expected from SSCs ($\lesssim 2 \times 10^4$ K), thus ruling out a thermal origin for the compact radio emission traced by our e-EVN observations.

The observed radio emission must be generated by young RSNe, SNRs, or both. In Table III.4 we show the flux densities, brightness temperatures and luminosities of all the components identified in our observations, and classify the objects according to their variability. The majority of sources do not show any evidence of significant variability, which is consistent with their identification as SNR. Only three sources (A6, A12, and A15) show appreciable flux density variations between our two consecutive e-EVN observations (see Table III.4 for details), which is very difficult to reconcile with their radio emission being due to SNRs. Sources A6, A12, and A15 are also detected in previous VLBI observations carried out between 2003 and 2005 by Ulvestad (2009). A15 is detected at 8.4 GHz but not at 2.3 GHz by Ulvestad (2009). From this fact, and our clear detection with an increasing flux density over two epochs at 5 GHz, we can infer that A15 is a relatively recent, slowly evolving RSN. This behaviour is very similar to that displayed by A0 (see below). Similarly, source A12 increases in flux with time at 5 GHz; and since it was also previously detected in 2003 and 2005, it is likely a relatively recent and slowly evolving RSN too. The nature of A6 is less clear. Ulvestad (2009) detected A6 only at 2.3 GHz. This detection, together with the sudden drop in its 5 GHz flux density between April

and December 2008 may be interpreted as the result of a CCSN leaving its young RSN phase (when it is powered by interaction with the CSM) to enter the SNR phase (when it is powered by interaction with the ISM). We cannot exclude, however, the possibility that A6 is an X-ray binary or a micro-quasar. In fact, A6 is quite close to two X-ray sources reported by Zezas *et al.* (2003) (sources 14 and 16 in their table 1). The combined absorption corrected X-ray luminosity of those sources is $\sim 1.9 \times 10^{40}$ erg s^{-1}. From the luminosity at 5 GHz of A6 in Table III.4, and assuming a spectral index of $\alpha = -0.5$ (typical of micro-quasars), the approximate total radio luminosity is $\sim 4.8 \times 10^{36}$ erg s^{-1}, resulting in a ratio of radio-to-X ray luminosity of $\sim 2.5 \times 10^{-4}$, which is a bit high, but still consistent with A6 being a micro-quasar.

The maximum 5 GHz luminosities inferred by A12 and A15 are of $\sim 1.6 \times 10^{27}$ and $\sim 7.6 \times 10^{26}$ erg s^{-1} Hz^{-1}, respectively. These are typical values of radio emitting Type IIP, or Type IIb SNe (Chevalier *et al.*, 2006). If confirmed, it would be the first time that such relatively faint radio SNe have been detected in the nuclear starburst of a local (U)LIRG. For comparison, Arp 220 appears to contain essentially very bright RSNe, which are identified with Type IIn RSNe (Parra *et al.*, 2007). We note here that this is not simply a sensitivity issue, since some of the VLBI observations of Arp 220 had rms as low as 9 μJy/beam (Parra *et al.*, 2007), yet most of the objects detected there were identified, based on their large radio luminosities, as Type IIn SNe. We cannot exclude, however, that A12 and A15 have not yet reached their peak. In that case, their (peak) radio luminosity could be a few times higher, and given their slow evolution, these SNe could be Type IIL, or even Type IIn.

In a previous paper, Neff *et al.* (2004) reported the detection of five VLBI sources (A0 to A4), within the central $\sim$80 pc of Arp 299-A. We detect all of these components at 5 GHz. Components A1 to A4 do not show significant variability in the eight months covered by our 5 GHz e-EVN observations, which is consistent with them being young SNRs, as also suggested by Ulvestad (2009).

A0 was first detected at 8.4 GHz, and identified with a radio supernova by Neff *et al.* (2004). We have now detected it at 5 GHz, more than five years after its discovery at 8.4 GHz. This implies that A0 is a long-lasting, slowly-evolving, non-standard radio supernova, since most other examples evolve more rapidly (Weiler *et al.*, 2002). Although rather uncommon, there are similar cases reported in the literature, both in normal galaxies, e.g., SN 1979C in M100 (Montes *et al.*, 2000), and in (U)LIRGs, like some of the RSNe in Arp 220 (Parra *et al.*, 2007). In addition, its non-detection at 2.3 GHz up to 2005 (Ulvestad, 2009) suggests the presence of a foreground absorber (e.g., a nearby HII region), as in the case of SN 2000ft in the LIRG NGC 7469 (Alberdi *et al.*, 2006; Pérez-Torres *et al.*, 2009a). Finally, we note that A5 may also have similar properties, although its variability

significance is lower. In short, the behaviour displayed by A0 (and A5) whilst unusual, is not unknown for RSNe, and provides important information about how the interaction between the SN ejecta and CSM is proceeding, and thus probes the mass-loss history of the progenitor star. We therefore suggest that it is the local CSM conditions which are primarily responsible for determining the luminosity of the RSNe exploding in the nuclear starburst of Arp 299-A.

III.3 The core-collapse supernova rate in Arp 299 revisited

Arp 299 has been observed with VLBI techniques only since 2003 (Neff *et al.*, 2004), and thus the appearance of new sources in its nuclear regions before 2003 has gone unnoticed. We have therefore carried out a study using the available data in the VLA archive aiming at measuring the ν_{SN} in the Arp 299 nuclei through the study of their flux density variability. Our method is particularly efficient in the B1-nucleus, where the radio surface brightness is lower, hence allowing us to detect small variations in the overall nuclear flux density, which can be related to SN activity. In fact, this kind of study has been successfully applied to M82, where a strong radio flare on top of the diffuse emission of the host galaxy was identified with SN 2008iz (Marchili *et al.*, 2010).

III.3.1 VLA archival data - Reduction and analysis

Arp 299 has been observed repeatedly with the VLA over the last decades in X-band (8.46 GHz). However, archival data lack homogeneity in frequency and resolution and do not cover an adequate time period at regular intervals, making the estimates of ν_{SN} more challenging.

The X-band VLA observations in A-configuration, provide us with a resolution of a few tenths of an arcsecond, enough to easily distinguish the emission from the different cores in Arp 299, but not to resolve each nucleus into the individual components. In fact, as we have mentioned in §III.1, the nuclei A and B1 both consist of several compact sources (Pérez-Torres *et al.*, 2009b, and references therein). Therefore, care must be taken while interpreting flux density measurements at VLA resolutions, which do not resolve out each core into their individual sources.

Our aim is to further investigate the available archival data to extract information on the SN activity in Arp 299, despite the difficulties both in extracting and interpreting the information from VLA images. We have analysed high resolution, X-band VLA data from

TABLE III.5: Properties of the VLA images and estimated flux densities at X-band ($\nu \sim 8.46\,\mathrm{GHz}$), S_{tot}, for the radio light curves of nuclei A and B1 (see Figure III.3(a)). The peak intensities, S_{peak}, for each nucleus are also given. The flux density and peak intensity uncertainties have been computed by adding in quadrature the rms noise in the map (sixth column), plus a conservative 5% uncertainty in the point source calibration. We have used a common uv-range of 23.6 to 261.9 kλ for all the epochs, and $0.78 \times 0.73\,\mathrm{arcsec}^2$ at 19° as the convolving beam.

	Date	VLA config.	Programme	Weighting	rms (μJy/beam)	$S_{\mathrm{peak}}^{\mathrm{A}}$ (mJy/beam)	$S_{\mathrm{tot}}^{\mathrm{A}}$ (mJy)	$S_{\mathrm{peak}}^{\mathrm{B1}}$ (mJy/beam)	$S_{\mathrm{tot}}^{\mathrm{B1}}$ (mJy)
1	1990-02-24	A	AH396	natural	148.4	64.74±3.24	83.66±4.19	7.52±0.40	9.89±0.52
2	1990-03-04	A	AH396	natural	89.3	62.77±3.14	79.46±3.97	7.55±0.39	9.60±0.49
3	1991-07-05	A	AS333	natural	93.3	62.26±3.11	81.87±4.09	8.09±0.41	11.23±0.57
4	1993-01-28	BnA	AS333	natural	73.4	62.32±3.12	81.71±4.09	7.91±0.40	12.29±0.62
5	1993-05-07	B	AS333	uniform	294.8	61.56±3.09	78.94±3.96	7.95±0.50	11.34±0.64
6	1994-05-16	BnA	AY064	natural	38.6	64.20±3.21	82.12±4.11	7.81±0.39	10.39±0.52
7	1999-10-28	B	AS568	uniform	70.8	56.25±2.81	77.21±3.86	7.57±0.38	9.92±0.50
8	2001-03-19	B	AN095	uniform	37.4	63.35±3.17	83.03±4.15	8.38±0.42	12.48±0.62
9	2002-04-29	A	AN103	natural	207.7	63.08±3.16	82.78±4.14	7.14±0.41	10.46±0.56
10	2002-09-06	B	TYP04	uniform	332.1	60.79±3.06	76.37±3.83	7.35±0.50	10.25±0.61
11	2003-10-17	BnA	AS779	uniform	36.9	66.94±3.35	82.54±4.13	7.97±0.40	11.48±0.57
12	2004-11-02	A	AC749	natural	31.5	65.85±3.29	84.37±4.22	7.80±0.39	10.90±0.55
13	2005-02-08	BnA	AW641	uniform	103.5	65.46±3.27	84.58±4.23	8.19±0.42	12.23±0.62
14	2006-04-15	A	AC749	natural	131.6	58.83±2.94	77.39±3.87	15.47±0.78	17.28±0.87

1990 to 2006 (see Table III.5) to study the flux density variations of the Arp 299 nuclei. The VLA data were reduced following standard procedures with the NRAO AIPS programme. The intensity scale was set by observations of 3C48 in the case of project TYP04, and 3C286 for all the other projects. At X-band, these sources have an adopted flux density around 3.2 and 5.2 Jy, respectively (Baars et al., 1977).

Most of the studied epochs have been previously analysed by Neff et al. (2004) and Ulvestad (2009). The main difference with the previous studies is that we have estimated the flux densities in a consistent way by extracting them from maps created with matched baselines (in wavelengths) and with the same convolving beam (0.78×0.73 arcsec^2 at $19°$). We chose a common uv-range of 23.6 to 261.9 kλ for all our maps in order to properly compare among different observing epochs, thus avoiding systematic effects. Such restriction in the uv-range implies a suppression of structures larger than ≈ 8.7 arcsec and smaller than ≈ 0.8 arcsec. Moreover, to match the resolutions of the different observations, we applied natural weighting to those images with better resolution (those made in the VLA-A configuration) and uniform weighting to images with worse resolution (those made in the VLA-B configuration). For the hybrid BnA observations, we applied a uniform weighting to images having an intrinsically worse resolution than the chosen convolving beam, and a natural weighting to images having a better resolution than this.

We ran a series of phase-only self-calibration iterations in each epoch to achieve a better signal to noise ratio. All the images were centred at $11^h28^m33^s$, $+58°33'43''$, and the AIPS task PBCOR was applied in each one of the final images to correct for the primary beam attenuation.

We estimated the flux densities of the nuclei in each image by enclosing the emission above 7σ in a box and fitting a single Gaussian, using the AIPS task IMFIT. In each epoch, such box had an area of $\approx 500 \times 500$ pc^2 for the A-nucleus, and $\approx 400 \times 400$ pc^2 for the B1-nucleus, thus covering the circumnuclear regions in each case, where we expect the SNe and the possible AGN activity to take place. The angular size of these regions is such that fitting a single Gaussian is suitable.

Table III.5 contains the observing parameters of each epoch and the estimated values obtained always from the last image resulting from the self-calibration process, but corrected by the beam attenuation.

III.3.2 Tracing the nuclear activity in Arp 299 through flux density variations

Figure III.3(a) shows the light curves of nuclei A and B1, scaled to the same flux density level (the one of B1) to allow comparison. We note that the B1-nucleus exhibits conspicuous flux density variations. In contrast, the A-nucleus does not show systematic variations and remains relatively constant throughout the period of time comprised in our study, taking into account the observational uncertainties. We have also attested that the use of different phase calibrators has no influence on the flux density variations we see in B1. Furthermore, as we show in Figure III.3(a), the flux density variations of nucleus B1 are not correlated with those of nucleus A, and we have checked that the same is also true with the other cores present in the region, i.e., C, C′ and D.

To quantify the flux density variations we see in nucleus B1, we have made an iterative selection of the lowest data points to obtain a baseline value for B1, and compared each epoch's flux density with respect to the obtained baseline value.

As a starting point, we defined an initial baseline value for the B1-nucleus flux densities given by $\langle S \rangle \pm \delta S$, where $\langle S \rangle$ is the mean of the 14 S_{tot} values and δS is the standard error of the mean. We then determined the deviation of the flux density in each epoch (i) from the baseline value, with

$$dS_i = \frac{S_{\text{tot},i} - \langle S \rangle}{\delta S}.$$

The same was done for nucleus A. In the next step we excluded the epochs having $dS_i > 3$ and proceeded to calculate a new baseline value. We followed this iterative process until no more epochs could be removed by another iteration, thus leading to a robust baseline value.

After the third iteration, we find that the flux densities of the B1-nucleus on epochs 1, 2, 6, 7, 9 and 10, are representative of a quiescent state. Thus, considering the fluxes of these epochs, we obtain a final baseline value of $\langle S^{\text{B1}} \rangle \pm \delta S^{\text{B1}} = 10.08 \pm 0.22$ mJy for B1. For nucleus A, only epochs 13 and 12 were found to be above three times the standard error of the mean after the second iteration, and we have consequently obtained a baseline value of $\langle S^{\text{A}} \rangle \pm \delta S^{\text{A}} = 80.59 \pm 1.16$ mJy for A. Taking the ratio of the final A and B1 nuclei baselines values, we obtain a scaling factor for A of ~ 0.125, that allows comparison with B1 (see Figure III.3(a)).

To attest the significance of the variability for each epoch in each nucleus, we calculated again the deviation of each epoch but this time using the standard deviation of the final baseline for each nucleus: $\sigma_{\text{A}} = 2.57$ mJy and $\sigma_{\text{B1}} = 0.34$ mJy. We found that the flux densities of all the epochs in the A-nucleus show no significant deviations from the mean

value ($< 3\sigma_A$), due to the strong diffuse emission. For the B1 nucleus, epochs 3, 4, 5, 8, 11, 13 and 14 (following the numeration from Table III.5) are all above $3\sigma_{B1}$, and of these, epochs 4, 8, 13 and 14 are also above $5\sigma_{B1}$. Epoch 12, not being part of the baseline, has a variation slightly below $3\sigma_{B1}$, and hence it lacks of significance according to our detection threshold. Epochs 3 and 5 appear to be connected with the variation present in epoch 4, so we consider all these three epochs as having the same origin. Epoch 11 has less significant variability on its own and seems to share a similar behaviour with the epoch 11 in A (see Figures III.3(b) and III.3(c)), so its significance is further reduced due to a possible systematic effect in that epoch.

III.3.2.1 Flux density variability of the A-nucleus

Tracing the SN activity of nucleus A through its radio flux density variations is not feasible. This is because the flux density of the core A at these angular scales is not dominated by the individual SNe, but by the diffuse emission of the strong starburst therein, thus resulting in the relative quiescence of the total flux density (see Figure III.3(b)).

We note that typical RSNe at the distance of Arp 299 have flux densities comparable to the given uncertainties in the nuclear flux density (see column 7 of Table III.5), and thus to the obtained standard deviation, σ_A, in our variability test. Hence, it was not possible to detect SNe in the A-nucleus using this method. Furthermore, the minimum flux density for an event to be robustly detected with $5\sigma_A$ above the mean, would be $\sim 12.85\,\mathrm{mJy}$. At the distance of Arp 299, such flux density implies $L \sim 3.1 \times 10^{28}\,\mathrm{erg\,s^{-1}\,Hz^{-1}}$ at the peak, which is uncommon for normal CCSNe (see Figure III.4). With our method, we are able to detect only very bright SN events (such as powerful type IIn or 98bw-like events), which do not seem to be common in the A-nucleus. Indeed, the luminosities for the SN candidates found by Pérez-Torres et al. (2009b), range between $\approx 3 \times 10^{26}$ and $\approx 2 \times 10^{27}\,\mathrm{erg\,s^{-1}\,Hz^{-1}}$ (typical of type IIb, IIP and IIL SNe), and are thus well below our detection limit. Thus, in the absence of VLBI observations, the only feasible alternative to detect new SNe in nucleus A is by means of NIR observations (see §III.4).

Pérez-Torres et al. (2010) identified a compact source (A1, Figure III.2) as the core of a LLAGN in Arp 299-A (see also Figure IV.1 in Chapter IV). Its flux density at 5 GHz has remained below $\sim 1\,\mathrm{mJy}$ in observations carried out in 8 April 2008, 5 December 2008 (Pérez-Torres et al., 2009b) and in 7-8 June 2009 (Pérez-Torres et al., 2010). In fact, typical LLAGNs display at most flux density variations $\simeq 0.8$ times the average flux density (see Figure 2 from Nagar et al., 2002). Even if the LLAGN doubles its radio luminosity at a given time, we would not be able to detect such a burst in nucleus A since our flux density uncertainties are higher than $2\,\mathrm{mJy}$ in any given epoch (see Table III.5).
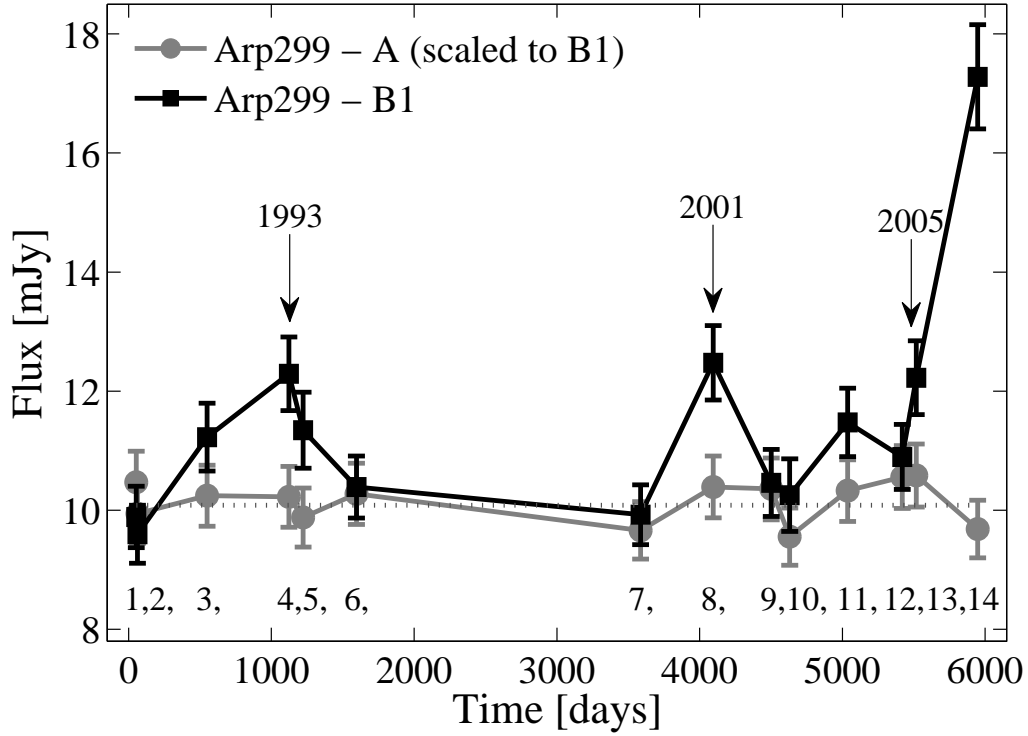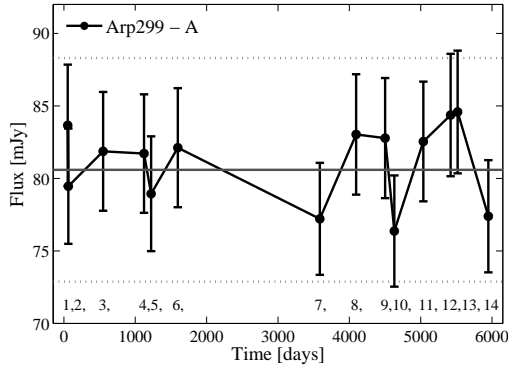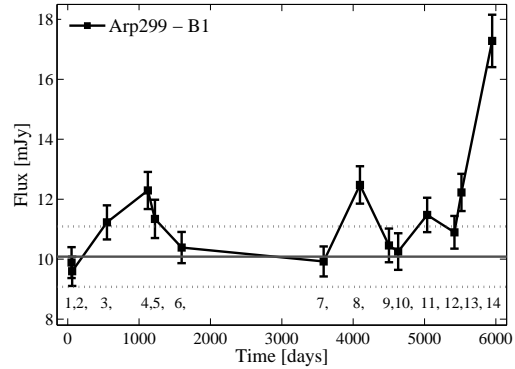
FIGURE III.3: (a) Arp 299-A light curve (solid line with circular markers) and -B1 (solid line with squared markers) at X-band. The labelling numbers correspond to those of Table III.5. The Arp 299-A flux densities have been scaled to the B1-nucleus baseline value (dotted line) for comparison. The scaling factor used is ~ 0.125. The epoch zero days corresponds to 1 January 1990. Figures (b) and (c) show the actual flux measurements for nuclei A and B1, respectively. In both Figures, the solid line represents the baseline value (80.59 ± 1.16 mJy for nucleus A, and 10.08 ± 0.22 mJy for nucleus B1) and the dotted lines denote the $+3\sigma$ and -3σ levels, σ being the standard deviation: 2.57 mJy for A and 0.34 mJy for B1. We note that all the epochs in A are well contained within the $\pm 3\sigma_{\mathrm{A}}$ region and essentially all the epochs represent the baseline level, whereas in B1 a number of epochs show significant variation $> 3\sigma_{\mathrm{B1}}$.

TABLE III.6: Properties of the variability events in the B1-nucleus, found during a ~11 yr period of VLA observations at 8.46 GHz.

Event	S_{peak} (mJy)	L_{peak} (10^{27} erg s^{-1} Hz^{-1})	t_{peak} (yr)
1993	> 2.21±0.66	> 5.31±1.58	<2
2001	> 2.40±0.66	> 5.76±1.58	<1.3
2005	> 7.20±0.90	> 17.29±2.16	>1.5

III.3.2.2 The nature of the radio variability of nucleus B1

As mentioned above, epochs 4, 8, 13 and 14 show conspicuous variability above $5\sigma_{\mathrm{B1}}$ (see Figure III.3(c)). Following the same reasoning as for the A-nucleus, we have also explored the possibility of explaining the flux density variations in the B1-nucleus being due to AGN outbursts. The presence of a LLAGN in the B1-nucleus is well supported by the detection of H_2O megamaser emission (Tarchi et al., 2011, and references therein) and hard X-ray component (e.g., Ballo et al., 2004; González-Martín et al., 2009). Further evidence for a LLAGN in B1 comes from the study of mid-infrared (MIR) high-excitation emission lines (Alonso-Herrero et al., 2009). Hence, one of the five VLBI components reported by Ulvestad (2009) (without considering the one corresponding to the 2005 event) is a candidate for being the LLAGN. Each one of these sources has a flux density $\lesssim 0.3$ mJy at both 8.4 and 2.3 GHz, typical for LLAGN. In the case that one of these sources is the AGN, and even if it were to display the highest inter-year variability that has ever been observed from LLAGN (Nagar et al., 2002), the corresponding burst will have a flux density $\ll 5\sigma_{\mathrm{B1}}$, thus being below our detection limit. Therefore, we find no evidence for any of the detected events to be linked to AGN activity.

We consider next the possibility of explaining the nuclear variability in 1993, 2001 and 2005 (epochs 3–5, 8 and 13–14) as resulting from SN explosions. Note that the scarcity of data available makes it challenging to properly determine the physical parameters that describe the variability we have detected. Nevertheless, we can identify certain properties in each event by examining their rise and fall in the light curve (Figures III.3(a) and III.3(c)). Moreover, if we plot the peak spectral luminosity versus the time after the explosion date to reach the peak (as was done for SN2000ft by Alberdi et al., 2006), we will find that the events considered here, have typical values for moderately luminous type Ib/c and II SNe (see Figure III.4).

A couple of assumptions must be made. First of all, we consider the peak flux density of the events (S_{peak}) as the difference between the flux density at the peak epoch (as seen in Figures III.3(a) and III.3(c)), and the characteristic baseline value of the B1-nucleus (10.08 ± 0.22 mJy), which we consider as the flux density of the nucleus in its quiescent

state. Secondly, we take half the time between the rise and fall in the light curve as the time it takes for each of the putative SNe to reach their peak after the explosion date (t_{peak}). Since each event is poorly sampled we can, as a coarse approach, consider their peak flux densities only as lower limits, and their time to reach the peak as upper limits. We summarize these two assumptions for each putative SN event in Table III.6.

From Table III.6, we see that the peak flux densities of the B1-nucleus corresponding to the 1993 and 2001 events, are above 2.2 mJy. At the distance of Arp 299 these flux densities correspond to luminosities of the order of a few times 10^{27} erg s^{-1} Hz^{-1}, which are typical for type Ib/c or moderately luminous type II SNe, as we can also see in Figure III.4. The 2005 event is more luminous than the others and similar to the most luminous type II RSNe observed, e.g., SN 1986J and SN 1988Z. In the following, we discuss each event separately:

- 1993 event (epochs 3–5). This event exhibits an extremely slow rise and relatively fast fall. Typical RSNe do not display such behaviour. If a single SN is responsible for the increase in flux, it must have reached its peak between epochs 3 and 4 (thus having a flux density peak higher than that of epoch 4). A change of the CSM profile could explain the changing slope in its optically thin phase. In this case, we assume that the putative SN has exploded some time after epoch 2 and has reached its peak some time between epochs 3 and 4, therefore being characterised by $t_{\mathrm{peak}} < 2$ yr and $L_{\mathrm{peak}} > 5.3 \times 10^{27}$ erg s^{-1} Hz^{-1}. These values for L_{peak} and t_{peak} are expected from moderately luminous type Ib/c or type II SNe, as we see in Figure III.4.

- 2001 event (epoch 8). This event is characterised by $t_{\mathrm{peak}} < 1.3$ yr (obtained by taking half of the time between epochs 7 and 9) and $L_{\mathrm{peak}} > 5.7 \times 10^{27}$ erg s^{-1} Hz^{-1}. This corresponds most likely to a type Ib/c or a moderately luminous type II SN (following the same criteria as before).

- 2005 event (epochs 13th–14th). The VLA observations we present here, cover just the beginning of the rise of this event, therefore allowing us to solely estimate lower limits to its peak luminosity and time to reach the peak (see Table III.6). Yet, we can still place this event among the most luminous type II RSNe known to date (see Figure III.4). See §III.3.2.3 for a detailed discussion on the origin of this event.

Unfortunately, Arp 299 was not observed with the VLA at X-band between 1994 and 1999 and we cannot search for new SN explosions in the B1-nucleus during that period. Hence, we divide our analysis in two periods: the first one from February 1990 to May 1994 (hereafter P1), and the second from October 1999 to April 2006 (P2). This is equivalent to one period of 4.2 yr and another one of 6.5 yr.
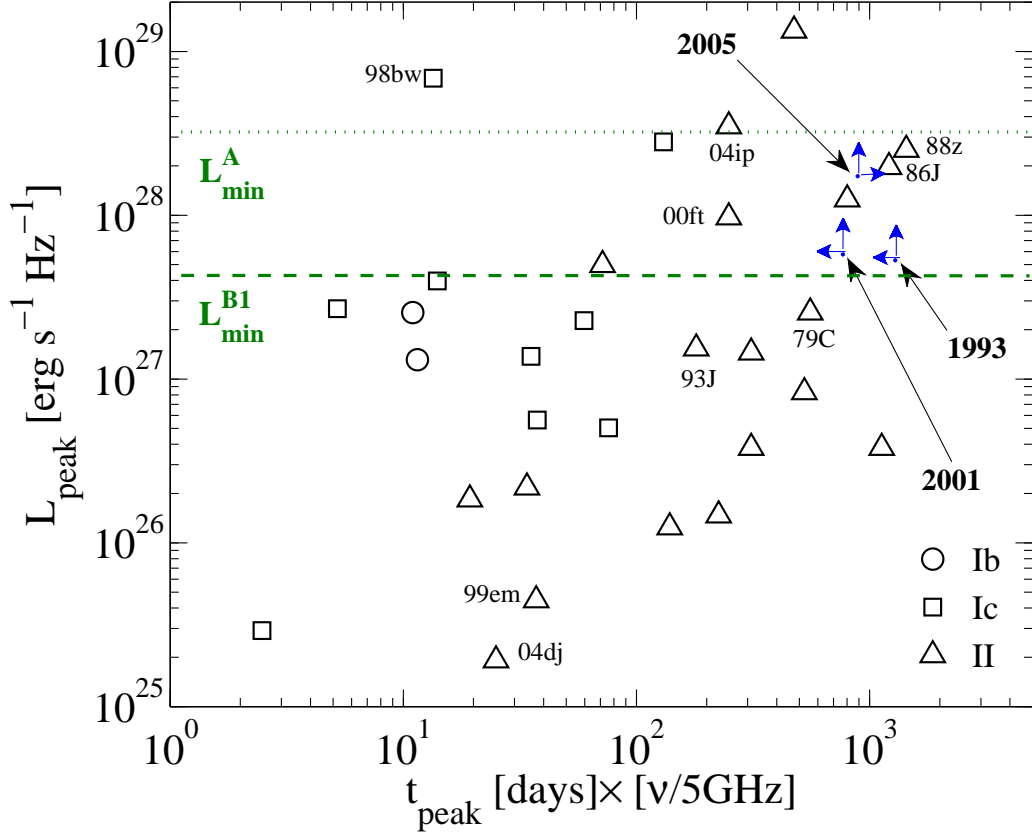
FIGURE III.4: Peak spectral radio luminosity of different types of CCSNe versus the time to reach the peak after the explosion date (updated from Alberdi *et al.*, 2006). We have added a factor of $\nu/(5\,\mathrm{GHz})$ multiplying t_{peak} that allows us to plot L_{peak} at any frequency. Labels for some historic RSNe are added for comparison with our 1993, 2001, and 2005 events (blue dots). Note that the upward arrows on the blue dots refer to L_{peak} lower limit values and leftward arrows are t_{peak} upper limit values for all events, except for 2005 where t_{peak} is a lower limit, which we represent with a rightward arrow. The dotted line represents the minimum luminosity a SN should have to be detected at $5\sigma_{\mathrm{A}}$ in nucleus A through flux density variability. The dashed line represents such detection limit ($5\sigma_{\mathrm{B1}}$) for nucleus B1.

Event 1993 in P1, as well as events 2001 and 2005 (see §III.3.2.3) in P2, can all be explained by RSNe. We note that the RSN type of each event is poorly determined due to the coarse and uneven sampling of the light curve. Only a more frequent sampling could provide the necessary information to characterise each event, as was done for SN 2008iz in M82 Marchili *et al.* (2010). We could solely state that due to the substantial difference in lifetime of type Ib/c and bright type II SNe, our events are likely to be type II SNe rather than type Ib/c. Nevertheless, the mere identification of events to have a CCSN origin allows us to estimate the CCSN rate.

III.3.2.3   The 2005 outburst in Arp 299-B1

We delve now into the nature of event 2005, for which our VLA monitoring has only provided information of its turn-on. For doing this, we make use of additional archival VLA data.

Ulvestad (2009) reported the discovery of a RSN in the innermost nuclear region of the B1-nucleus, from VLBA and Green Bank Telescope (GBT) observations on 17 July 2005, thus likely related with the 2005 event, which has been also detected in the NIR.

Two-point spectral index of nucleus B1 between X- and K-band - The radio fluxes we have estimated for the Arp 299-A and -B1 nuclei, result from the contribution of several compact sources located within the innermost nuclear regions (§III.3.2). The contribution of each compact source can vary in time although most of them show no significant variability in a few month time scale (Ulvestad, 2009).

We want to know what has been the overall change in the nucleus due to the outburst, by studying an observing epoch before, or close to the start of the outburst, and one after. To obtain reliable spectral information, it is important to use contemporaneous observations at different frequencies. Suitable observations in time for our purposes are scarce and we were pushed to use poor resolution observations (see Table III.7). The pre- and post-epochs show simultaneous observations at both X- and K-band. As we did for the light curve measurements in §III.3.2, we restricted the uv-range to allow comparison in the pre- and post-outburst epochs throughout the same baselines. With a common uv-range of 18.9 to 182.9 kλ (structure sizes between ≈ 1 arcsec and ≈ 11 arcsec), all the images were made with a convolving beam of 1.5×1.0 arcsec^2 at $0°$ (in the major axis, the angular size is about the double of what we used in the light curve measurements).

The data reduction and imaging for the spectral indices estimate were made in the same way as explained in §III.3.1, except for the K-band measurements, where the initial

calibration should be done first in phase and then in amplitude and phase to account for phase instabilities introduced by the troposphere.

TABLE III.7: Properties of the VLA images at X and K-bands used for spectral indices estimates. Both early and later epochs were observed under program AW641 and using BnA and CnB configurations respectively. The images were made with a convolving beam of 1.5×1.0 arcsec^2 and a common uv-range which allows the detection of structures with sizes between ≈ 1 arcsec and ≈ 11 arcsec. The two-point spectral indices estimates between X- and K-band for B1- and A-nucleus at the pre- and post-outburst epochs, are shown in the sixth and last columns, respectively. The spectral index α is defined by $S_\nu \propto \nu^\alpha$, where S_ν is the flux density at frequency ν.

Epoch	Date	Band	Weighting	B1-nucleus		A-nucleus	
				S_ν (mJy)	α_K^X	S_ν (mJy)	α_K^X
Pre	2005-02-08	X	natural	11.47 ± 0.58	-0.84 ± 0.08	87.55 ± 4.38	-0.81 ± 0.07
		K		5.05 ± 0.29		39.87 ± 2.00	
Post	2005-06-18	X	uniform	14.84 ± 0.75	-0.06 ± 0.07	87.67 ± 4.38	-0.85 ± 0.07
		K		14.01 ± 0.72		38.19 ± 1.92	

The flux densities of the A-nucleus in Table III.7 are within the errorbars, i.e. from the pre- to the post-outburst epoch, the nucleus A shows a variation of about 0.1% in X-band and $\sim$4.5% in K-band. However, for the B1-nucleus, the variations are significantly higher than that: $\sim$30% in X-band and $\sim$180% in K-band.

As shown in the last column of Table III.7, the spectral index of the A-nucleus has remained practically constant, but this is not the case for the B1-nucleus. Note that the outburst in the B1-nucleus has become relatively stronger at higher frequencies rather than at lower frequencies. This is consistent with an optically thick scenario, e.g., after a SN explosion, where the emission at both bands is partially transparent, especially at K-band. The sixth column in Table III.7 contains the estimated values for the two-point B1 spectral index at the pre- and at the post-outburst epochs (February and June 2005, respectively). We have also obtained the spectral index correspondent to the difference in pre- and post-fluxes, with the aim of unveiling the nature of the source giving rise to the observed outburst. The estimated value for α_K^X(post$-$pre) is 1.00 ± 0.42. Such inverted spectrum is typical of HII regions (e.g., Tarchi *et al.*, 2000) and young radio SNe (e.g., Weiler and Sramek, 1988).

To discriminate between a thermal (HII region) and a non-thermal (RSN) origin, we calculate the brightness temperature (T_B) inferred from the difference in pre- and post-fluxes. This can only be an upper limit, since we are attributing the whole flux difference from the pre- to the post- epoch to the appearance of a single source. We assume a spherical isotropic emitting source of size l (pc), at a distance D (Mpc), for which the

following relation holds

$$\left(\frac{T_B}{K}\right) \lesssim 2.9 \times 10^4 \left(\frac{S_\nu}{mJy}\right) \left(\frac{\nu}{GHz}\right)^{-2} \left(\frac{D}{Mpc}\right)^2 \left(\frac{l}{pc}\right)^{-2} \qquad \text{(III.1)}$$

(see Appendix B).

As we have explained before, the most plausible explanation is that the 2005 event corresponds to a SN. Let us consider a typical expansion velocity of $\approx 10^4$ km s^{-1} which yields a size of $\approx 3.64 \times 10^{-3}$ pc for the free expansion case after 130 days. The inferred T_B when using the difference in flux in X-band ($\Delta S_{\nu=X} = 3.38$ mJy), is $\lesssim (2.1 \pm 0.8) \times 10^{11}$ K, and $\lesssim (7.7 \pm 0.9) \times 10^{10}$ K when using the difference in flux in K-band ($\Delta S_{\nu=K} = 8.96$ mJy). These are very high brightness temperatures, but still below the inverse Compton limit (see Readhead, 1994, and references therein) and not rare for bright SNe short time after explosion (e.g., SNe 1998bw and 2002ap in Bloom *et al.*, 1998; Berger *et al.*, 2002, respectively). Brightness temperatures as high as $\sim 10^8$ have been found for young supernovae in nucleus A, e.g., component A0 (Neff *et al.*, 2004) and A12 (see Pérez-Torres *et al.*, 2009b, and §III.2 in this thesis). Furthermore, the luminosities inferred by $\Delta S_{\nu=X}$ and $\Delta S_{\nu=K}$, $L_{\nu=X} \lesssim (8.1 \pm 3.2) 10^{27}$ erg s^{-1} Hz^{-1} and $L_{\nu=K} \lesssim (2.2 \pm 0.2) 10^{28}$ erg s^{-1} Hz^{-1}, are typical of young, very bright radio supernovae.

We can discard the hypothesis of the thermal emission: in the case of an HII region being responsible for the rise in flux between the pre- and post-outburst epochs, we should either consider the typical size of a young HII region, i.e. an ultra-compact HII region, to calculate the correspondent T_B, or we should consider $T_B \approx 10^4$ K to calculate the correspondent radius of the emitting source. A size of ≈ 0.1 pc (Wood and Churchwell, 1989) implies $T_B \lesssim 10^8$ K at both X- and K-bands, whereas $T_B \approx 10^4$ K implies $l \sim 10$–17 pc. Both values are too large to characterise an ultra-compact HII region and we therefore rule out a thermal origin for our source.

From the evidence we have gathered so far, i.e. spectral index, the large brightness temperature and luminosity, we can safely conclude that the rise in flux in the B1 nucleus was due to the explosion of a radio supernova, as claimed by Ulvestad (2009).

Radio SED of nucleus B1 - We focus now our attention in the post-outburst epoch. C-band measurements are also available in the AW641 observations carried out on 18 June 2005. To add this information to the measurements we have at X and K bands and thus obtain a radio SED of the B1-nucleus, it is necessary to make new images that account for the poorer resolution provided by C-band at CnB configuration (which is considerably worse than that obtained with X or K-bands at BnA configuration). With these considerations, we reduced the C-band data (following the same steps as done before)

and re-imaged the X and K-band observations from 18 June 2005 to match the resolution of the C-band measurement. We have used a common *uv*-range of 18.9 to 103.9 kλ (allowing the detection of structures with sizes between 2 and 11 arcsec), and a convolving beam of 3.5×1.7 arcsec^2 at a position angle of $-60°$. We could have used a smaller *uv*-min, but then our images would have been sensitive to structures as large as ≈ 36 arcsec. Since we are only concerned about the variation in flux within the nuclear regions, we considered appropriated to restrict the *uv*-min even more, thus avoiding the diffuse emission. In Table III.8 we find the fluxes estimated from the images at the different frequencies, and the resulting SED from A- and from the B1-nucleus, are shown in Figure III.5. We see that the SED of the B1-nucleus remains steep at low frequencies, but flattens when going to higher frequencies (due to the emerging new SN), whereas the A-nucleus preserves a steep spectrum at both low and high frequencies.

Obviously, the slopes between the X and K fluxes for the A and B1-nucleus are the same within the errors as those found in Table III.7. The estimated values for the spectral indices between the C and X measurements are $\alpha_{\mathrm{X}}^{\mathrm{C}}(A) = -0.44 \pm 0.13$ and $\alpha_{\mathrm{X}}^{\mathrm{C}}(B1) = -0.61 \pm 0.13$. Note that these values are comparable to those reported by Neff *et al.* (2004): $\alpha_{\mathrm{X}}^{\mathrm{C}}(A) = -0.51 \pm 0.13$ and $\alpha_{\mathrm{X}}^{\mathrm{C}}(B1) = -0.60 \pm 0.13$. This indicates that after the considered post-outburst epoch, the slopes between C- and X-band have not changed significantly, since the new RSN is partially transparent at these two frequencies. This situation agrees with a supernova scenario, in which the supernova emission rises first at higher frequencies and later at lower frequencies (Weiler *et al.*, 2002).

TABLE III.8: Estimated fluxes from the VLA images at C, X and K-bands, used for the radio SED of nuclei B1 and A of Arp 299. The observations correspond to program AW641 at the CnB configuration, carried out on 18 June 2005 (the post-outburst epoch). The images were made with a common *uv*-range of 18.9 to 103.9 kλ (structures with sizes between 2 and 11 arcsec), and a convolving beam of 3.5×1.7 arcsec^2 at $-60°$.

Band	Weighting	S_ν^{B1} (mJy)	S_ν^{A} (mJy)
C	uniform	21.27$\pm$1.08	113.68$\pm$5.68
X	uniform	15.13$\pm$0.76	89.03$\pm$4.45
K	natural	13.90$\pm$0.72	37.52$\pm$1.88
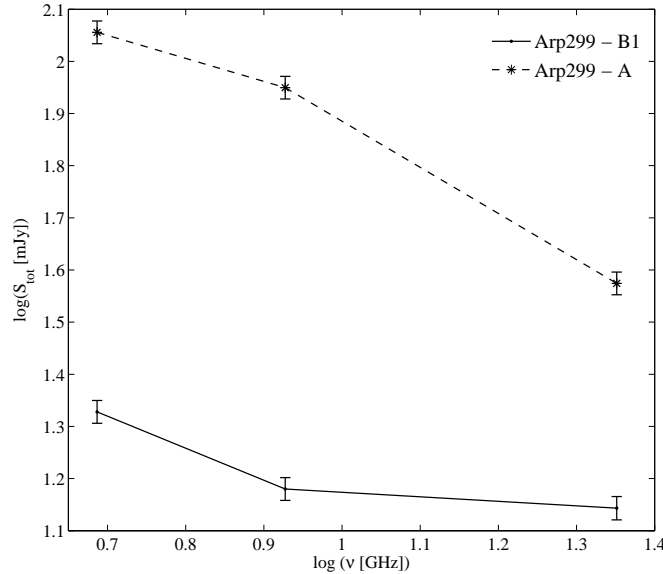
FIGURE III.5: Radio continuum spectra of Arp299-B1 (solid line) and -A (dashed line), from 18 June 2005 VLA observations at C-, X- and K-bands, under program AW641 (see Table III.8).

Nature of the SN responsible of the B1-nucleus 2005 outburst - What type of RSN is responsible of the observed flux density variability? To answer this question we need to make a long-term flux density monitoring with a similar interferometer array. This is a complicated task due to the scarcity of observations after the outburst. However, we know that VLA D-configuration observations at K-band carried out in 9 April 2007 (more than two years after the outburst), yield an approximate flux for the B1-nucleus of 15 mJy (Tarchi, A. 2010, private communication). This value might be affected by diffuse emission in the beam. However, even if the contribution of the diffuse emission is as large as the 50% of the observed flux, we would have that still, after almost two years, the flux at K-band for the B1-nucleus (~ 7.5 mJy) is higher than the value we obtained at our pre-outburst epoch (see Table III.7). This would indicate a type II origin for the RSN in nucleus B1. This conclusion is also supported by the high brightness temperature and luminosity we have found in §III.3.2.3, values which are similar to those found in e.g., SN 1988Z (see e.g., van Dyk *et al.*, 1993) which is a type IIn supernova having an optically thick spectral index similar to the one we found for the young RSN in nucleus B1.

III.3.3 The CCSN rate in nucleus B1

We now want to obtain an estimate for the ν_{SN} over the ~ 11 yr (P1+P2) comprised in our study. In order to do this, we assume that the N SN events detected in B1 are

independent and occur at a constant rate over time, thus obeying Poisson statistics. The probability of observing N events is

$$\mathrm{Prob}(N) = \frac{\mu^N}{N!} e^{-\mu},$$

where $\mu = \nu_{\mathrm{SN}} t$ is the mean of the Poissonian distribution (which in this case is simply estimated by the number N of detected SNe). Since the number of detections is very small, the upper and lower Poisson 1σ uncertainties are adopted from Gehrels (1986).

In the case of P1, with one RSN (1993 event), we have $\nu_{\mathrm{SN}=1}^{\mathrm{P1}} \approx 0.24_{-0.20}^{+0.55}\,\mathrm{yr}^{-1}$. For P2, where there are two detections (2001 and 2005 events), we have $\nu_{\mathrm{SN}=2}^{\mathrm{P2}} \approx 0.31_{-0.20}^{+0.41}\,\mathrm{yr}^{-1}$. We then calculate a total ν_{SN} for the 10.7 yr ($\sim$11 yr) comprised in our study using the upper and lower Poisson 1σ uncertainties for three events, which yields a final $\nu_{\mathrm{SN}=3} \approx 0.28_{-0.15}^{+0.27}\,\mathrm{yr}^{-1}$.

Our variability test leads us to a ν_{SN} estimate which, within the uncertainties, agrees with the IR luminosity based SN rate estimate, as well as with previous radio-based estimates (see Table III.2).

It is worth to mention that the radio-based estimates by Alonso-Herrero et al. (2000) and by Neff et al. (2004) in Table III.2) rely on the use of formulae which relate the SN rate with the source spectral index and flux density values. In the case of the estimates by Alonso-Herrero et al. (2000), these values were retrieved from previously published observations made in 1980 and in 1990. In our study, we have seen that the B1-nucleus shows conspicuous variations in its flux-density, and non-reliable spectral index determinations could be obtained comparing data at different epochs. For example, different spectral indices are to be expected between a given measurement at 4.8 GHz, for instance, and the value at 8.46 GHz from epochs 1 and 4; as a consequence, we would also obtain different SN rates. Even when obtaining spectral indices based on flux density measurements from contemporaneous observations at different frequencies, there is still an uncertainty related with a possible evolution in time of the spectral index, since new sources (e.g. SNe) become visible first at high frequencies, and later at low frequencies due to absorption effects (see e.g., Weiler et al., 2002, and Chapter V of this thesis). Another issue is the possible flattening at low frequencies caused by free-free absorption, as mentioned by Alonso-Herrero et al. (2000). Hence, the assumption of a straight spectral index between 408 MHz and 8.4 GHz made by Neff et al. (2004) for calculating SN rates, would not be appropriate, and it would represent a relevant source of uncertainty in their estimates, making them unreliable.

Our CCSN rate estimate, on the other hand, represents a lower (but stringent) limit due to our detection threshold. Event 1993 is only slightly above such limit, and we see from

Figure III.4 that fainter (as well as more rapidly evolving) SNe than the one responsible for the 1993 event, are deemed to remain as non-detections through this variability test. We probably miss most type Ib/c and all type IIP SNe, which represent about 37% and 48% (Smith *et al.*, 2011), respectively, of all CCSNe in a volume-limited sample (see Figure III.4). Thus, the total ν_{SN} should be significantly higher than our estimate and those based on IR luminosity (since these two are comparable), unless the IMF is a top-heavy one favouring the production of the most massive stars, and the surrounding environment is dense enough, so that a large fraction of the SN explosions will turn into bright radio sources. For instance, Chevalier and Fransson (2001) have shown that the high molecular cloud densities in the nuclear regions of galaxies undergoing bursts of SF (e.g., M82), can account for the high radio luminosity of the supernova remnants therein. This is also the case for the luminous RSNe in Arp 220, which Parra *et al.* (2007) have found to be consistent with powerful type IIn SNe interacting with their dense CSM found by Lonsdale *et al.* (2006), which implies a SFR high enough to power the entire L_{IR} of the galaxy. Therefore, if the gas surrounding the SNe in Arp 299-B1 is very dense, our ν_{SN} estimate could be close to the true CCSN rate. This result is not surprising if we consider that already from the EVN observations of the A-nucleus, Pérez-Torres *et al.* (2009b) found that its ν_{SN} might be much higher than previous estimates, thus suggesting that a top-heavy IMF could describe better the observations of the nuclear starburst in Arp 299-A. We might well be facing the same situation here for the B1-nucleus. In fact, a recent study of the properties of the sample of optical/NIR detected SNe in the circumnuclear regions of Arp 299, also indicates an IMF possibly biassed toward high mass stars in the system (Anderson *et al.*, 2011).

However, the population of SNe within the innermost $\sim 200\,\mathrm{pc}$ of the nuclei of Arp 299 can be quite different from the one within ~ 1–$4\,\mathrm{kpc}$ distances from the nuclei of Arp 299 that Anderson *et al.* have studied, due to the difference in the ambient conditions, which could lead to different IMFs (see e.g. Chevalier and Fransson, 2001). Therefore, in the future, the combined use of high spatial resolution radio and NIR observations to detect and study the population of SNe within the LIRG innermost nuclear regions, is crucial in order to better constrain their SF properties.

III.3.4 Caveats and limitations of our variability test

We have presented a variability test that covers a period of $\sim 11\,\mathrm{yr}$ (P1 + P2), with 14 data points. This corresponds to a typical sampling rate of 1.3 observations per year, and a typical time interval between observations of ≈ 11 months (considering P1 and P2 separately), although we acknowledge that the sampling is very uneven.

The typical time interval between observations in our study makes the detection of type Ib/c SNe difficult, as they decay fast at radio wavelengths, having short lifetimes that range from a few days up to a few months (see e.g., Weiler *et al.*, 2002). It is thus impossible to resolve individual type Ib/c SNe occurring within an 11 months period. However, it is not impossible to detect them, if we are fortunate enough to have an observation at around the time of their luminosity peak. This is of course not very likely and our detection threshold (see Figure III.4) makes our test blind to practically all type Ib/c SNe (as we have discussed in §III.3.3), for the given sample.

For type II SNe the situation is different. Although a coarse and uneven sampling does not allow an unambiguous identification of the SN subtype (IIP, IIL, IIb, IIn), both the sensitivity and the frequency of our sampling favour the detection of bright and long-lasting events. For instance, SN 2000ft in a LIRG host galaxy (NGC 7469) at 70 Mpc distance, with a peak luminosity of almost 1×10^{28} erg s^{-1} Hz^{-1}, was clearly visible in VLA observations over a period of 4 yr (Pérez-Torres *et al.*, 2009a). Furthermore, an event like SN 2000ft, could be covered by four of our observations (with a typical separation of ~ 11 months). In fact, we would need at least three observations covering the light curve, for a minimum sampling. This is fulfilled in the case of the B1-nucleus for long-lasting events. However, in the case of nucleus A, the identification of RSNe is more challenging than in the case of B1 due to our current sampling characteristics, in addition to the sensitivity threshold which allows only the detection of very bright events. According to IR luminosity based estimates, the SN rate of nucleus A (~ 0.7 yr^{-1}) is about twice that of B1. A sampling rate of 1.3 observations per year is clearly not optimal to probe the RSNe activity in nucleus A, for which we could often have overlapping events, with severe difficulties to separate them.

III.4 Searching for NIR counterparts of radio supernovae in Arp 299-A

NIR observations towards the A-nucleus were carried out with the Gemini-North Telescope in the K-band (2.2 μm) under the program "Altair Study of Supernovae in Luminous Infrared Galaxies" (P.I.: S. Ryder).

In the previous section we have estimated the radio SN rate for the B1-nucleus and pointed out that SN detections in the A-nucleus—unless extremely radio luminous SNe, like SN 1998bw—are feasible only by means of VLBI observations, at radio wavelengths, or by NIR observations with high angular resolution. We then consider the EVN observations carried out in April and December 2008 by Pérez-Torres *et al.* (2009b), revealing young

TABLE III.9: Log of the Gemini-North NIR observations of A-nucleus.

UT date	Program	Exposure Time (s)
2008 Jun 20.3	GN-2008A-Q-38	8×30
2010 May 04.8	GN-2010A-Q-40	8×30

TABLE III.10: Sources of uncertainty in the A-nucleus Gemini-N image WCS.

Transformation	RMS (arcsec)
WCS of SDSS	0.090
SDSS to *HST*	0.056
HST to Gemini-N	0.023
Combined uncertainty	0.1085

RSN candidates within the nucleus A. Aiming at finding the NIR counterparts for these objects, we analysed our contemporaneous (June 2008) NIR AO Gemini-N observations.

We used the NIRI with the ALTAIR Laser Guide Star AO system (0.022 arcsec/pixel, FWHM∼0.1 arcsec) for the two observations (see Table III.9) in this study. The obtained images were reduced using the NIRI package within the Image Reduction and Analysis Facility (IRAF) V2.14. Before median combining the target images, we subtracted the inherent horizontal noise pattern of the NIRI images.

The world coordinate system (WCS) for the NIRI images with a small FOV (23 × 23 arcsec^2) was obtained in an iterative way. We first calibrated the WCS of an SDSS *i*-band image using 28 point-like sources from the Two Micron All Sky Survey (2MASS) catalogue. Having a total of 51 2MASS sources in the SDSS field, we rejected 23 which were either elongated, too faint, too close to another object to be blended, and/or located on corrupted pixels regions of the images.

The SDSS *i*-band image was then transformed to an *HST* Advanced Camera for Surveys (ACS) *J*-band image (obtained as already calibrated from the *HST* science archive) using nine common sources between the two images. As a final step, we transformed the *HST* image to the images of the A-nucleus obtained with the Gemini-N telescope. For doing this, we used 20 sources. In all the steps we used a simple geometric transformation for the coordinates, which included shifts in x and y as well as the same scaling factors and rotation in x and y. The propagation of uncertainties between the different alignment steps yielded a total RMS of approximately 0.1 arcsec (see Table III.10).

The centroid position (J2000) of nucleus A as measured in the WCS calibrated Gemini-N image using IRAF is $11^{h}28^{m}33^{s}.62$, $58°33'46''.6$ (see deep image in Figure III.6(a)). The distance between the NIR A-nucleus and its radio counterpart (see Table III.1) is 0.103 arcsec, so that both positions are coincident within 1σ.
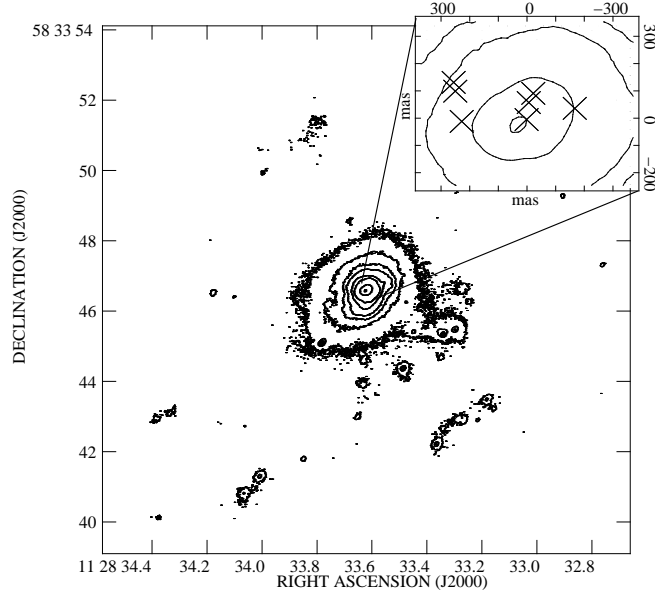
(a)
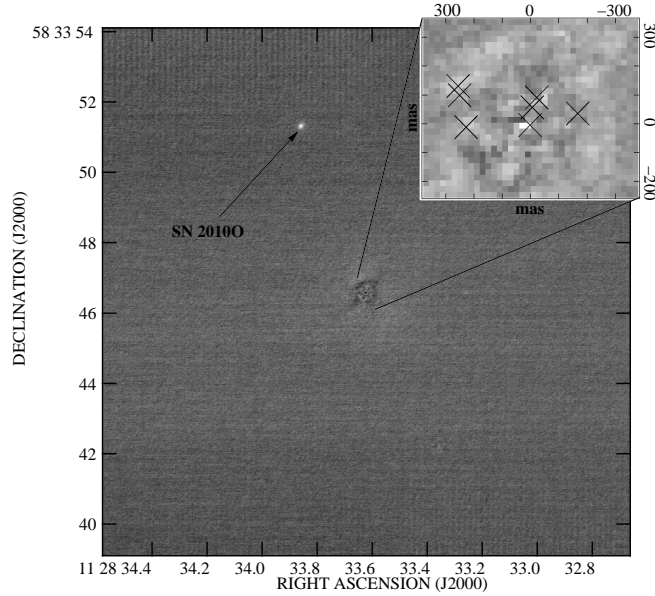
(b)

FIGURE III.6:   Arp 299-A WCS calibrated Gemini-N *K*-band images (FOV= 15×15 arcsec^2). (a) Our reference image (June 2008), which we use to compare with contemporaneous VLBI images. A blow-up of the inner nuclear region is also shown. The 'x' symbols indicate the positions of the EVN detected SNe by Pérez-Torres *et al.* (2009b). (b) A subtraction of our Gemini-N image obtained in May 2010 from the June 2008 epoch (shown as negative). Note that the use of the innermost part of the A-nucleus is needed for the PSF matching to obtain a smooth subtraction. However, because of this, we lose information about any possible SN within a radius of ~ 70 pc (~ 300 mas) from the centre of the A-nucleus. SNe occurring outside the ~ 300 mas radius, are detectable by our method with a limiting magnitude of ~ 18.5, and outside 1 arcsec radius, to a limiting magnitude of ~ 20. Note that SN 2010O, discovered in January 2010 in the circumnuclear regions, is still well detected in the subtracted image.

III.4.1 SN detection in NIR images

We have used a difference imaging technique based on the Optimal Image Subtraction (OIS) code (Alard and Lupton, 1998), and already demonstrated to work in SN detection in NIR AO images of LIRGs (Mattila *et al.*, 2007). Having transformed the image from the epoch of interest (2008 June 20) to our reference image from 2010 May 4, we then selected 19 regions around suitable bright objects for deriving a convolution kernel that was later used to match the PSF of our reference image to the PSF of the other image before performing the image subtraction. To obtain a successful subtraction, we had to include also the nucleus itself in these regions, given its outstanding brightness compared to the other objects in the image.

The FWHM of the A-nucleus is about 0.4 arcsec in our Gemini-N images. To obtain a satisfactory subtraction result, we used $\sim 0.66 \times 0.66\,\mathrm{arcsec}^2$ for the size of the regions involved in the kernel solution. This is large enough to cover well the diffraction limited core of the PSF (whereas the much wider PSF wings are hidden in the noise for most of the sources present in our images). Regions substantially smaller than this did not result in a smooth subtraction for the regions around the bright nucleus. As a result of this, the detection of SNe falling within the innermost $\sim 300\,\mathrm{mas}$ radius region is not feasible using these techniques (see Figure III.6(b)).

EVN radio images by Pérez-Torres *et al.* (2009b) have approximately 10 times better resolution than that of our NIR AO observations. Thus, the resolution of these NIR observations is not high enough, such that we could expect to be able to detect objects as deep in the LIRG nucleus as in the EVN observations. In addition, SN detections in the NIR domain might also be hindered by the high extinction towards the SNe. However, not all the CCSNe produce radio emission strong enough to be detectable at the distance of the nearest LIRGs. Hence, we have investigated the limiting magnitude for our NIR SN detection ability at different distances from the centre of the nucleus A.

III.4.2 SN detection threshold in the A-nucleus

We have simulated SNe of different magnitudes at different distances from the centre of the nucleus A in our 2008 June 20 image using the IRAF MKOBJECTS task. Unfortunately, there are no bright field stars in our Gemini-N images (FOV$\approx 23 \times 23\,\mathrm{arcsec}^2$) that can be used to model the complicated PSF. Therefore, for the fake SNe a Moffat profile with a beta parameter of 2.5 and FWHM of $\sim 0.15\,\mathrm{arcsec}$ was used. We found this to give a reasonable match with the diffraction limited part of the PSF whereas for the faint sources the much wider PSF wings disappear within the noise.

After the matching and subtraction of the reference image for each simulation, we checked if the simulated source could be detected significantly (more than 3σ) above the subtraction residuals within the nuclear regions. The level of the noise introduced by the subtraction residuals was determined as the standard deviation of the aperture sums (using a small radius of 0.13 arcsec) for 49 apertures placed in a grid covering the innermost 0.66×0.66 arcsec^2 nuclear region. We obtained a photometric calibration for our Gemini-N images, with too small a FOV to include any 2MASS stars, making use of the *HST* photometry for several compact circumnuclear SSCs (A1–A6) reported by Alonso-Herrero *et al.* (2000) and converted to the standard K-band. We estimated our SN detection threshold by simulating (one at a time) and recovering eight artificial SNe of a given magnitude, distributed at different locations, at a 300 mas distance from the centre of the nucleus A (or ~ 70 pc projected distance). By repeating the simulation for a range of magnitudes, we found a 3σ limiting magnitude of ~ 18.5 (estimating our calibration to be accurate to ± 0.1 mag) for our SN detection. Inside this radius our method was not sensitive for the detection of highly obscured SNe. Note that the limiting magnitude we have found is similar to the magnitude of SN 2004ip discovered in IRAS 18293−3413 (Mattila *et al.*, 2007) with the NAOS-CONICA (NaCo) camera on the Very Large Telescope (VLT).

We tested our SN detection ability also in the circumnuclear regions where no strong image subtraction residuals are present. For this the level of noise was first determined as the standard deviation of aperture fluxes for 45 apertures (0.13 arcsec radius, 0.20–0.26 arcsec sky annulus) placed along a circumference at 1 arcsec distance from the centre of the nucleus A. Again, by simulating and recovering 12 artificial SNe of a given magnitude distributed at different locations along the same circumference, we found a 3σ limiting magnitude of ~ 20.

From the template light curves for ordinary CCSNe provided by Mattila and Meikle 2001, we adopt $M(K)_{\mathrm{peak}} = -18.6$ and a decline rate of $\Delta m(K) = 0.022$ mag/day after the peak. At the distance of Arp 299, this corresponds to $m(K) = 14.7$ at maximum light. We would therefore be able to detect such a SN suffering from a visual extinction of up to $A_V \sim 15$ (similar to the extinction found in our study for SN 2008cs in the circumnuclear regions of a LIRG) at 300 mas from the centre of nucleus A, still at three months from the maximum light. In the case of a slowly declining (SNe 1979C and 1998S-like) SN, for which $M(K)_{\mathrm{peak}} = -20.0$, the apparent magnitude at the distance of Arp 299 becomes $m(K) = 13.3$ at maximum light. Thus, the visual extinction towards such a SN could be as high as about 30 magnitudes and still detectable at 300 mas from the centre of the nucleus A, three months after the maximum. At a larger distance (1 arcsec or ~ 200 pc projected distance) from the centre of the nucleus, our observations were sensitive to an ordinary CCSN with $A_V \sim 30$, or slowly declining CCSN with A_V over 40.

At radio frequencies there is no dust extinction, and a SN will appear bright when the interaction between the SN ejecta and the CSM is strong enough, i.e., when the CSM is dense enough. However, at NIR wavelengths, all types of SN events should be visible as long as the visual extinction is not too high. Therefore, SNe in the less extinguished circumnuclear regions could be more easily detected at NIR wavelengths than at radio frequencies, while the opposite is true when dealing with objects within the innermost nuclear regions.

CHAPTER IV

PROBING WATER MASER EMISSION IN LIRGS

The high concentration of dense molecular gas and dust in the circumnuclear regions of (U)LIRGs ensures a wealth of molecular chemistry. For each molecular or atomic transition to be excited, a certain temperature and density (of either particles or radiation) are needed. For example, the H_2O line at $22\,\mathrm{GHz}$ traces warm ($T_{\mathrm{kin}} \gtrsim 400\,\mathrm{K}$) and dense ($n_{H_2} \gtrsim 10^7\,\mathrm{cm}^{-3}$) molecular gas (see e.g., Elitzur, 1992). These are typical values for the dense and energetic circumnuclear regions of (U)LIRGs; thus, we can expect transitions such as the $6_{16} - 5_{23}$ of H_2O to occur.

By studying the different components of the maser emission, it is possible to probe the kinematics and dynamical structures of the gas in which masers are embedded. Furthermore, because water masers appear close to their powering sources, they represent the only means to image the regions and probe structures such as accretion disks around the central black hole, jet-cloud interactions or nuclear outflows, in highly obscured environments such as the inner parsec-scale regions of (U)LIRGs.

The first extragalactic water maser was found in 1976 (Churchwell *et al.*, 1977). Since then, approximately 80 extragalactic masers have been detected[1]. Luminous extragalactic water masers ($L_{H_2O} > 10\,\mathrm{L}_\odot$) are associated with the presence of an AGN, whereas those being low-luminous ($L_{H_2O} < 10\,\mathrm{L}_\odot$) appear to be associated in most cases with SF activity, and in some cases, they have been found to be associated with the presence of a LLAGN (see e.g., Tarchi *et al.*, 2011). Luminous extragalactic water masers have been found to trace either accretion disks (e.g. NGC 4258; Miyoshi *et al.*, 1995), radio jets (e.g. NGC 1068; Gallimore *et al.*, 2001) or nuclear outflows (e.g., in the Circinus galaxy; Greenhill *et al.*, 2003). Furthermore, among AGNs, the highest water maser detection rates have been found in Seyfert 2 and low-ionisation narrow emission-line region (LINER) galaxies (see Lo, 2005; Greenhill, 2007, for a review on extragalactic water masers). Water maser emission has also been detected in a number of (U)LIRGs which appear to host an AGN, e.g., NGC 6240 in Hagiwara *et al.* (2002), NGC 23 and NGC 7479 in Braatz and Gugliucci

---

[1]For a list, see `https://www.cfa.harvard.edu/~lincoln/demo/HoME/surveys/survey.html`

(2008).

IV.1 Shedding light on the AGNs of Arp 299

We proposed EVN observations of water maser emission towards the merging system Arp 299, aiming at investigating the presence of AGNs, and their role as an energy source in the system, whilst gaining insight into the interaction of the AGN with the surrounding dense, warm molecular gas, further advancing our understanding of the starburst-AGN connection.

This is an ongoing project originally lead by two different groups (Romero-Cañizales, Pérez-Torres, Alberdi, Rodríguez, Aalto, Kurtz & Polatidis / Tarchi, Castangia & Sanna) under projects ER025 and ET011, which were later merged.

IV.1.1 The case of Arp 299-A

Arp 299-A has been extensively studied at different wavelengths to investigate its power engine. Both observations and models point to a very powerful starburst in the nucleus (e.g., Aalto *et al.*, 1997; Smith *et al.*, 1998a; Polatidis and Aalto, 2001; Neff *et al.*, 2004; Imanishi and Nakanishi, 2006; Alonso-Herrero *et al.*, 2009; Pérez-Torres *et al.*, 2009b). In fact, there has been no need of invoking an AGN to explain its infrared luminosity. Despite the inferred morphology for Arp 299-A from CO observations (Aalto *et al.*, 1997), OH megamaser emission and HI absorption (Baan and Haschick, 1990; Polatidis and Aalto, 2001), being more consistent with the presence of a rotating disk-like structure powered by SNRs, X-ray studies by Ballo *et al.* (2004), have found that the strength of the 6.7 keV Fe-K_α line in the spectrum of Arp 299-A, is likely indicating the presence of an AGN.

In EVN observations from 2008 towards Arp 299-A, we detected a rich cluster of 26 compact radio emitting sources in the central 150 pc of the nuclear starburst (see Figure III.2 in Chapter III of this thesis, and Pérez-Torres *et al.*, 2009b). In more recent EVN observations at 1.7 and 5 GHz we have found one source that has a very flat spectral index ($\alpha = -0.05$) and shows, along with neighbouring compact sources, a core-jet structure at 1.7 GHz (see Figure IV.1), thus representing the long sought AGN in the A nucleus (Pérez-Torres *et al.*, 2010). Arp 299 is then one of the few merging systems where a double AGN (one in each of the nuclei of the interacting galaxies) has been found (NGC 6240 and Mrk 463 in Komossa *et al.*, 2003; Bianchi *et al.*, 2008, respectively). It is then interesting to investigate why the AGN has not played an important role so far in the energetics of the merger.
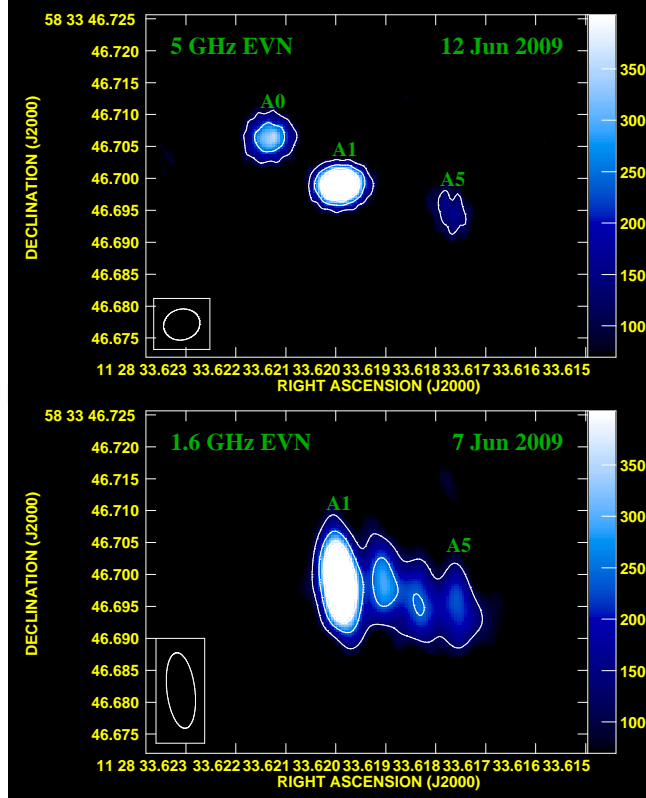
FIGURE IV.1: EVN 5 GHz (upper panel) and 1.7 GHz observations (lower panel) of Arp 299-A (Pérez-Torres *et al.*, 2010). The FOV in both images is similar, and the labels on the components correspond with the nomenclature in Pérez-Torres *et al.* (2009b). Components A1–A5 show a core-jet structure at 1.7 GHz, typical of an AGN. Moreover, the two-point spectral index derived from these observations for component A1, is also consistent with A1 being the core of the core-jet structure suggested by the 1.7 GHz continuum emission. Component A0 is only detected at 5 GHz due to the presence of a foreground absorber that hinders its emission at 1.6 GHz (Pérez-Torres *et al.*, 2010).

In 2002, water maser emission was detected towards Arp 299-A by Henkel *et al.* (2005) using the Effelsberg telescope. The detected maser feature shows a broad profile ($\sim$ 200 km s^{-1}) and has a flux density peak of about 25 mJy/beam. Tarchi *et al.* (2011) report VLA observations of the 22 GHz water maser emission towards Arp 299 (see Figure IV.2) carried out in 2004 and in 2007. They report a maser spot in the inner region of Arp 299-A with an isotropic luminosity of 28 L$_\odot$ and conclude that the water maser emission found in Arp 299-A is associated with an expanding structure, close by, and in front of the nuclear region of the galaxy. In addition, the water maser emission is blueshifted with respect to the systemic velocity ($\sim$ 3100 km s^{-1} from CO observations by Casoli *et al.*, 1999), and similar to the OH and HI distributions (Baan and Haschick, 1990; Polatidis and Aalto, 2001), so that it could be part of an outflow. It is also very interesting that the strong water maser emission has been spatially coexisting in Arp 299-A with powerful OH masers, given that, so far, luminous masers from these two molecular species seem to be mutually

exclusive (Greenhill, 2007; Tarchi *et al.*, 2011).

IV.1.2   The case of Arp 299-B1

Only five VLBI components have been detected in Arp 299-B1 (Ulvestad, 2009). This is consistent with its FIR luminosity and its associated SN rate of $\nu_{\mathrm{SN=3}} \approx 0.28^{+0.27}_{-0.15}\,\mathrm{yr}^{-1}$ (see §III.3.3). On the other hand, the presence of an AGN in Arp 299-B1 is well supported by the detection of H_2O megamaser emission (Henkel *et al.*, 2005; Tarchi *et al.*, 2011, see also Figure IV.2), hard X-ray component (e.g., Ballo *et al.*, 2004; González-Martín *et al.*, 2009), etc. Revisited observations of the water megamaser towards this region will help us to pinpoint its driving source, now that data on VLBI sources are available (Pérez-Torres *et al.*, 2009b, 2010). Furthermore, we will have an overall view of the role of AGNs in the Arp 299 merging system.
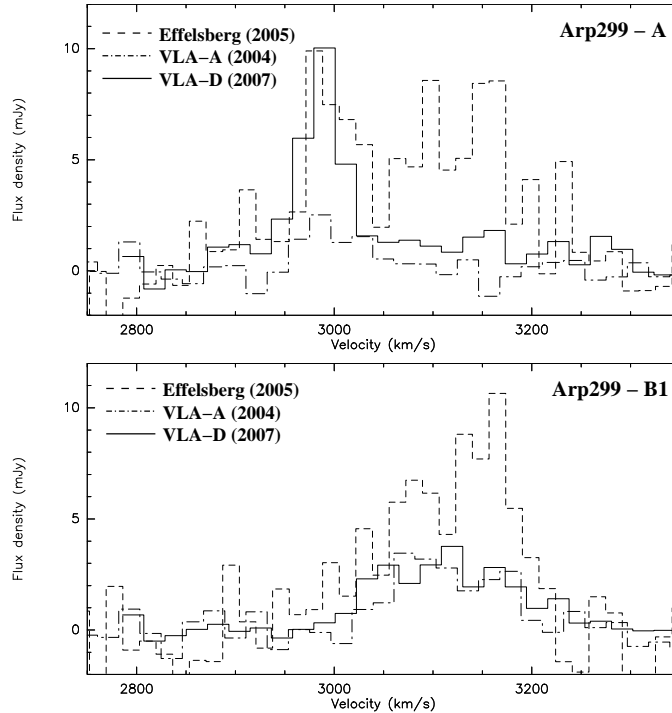
FIGURE IV.2: Water Maser profiles taken from Tarchi *et al.* 2007 for Arp 299-A (upper panel) and Arp 299-B1 (lower panel). Dashed lines correspond to Effelsberg telescope observations (November 2005), dash-dotted lines correspond to VLA observations in A-configuration (September 2004) and solid lines correspond to VLA observations in D-configuration (September 2007). Note that the large brightness inferred from the interferometric observations (from 8 to 28 $L_\odot$ in the case of nucleus-A, and $\sim 20\ L_\odot$ in the case of nucleus-B1) are likely indicating that the masers are associated with an AGN. In this case, we would not expect to resolve the maser emission while observing them at higher resolution (as with VLBI), and so the difference between the observations carried our in D- and in A-configuration with the VLA is considered as real.

IV.1.3   Experiment ER025: observational setup

In October 2010, we carried out EVN observations of the $6_{16} - 5_{23}$ H_2O transition towards the Arp 299 system, aimed at i) detecting for the first time the water maser emission in Arp 299 at VLBI scales, ii) pinpointing the emitting regions with milli-arcsecond angular resolution, iii) determining the distance of the masing regions from each nucleus with great accuracy, hence probing their potential spatial coincidence, iv) possibly unveiling the nature of the maser emission as a disk or a jet maser.

ER025 consisted of phase referencing full EVN observations in two tracks of 12 hr each, to have individual pointings on nucleus A and B1. The segments were labelled as ER025A (for nucleus A) and ER025B (for nucleus B1). A single observing run with correlations at each nucleus could go in detriment of the sensitivity, since the separation between A and B1 is ≈ 21 arcsec (quite large compared to the VLBI beam). Because of the weakness (a few mJy) of the maser line and of the nuclei themselves, we relied on phase-referencing for this project. As a phase-reference calibrator, we used J1128+5925, found at 0.9° projected distance from Arp 299, and with a peak flux density of 230 mJy/beam at 1.3 cm. The FOV is limited to ~ 2.4 arcsec by time-smearing, which at a distance of 44.8 Mpc, corresponds to ~ 500 pc (enough to cover the nuclear and circumnuclear regions of both Arp 299-A and -B1).

The following stations (locations, diameter) participated in the observations: Ef-Effelsberg (Germany, 100 m), Mc-Medicina (Italy, 32 m), On-Onsala (Sweden, 20 m), Jb2-MK II (UK, 25 m), Mh-Metsähovi (Finland, 14 m), Ys-Yebes (Spain, 40 m) and Ro70-Robledo (Spain, 70 m). Within each track, 360 min were spent on-source. We used four subbands (each with dual polarization, 256 channels and 16 MHz of bandwidth) and 1 s integration time, which resulted in a total recording rate of 512 Mbits/s at 2 bit sampling. To avoid loosing spectral information due to the roll off at the edges of each subband, we overlapped the subbands by 4 MHz. Hence, the total velocity coverage is approximately 730 km s^{-1}, allowing to cover the maser features close to the systemic velocity.

The use of 256 channels allows to better isolate RFIs, as long as these occur only at specific frequencies with no variations in time (unlike the case shown in Figure II.3). To increase the sensitivity, it is possible to average in frequency once RFI features have been removed. For instance, averaging by a factor of four allows to obtain a spectral resolution ~ 3.5 km s^{-1} (or 0.25 MHz) and a spectral channel rms ≈ 0.5 mJy/beam, enough to get 7σ detections of the putative maser components even if they are as faint as 3.5 mJy (the minimum peak for the water maser line; see Figure IV.2). We note that the addition of Robledo 70 m is crucial, since the expected rms goes down by a factor of 2/3 by including this antenna.

IV.1.4 Experiment ER025: the observations

The data reduction for the water maser projects has proved to be very challenging. In the following, I provide some details for each segment of our project:

(1) ER025A: The target of this segment was Arp299-A. Seven antennas took part in the observations but many problems arose during observations. MK II was heavily affected by RFI and had amplitude problems in RCP; Metsähovi provided very few usable data, apparently due to failures of the baseband converters; and Robledo had in situ amplitude calibration problems and operated under bad weather (rain) during the observations, factors which severely affected its sensitivity. This situation basically left us with four antennas. In addition, Effelsberg was lost for about 3 hr due to slow slewing between target and calibrator close to zenith. As a consequence, fringe fitting did not work properly, and we obtained very large delays and rates, preventing us from producing any map at all for the A-nucleus.

(2) ER025B: The target of this segment was Arp299-B1. For this experiment we also had seven antennas. MK II and Metsähovi had practically the same problems as for ER025A, with the exception of the first subband in MK II which had somewhat acceptable data. Robledo had this time a more reliable amplitude. Although we still suffered from heavy data loss, it was possible to obtain a good fringe calibration. Unfortunately, the large fraction of data that needed to be flagged resulted in a final rms about four times larger than the nominal one we proposed for, i.e., approximately 2 mJy/channel. The resulting maps do not provide evidence for neither continuum nor spectral confident detections/features. No continuum sources were detected. In Figure IV.3 we show the attained profile of the B1-nucleus water maser emission.

The non-detection of water maser emission in Arp 299-B1 can be explained by the masers being heavily resolved, or variable (having a peak below 2 mJy at the time of the observations). In the case of Arp 299-A, the observations were severely affected by technical problems and we were not able to obtain any spectrum. In June 2011, we thus submitted a proposal to re-observe the segment A of ER025.

Taking advantage of the experience we gained in our past experiment, we slightly modified our observing request. We proposed full EVN observations 450 min on-source time, in a 15 hr run. In addition to the antennas used in ER025, we also requested the use of stations Sv-Svetloe (Russia, 32 m) and Zc-Zelenchukskaya (Russia, 32 m), which will improve the signal-to-noise ratio. The observations, now under project ER028, were approved by the EVN Programme Committee and will probably be scheduled within the first semester of 2012.
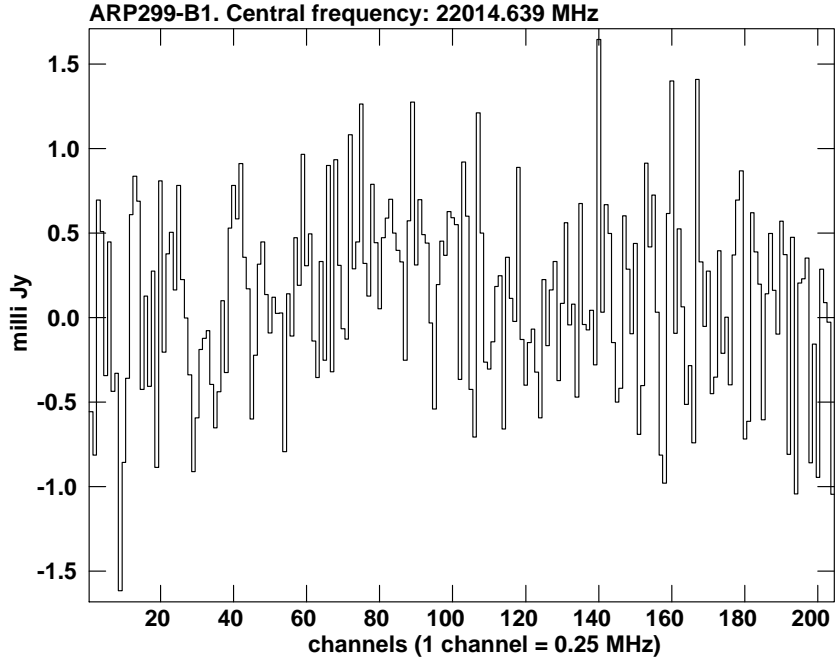
FIGURE IV.3: Water Maser profile of Arp 299-B1 (experiment ER0025B).

IV.2 The search for water maser emission in NGC 7469

NGC 7469 is a LIRG, $\log(L_{\mathrm{IR}}/\mathrm{L}_\odot) = 11.6$, located at a distance of 65 Mpc (Sanders *et al.*, 2003). This galaxy displays a barred spiral structure containing a luminous Seyfert 1 nucleus, surrounded by a dusty starburst of about 1 kpc in size (Wilson *et al.*, 1991). There is evidence for a 10^7 M$_\odot$ black hole through reverberation mapping (Lonsdale *et al.*, 2003). EVN observations by Alberdi *et al.*, (in preparation), have revealed the presence of a source, which is consistent with an AGN, in coexistence with ongoing SF activity within the innermost ≈ 50 pc of the nuclear region.

No water vapour masers have been detected in face-on, Seyfert 1 galaxies, whilst there is a high detection toward type 2 Seyferts (Braatz *et al.*, 1997). It has been recently argued that the low detection towards type 1 Seyferts, is likely a matter of sensitivity (Ramolla *et al.*, 2011) against higher degree of obscuration.

In October 1993, Braatz *et al.* (1996) made 22 GHz observations with the Effelsberg 100 m telescope towards nearby active galaxies. No water maser emission was detected towards NGC 7469. Since then, we are not aware of further attempts to search for water maser emission in that source.

The observations by Braatz *et al.* (1996) were done with a bandwidth of 50 MHz which corresponds to ≈ 600 km s^{-1} at the $6_{16}-5_{23}$ H$_2$O rest frequency transition (22235.08 MHz).

They report a 1σ noise per channel of 15 mJy for NGC 7469.

We carried out new K-band observations with the Effelsberg 100 m telescope towards NGC 7469. Our aim was to investigate/confirm the presence of the AGN (as in the case of our observations towards Arp 299), and to gain insight into the interaction of this one with its surrounding media. Assuming $T_{\rm sys} \approx 80$ K, we made a request of 3 h on source (using position switching mode) to achieve an rms ~ 3 mJy/beam, enough to get 5σ detections of the putative maser components even if they are as faint as 15 mJy. The observations were carried out under project 17-10 (PI: C. Romero-Cañizales).

We used a bandwidth of 100 MHz and 16384 channels, which were later averaged in order to increase the sensitivity. We achieved a velocity coverage of approximately 1,300 km s^{-1} and a spectral resolution ~ 0.64 km s^{-1}. Thus, in comparison with previous observations from Braatz $et\ al.$ (1996), we improved the sensitivity and the spectral resolution by a factor of three and two, respectively, and we extended the velocity coverage to be able to detect low-velocity/broad features, if present.

No line was detected (see Figure IV.4), in agreement with previous observations, and indicating that, at least in the case of NGC 7469, the non-detection of water maser emission is likely a consequence of obscuration and inclination typical of Seyfert 1 galaxies, suggesting that there is no maser component in our line of sight, and thus, it is undetectable.
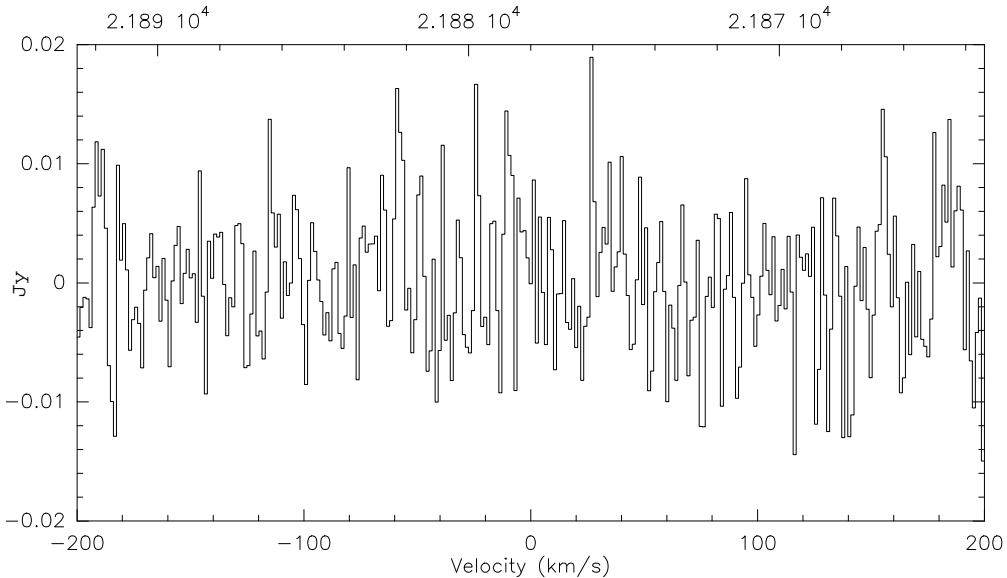
FIGURE IV.4: Water Maser profile of NGC 7469 (experiment 17-10). We only show the inner (and averaged) part of the spectrum, around the central reference frequency, 21.878 GHz, which corresponds to 0 kms.

CHAPTER V

EVN OBSERVATIONS TOWARDS IRAS 23365+3604

This chapter is devoted to our work on the ULIRG IRAS 23365+3604 (already submitted for publication to *MNRAS*). Here I present the first part of an ongoing project entitled "The dominant heating mechanism in the central regions of ULIRGs" (PI: M. A. Pérez-Torres), based on EVN high angular resolution, high sensitivity images of a sample of four of the farthest and brightest ULIRGs in the local Universe (z < 0.1).

V.1 The EVN ULIRG sample

The sample of ULIRGs we present here is the result from a selection process. We first selected those sources from the *IRAS* Revised Bright Galaxy Sample (Sanders *et al.*, 2003) having $\log_{10}(L_{\mathrm{IR}}/\mathrm{L}_\odot) > 12$, from which large supernova rates (ν_{SN}) were expected. We further constrained our sample by selecting those objects with $\delta > -5°$ (in order to obtain a good *uv*-coverage with the EVN), which also appear in the 1.4 GHz Atlas Catalogue of the *IRAS* Bright Galaxy Sample (Condon *et al.*, 1990, 1996), as to ensure their radio emission detection. Finally, we selected those ULIRGs for which neither MERLIN nor deep VLBI data existed in the literature, and for which MERLIN or EVN archival data are not available. The resulting sample contains four of the brightest and farthest ULIRGs in the local Universe (Table V.1), for which we aimed to unveil their dominant heating mechanisms.

The needed rms to obtain 3σ detections of typical type II CCSNe in the most distant ULIRGs of our sample, is quite low ($\sim 2\,\mu\mathrm{Jy}$, for peak luminosities $\sim 10^{27}\ \mathrm{erg\,s^{-1}\,Hz^{-1}}$) and therefore are well below our detection limit. Nevertheless, it is also expected that more luminous systems provide denser environments, which in turn favour the production of very luminous CCSNe (e.g., type IIn SNe in Arp 220; Parra *et al.*, 2007). Moreover, the more luminous a RSN is, the longer it will take for it to reach its peak brightness (see figure 5 in Alberdi *et al.*, 2006). For instance, the RSN A0 discovered in the nuclear region of Arp 299 in 2003 (see Neff *et al.*, 2004), is still detected after several years and

TABLE V.1: The EVN ULIRG sample. Values in columns 2–6 are those provided by Sanders *et al.* (2003). The SN rates in column 7 were obtained following the empirical relation between CCSN rate and $L[8–1000\,\mu\text{m}]$ for starburst galaxies obtained by Mattila and Meikle (2001) (equation I.1), without discounting AGN contribution, if any. In column 8 we show the flux density range a SN would display when having a typical type II and type IIn SN peak luminosity, denoted by $L \sim 10^{27-28}\ \text{erg}\,\text{s}^{-1}\,\text{Hz}^{-1}$.

IRAS name	IRAS position (J2000)		Distance	Redshift	$\log_{10}(L_{\text{IR}}/\text{L}_\odot)$	ν_{SN}	S_ν^{SN}
	$\alpha(^{\text{h m s}})$	$\delta(^{\circ\,\prime\,\prime\prime})$	(Mpc)			(yr^{-1})	(μJy)
(1)	(2)	(3)	(4)	(5)	(6)	(7)	(8)
07251−0248	07 27 37.5	−02 54 55	344	0.088	12.32	5.6	7–71
19297−0406	19 32 22.1	−04 00 02	338	0.086	12.37	6.3	7–73
19542+1110	19 56 35.4	+11 19 03	257	0.065	12.04	3.0	13–127
23365+3604	23 39 01.7	+36 21 14	252	0.064	12.13	3.6	13–132

remains particularly strong (Pérez-Torres *et al.*, 2009b, 2010). A similar scenario in the dense nuclear regions of our sample of ULIRGs can be expected. Furthermore, in the circumnuclear regions of (U)LIRGs, we also expect SN activity to occur. Two remarkable examples are SN 2000ft and SN 2004ip, discovered at 600 pc and 500 pc from the nucleus of galaxies NGC 7469 (Colina *et al.*, 2001; Alberdi *et al.*, 2006; Pérez-Torres *et al.*, 2009a) and IRAS 18293−3413 (Mattila *et al.*, 2007; Pérez-Torres *et al.*, 2007), respectively.

It is worth noting that the empirical relation between CCSN rate and $L[8–1000\,\mu m]$ for starburst galaxies obtained by Mattila and Meikle (2001) (equation I.1), and a similar relation by Condon (1992) (equation I.2), which results in slightly larger values, assume no AGN contribution to the IR or to the FIR luminosity. Thus, if an AGN is present, the values for ν_{SN} in Table V.1, represent upper limits, and a quantitative estimate of the AGN contribution to the IR luminosity is needed before deriving reliable CCSN rates.

V.1.1 The case of IRAS 23365+3604

IRAS 23365+3604 (hereafter IRAS 23365) is thought to be in an advanced merger state (Sopp *et al.*, 1990). There is no companion galaxy so far visible with neither VLA nor 2MASS observations (see e.g. Sopp *et al.*, 1990; Yuan *et al.*, 2010). Klaas and Elsaesser (1991) report a companion candidate, a small galaxy located ≈ 50 kpc (projected distance) away from IRAS 23365, which is however not considered to be the cause of the extremely irregular and disturbed morphology of IRAS 23365. The optical spectrum of this ULIRG seems to be the result of the superposition of LINER and HII-region like components. Such AGN-starburst composite spectrum has been confirmed in other studies (e.g., Veron *et al.*, 1997; Yuan *et al.*, 2010). Chandra X-ray observations have evidenced the presence of an AGN (possibly Compton-thick) in this source (Iwasawa *et al.*, 2011).

At a distance of 252 Mpc (1 mas ≈ 1.2 pc), the high infrared luminosity of IRAS 23365, $\log_{10}(L_{IR}[\,L_\odot] = 12.13)$, corresponds to a CCSN rate of $\approx 3.6\,\mathrm{yr}^{-1}$, according to Equation I.1. As indicated in section V.1, this estimate does not consider an AGN contribution. According to Farrah *et al.* (2003), the AGN contribution in IRAS 23365 is approximately 35% of the total L_{IR}, and the rest is due to a starburst, from which we infer that $\nu_{SN} \approx 2.4\,\mathrm{yr}^{-1}$.

V.2 EVN Observations and data reduction

We performed EVN observations of IRAS 23365 quasi-simultaneously at L- ($\nu \sim 1.7$ GHz or $\lambda \sim 18$ cm) and C-band ($\nu \sim 5$ GHz or $\lambda \sim 6$ cm) in three epochs with a time span among them of approximately one year (see Table V.2).

TABLE V.2: Parameters of the EVN observations. The stations (location, diameter) used in the different observing runs are: Ef-Effelsberg (Germany, 100 m), Wb-Westerbork array (NL, 14×25 m), Jb1-Lovell (UK, 76 m), Jb2-MK II (UK, 25 m), On-Onsala (Sweden, 25 m), Mc-Medicina (Italy, 32 m), Nt-Noto (Italy, 32 m), Tr-Torun (Poland, 32 m), Ur-Urumqi (China, 25 m), Cm-Cambridge (UK, 32 m), Kn-Knockin (UK, 25 m), Ar-Arecibo (Puerto Rico, 305 m), Ys-Yebes (Spain, 40 m).

Label	Project	Observing date	Frequency (GHz)	Participating stations	Phase calibrator	S_{peak} (Jy/beam)
(1)	(2)	(3)	(4)	(5)	(6)	(7)
L1	EP061A	2008-02-29	1.7	Ef, Wb, Jb1, On, Mc, Nt, Tr, Ur, Cm	J2333+3901	0.34 ± 0.02
C1	EP061C	2008-03-11	5.0	Ef, Wb, Jb1, On, Mc, Nt, Tr, Ur, Cm	J2333+3901	0.21 ± 0.01
L2	EP064D	2009-03-07	1.7	Ef, Wb, Jb2, On, Mc, Nt, Tr, Ur, Cm, Kn, Ar	J2333+3901	0.48 ± 0.02
C2	EP064B	2009-02-28	5.0	Ef, Wb, Jb2, On, Mc, Nt, Tr, Ur, Cm, Kn, Ar	J2333+3901	0.23 ± 0.01
L3	EP064J	2010-03-08	1.7	Ef, Wb, Jb1, On, Mc, Nt, Tr, Ur, Cm, Kn	J2330+3348	0.65 ± 0.03
C3	EP064L	2010-03-20	5.0	Ef, Wb, Jb1, On, Mc, Nt, Tr, Ur, Cm, Kn, Ys	J2330+3348	0.64 ± 0.03

Table V.3: EVN observational data, as measured from the images shown in Figure V.3. *Columns* (2) and (3) Peak position coordinates given with respect to $\alpha(J2000) = 23^h39^m01\overset{s}{.}0000$ and $\delta(J2000) = 36°21'08\overset{''}{.}000$. The errors in position (within parentheses), given in mas, were estimated with $FWHM/(2 \times SNR)$, where SNR is the signal to noise ratio, and FWHM was taken as the projection of the beam major axis on both α and δ axes. *Column* (4) rms noise in the maps. *Column* (5) Peak intensities. *Column* (6) Flux densities measured in regions enclosing 5σ level of the emission. *Column* (7) Matched C-band flux densities, covering the 5σ level L-band emission region; this is done by adding the C-band S_{tot} to a 3σ emission in the remaining part. The uncertainties for the measurements shown in columns 5–7 have been estimated by adding in quadrature the rms noise in the map plus a 5% uncertainty in the point source calibration. *Column* (8) Characteristic size (in both α and δ) occupied by the emission at a 5σ level.)

Label	$\Delta\alpha(J2000)$ (s)	$\Delta\delta(J2000)$ ('')	rms (μJy/beam)	S_{peak} (μJy/beam)	S_{tot} (mJy)	S_{match} (mJy)	$R_\alpha \times R_\delta$ (pc^2)
(1)	(2)	(3)	(4)	(5)	(6)	(7)	(8)
L1	0.2600 (0.5)	0.592 (0.5)	28	786 ± 48	7.99 ± 0.40	$\cdots$	207 × 221
C1	0.2614 (0.7)	0.603 (0.7)	16	303 ± 22	0.32 ± 0.02	1.33 ± 0.07	68 × 69
L2	0.2616 (0.7)	0.598 (0.7)	25	466 ± 34	5.42 ± 0.27	$\cdots$	221 × 220
C2	0.2607 (0.5)	0.603 (0.5)	23	584 ± 37	1.11 ± 0.06	2.38 ± 0.12	98 × 94
L3	0.2615 (0.6)	0.566 (0.6)	30	640 ± 44	8.54 ± 0.43	$\cdots$	241 × 259
C3	0.2608 (0.3)	0.599 (0.3)	18	875 ± 47	2.45 ± 0.13	3.52 ± 0.18	111 × 127

All the epochs were VLBI phase-referenced experiments using a data recording rate of 1024 Mbps with two-bit sampling, for a total bandwidth of 128 MHz. The telescope systems recorded both RCP and LCP. The data were correlated at the EVN MkIV Data Processor at JIVE using an averaging time of 2 s in the first two epochs, and 4 s in the third one, since there was no need for a FOV as large as 20 arcsec. The sources 2134+004 and 3C454.3 were used as fringe finders in all the observations. Each epoch lasted 6 hr from which a total of ≈ 3.7 hr were spent on target. Target source scans of 3.5 min were alternated with 1.5 min scans of the phase reference source.

The correlated data of every epoch were analysed using the NRAO AIPS. The overall quality of the visibilities was good and the EVN pipeline products were useful for the initial steps of the data reduction. To improve the calibration, we edited the data to remove artifacts due to RFI and included ionospheric corrections where needed. We exported the data of all the calibrators to the Caltech program DIFMAP and made images and visibility plots of each source. This allowed us to test the performance of each antenna and to determine gain corrections for each. When the gain correction was larger than 10% for a given antenna during the whole observing run, we applied it to the uv-data using the AIPS task CLCOR.

In the first two epochs we used J2333+3901 (at 2.9° angular distance of target) as a phase reference source. This source has a complex structure (see Figure V.1) and it varied in flux density at L-band between both epochs (see column 7 in Table V.2). The subtraction of the phase contribution of J2333+3901 structure from the fringe solutions (delay and rate) was thus necessary. In spite of this correction, the phase referencing of the target source resulted in noisy phases.

In the third epoch we used J2330+3348 (at 3.1° angular distance of our target) as a phase calibrator, which being a predominantly compact source (at mas angular scales) provided a reliable phase reference and calibration. To correct the reference position in our first two epochs, and to align the three observing epochs, we obtained the shifts in right ascension and declination for the first two epochs that make their 15σ emission coincide positionally with the 15σ emission of the third epoch. We did this by means of the task UVSUB in AIPS, in which the data was divided by a point source model of 1 Jy at the wanted reference position.

V.2.1 Imaging process

The extended emission of IRAS 23365 is not completely resolved with the available EVN array. The shortest baselines, such as Ef-Wb, can recover some of the extended emission. If no other short baselines are present (e.g. combinations of Jb, Cm and Kn), it is not

(a)   (b)
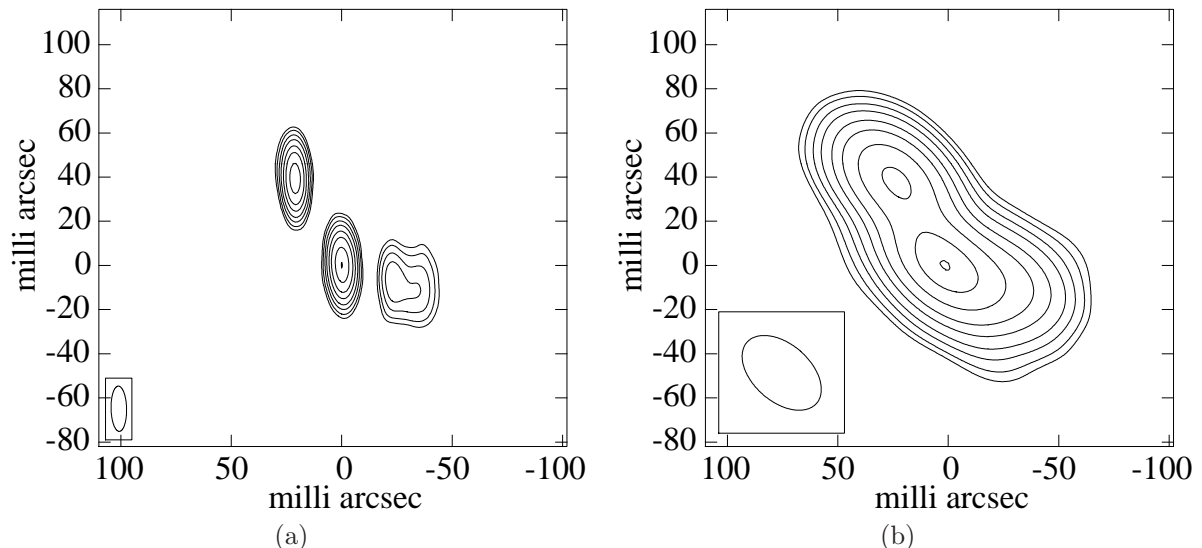
FIGURE V.1: EVN contour maps of the phase reference source J2333+3901 at L-band, in our first (a) and second epoch (b). In the calibration process in epochs 1 and 2, we corrected the rate and delay solutions for the structure of this source before applying the solutions to the target source, IRAS 23365.

possible to determine closure phases, and the presence of strong sidelobes (of the order of the peak) in the dirty map is thus favoured. This situation made very difficult to obtain a reliable image of the target source (see the preliminary maps of IRAS 23365 presented in Romero-Canizales *et al.*, 2008). In principle, removing such short baselines would solve the problem, at the expense of significantly degrading the final image sensitivity.

To properly map the extended emission, a good coverage of short baselines (resulting from combinations of at least three antennas to determine closure phases) is needed. To overcome the lack of short *uv*-spacings, a combination of Gaussian model fitting and imaging algorithms can be used. This is a widely used method for mapping the structure of outflows at VLBI scales (see e.g., Rastorgueva *et al.*, 2011), specially for the cases in which faint diffuse emission is present together with the bright compact one. Epochs 1 and 2 were affected by poor short-baseline *uv*-coverage (the Cm-Kn baseline had a severe amplitude problem and it was not used). In epoch 3, baselines Jb-Kn, Jb-Cm, Cm-Kn and Ef-Wb were present, thus permitting to determine closure phases for the short baselines. As a result, no strong sidelobes affected the imaging process at this epoch. Nevertheless, for this epoch we also used a Gaussian model fitting combined with clean components in order to obtain consistent results with those of the first two epochs. This was done within DIFMAP. We exported the resulting images back into AIPS to analyse them and to produce the final maps that we present here (see Figure V.3).

In Table V.2 we show the stations that participated in each observation. For different reasons, we lost some antennas and/or baselines and the final images were produced using
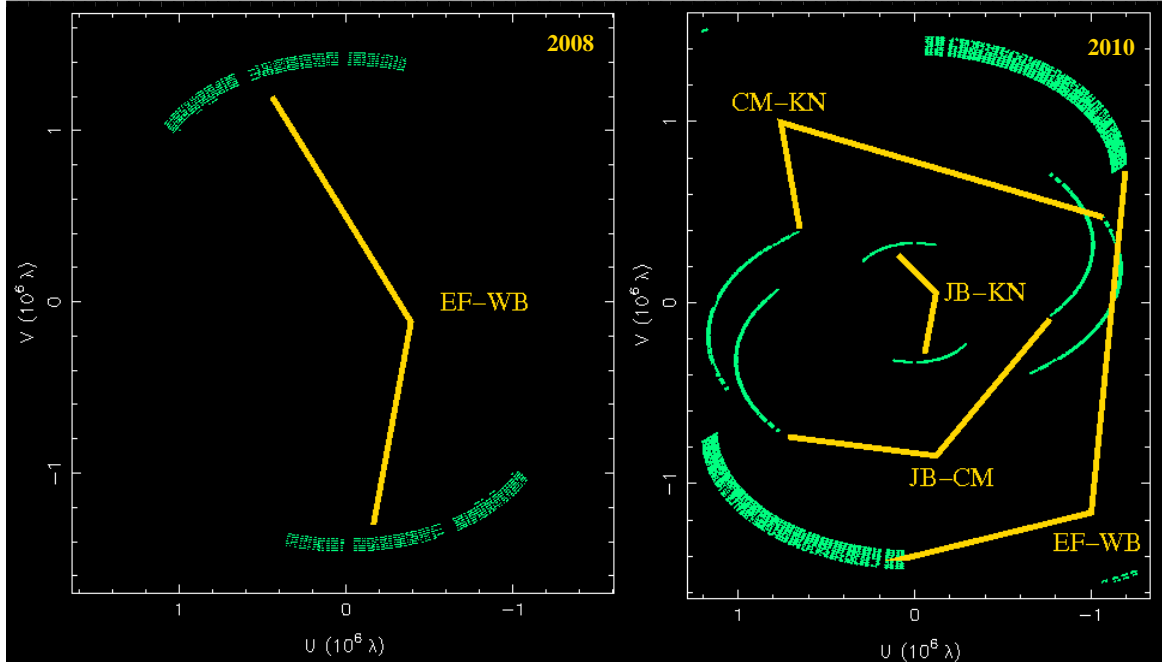
FIGURE V.2: The *uv*-coverage for short baselines (baseline length, $l < 10^6\lambda$) in the first (left panel) and third (right panel) epochs at 1.7 GHz. Note that the poor *uv*-coverage does not provide information for closure phase in the first epoch, and thus a proper imaging of the diffuse emission is not possible; in the third epoch, on the other hand, the short baselines provide a much better *uv*-coverage.

the visibilities resulting from slightly different arrays. For instance, in the second epoch we lost Ur and Ar, and thus the resolution was compromised by the loss of the longest baselines. On the other hand, in the third epoch we had a good coverage of the short baselines (from combinations of Cm, Kn, Jb, Ef and Wb), which eased the reconstruction of the extended emission (see Figure V.2). To allow comparisons among the different epochs and frequencies, we used the same convolving beam (that from the epoch with the worst resolution: $26\times38\,\mathrm{mas}^2$ at $46°$) for the imaging process and sampled the beam using the same cell size $(= 4\,\mathrm{mas})$, and natural weighting for all epochs. The resulting images for the three EVN epochs at the two different frequencies (1.7 and 5 GHz) are shown in Figure V.3. The actual array used in the different epochs, is shown in a label at the upper right corner of each image. In Figure V.4 (bottom) we also show the third EVN epoch at both 1.7 and 5 GHz, as imaged with the natural beam of the observation at 1.7 GHz $(19\times25\,\mathrm{mas}^2$ at $30°)$.

V.3   MERLIN and VLA observations

Simultaneously with our second EVN epoch, we also observed IRAS 23365 at both L- and C-bands with MERLIN (see Table V.4), including the following antennas: Def-

TABLE V.4: Parameters and observational data of complementary **VLA** and **MERLIN** observations (see the corresponding contour maps in Figure V.4). The observations are labelled with a two-letter code, in which the first letter corresponds to the array (V=VLA or M=MERLIN), and the second letter to the observed frequency band (*Column* 3). *Columns* (4) and (5) Coordinates of the peak position, given with respect to $\alpha(J2000) = 23^{\rm h}39^{\rm m}01\overset{\rm s}{.}0000$ and $\delta(J2000) = 36°21'08\overset{''}{.}000$. *Column* (6) - rms noise in the maps. *Column* (7) Peak intensities. *Column* (8) Flux densities measured in regions enclosing 5σ level of the emission. The uncertainties for the measurements shown in columns 4–5 and 7–8 have been estimated as described in Table V.3. *Column* (9) Major and minor axes, obtained by fitting a Gaussian to the source. *Column* (10) Characteristic size (in both α and δ) occupied by the emission at a 5σ level.

Label	Observing date	Freq. (GHz)	$\Delta\alpha$(J2000) (s)	$\Delta\delta$(J2000) ('')	rms (μJy/beam)	$S_{\rm peak}$ (mJy/beam)	$S_{\rm tot}$ (mJy)	$\Theta_{\rm M} \times \Theta_{\rm m}$ (arcsec^2)	$R_\alpha \times R_\delta$ (kpc^2)
(1)	(2)	(3)	(4)	(5)	(6)	(7)	(8)	(9)	(10)
VL	1992-12-14	1.4	0.252 (6.1)	0.54 (6.1)	180	19.14 ± 0.97	25.18 ± 1.27	0.93×0.58	4.48×4.38
VC	1992-12-14	4.9	0.261 (3.3)	0.59 (3.3)	50	9.97 ± 0.21	10.82 ± 0.54	0.46×0.30	4.54×4.16
ML	2009-03-06	1.6	0.260 (1.6)	0.55 (4.0)	200	6.29 ± 0.37	13.90 ± 0.72	0.17×0.14	0.36×0.66
MC	2009-02-25	5.0	0.264 (3.6)	0.56 (8.9)	170	2.39 ± 0.50	5.20 ± 0.31	0.17×0.16	0.32×0.54

ford, Cambridge, Knockin, Darnhall, MK II and Pickmere, observing with a bandwidth of 15 MHz (in both circular polarisations). OQ208 was used as amplitude calibrator (1.1 Jy at L-band and 2.5 Jy at C-band) and J2333+3901 (0.8 Jy at L-band and 0.34 Jy at C-band) as phase calibrator. For phase-referencing, duty times of 7 min/1.5 min in L-band, and 2.5 min/1.5 min in C-band were used, for a total time on source of 4 and 2.5 hr at each band, respectively.

We also analysed archival VLA (A-configuration) data at L- and C-bands (project: AB660, reported in Baan and Klöckner, 2006) to compare with the MERLIN and EVN images. The observations were performed with a bandwidth of 50 MHz (in both circular polarisations). 3C48 (16.0 Jy at L-band and 5.4 Jy at C-band) was the flux calibrator and 0025+393 (0.7 Jy and 0.6 Jy at L- and C-band, respectively) the phase calibrator, which is found at 9.6° angular distance of the target source.

We followed standard procedures within AIPS for the data reduction. Details on the VLA and MERLIN observations are shown in Table V.4 and the resulting images in Figure V.4. We used matched baselines (in wavelengths) to obtain the images for the two different frequencies of each array, to enable the comparison of information at the same scales. For the VLA images we used a common uv-range of 11.5 to 162.7 kλ and same convolving beam of $1.3 \times 1.3 \, \text{arcsec}^2$, while we restricted MERLIN images from 112.6 to 1191.8 kλ, that resulted in a convolving beam of $0.10 \times 0.25 \, \text{arcsec}^2$, at 30°. We did not perform any uv-restriction in the case of the EVN data, to optimize the sensitivity and uv-coverage for each observing epoch.

V.4   Results

IRAS 23365 has been observed at different resolutions (EVN, MERLIN and VLA) and at two different frequencies. This allows a comparison among the different linear scales mapped with different arrays. In the following, we present our results regarding morphology, radio emission, radio spectrum and magnetic field of IRAS 23365. The different parameters measured from the three epochs of EVN observations (see Figure V.3) are presented in Table V.3, and measurements from the VLA archival data and the MERLIN observations are presented in Table V.4. In Table V.5 we show the estimates from the measurements at different scales as shown in Figure V.4.

V.4.1   The IRAS 23365 structure: from kpc- down to pc-scales

The radio images of IRAS 23365 shown in Figure V.4 cover the structure of this galaxy at three different scales: galactic (with the VLA), circumnuclear (with MERLIN) and

TABLE V.5: Physical quantities of IRAS 23365 estimated from VLA, MERLIN and EVN observations. We have used the measured values of S_{peak}, S_{tot} and the largest linear size between R_α and R_δ, from Tables V.3 and V.4. In the case of the EVN, we only include the first epoch of observations, since this is the one that yield a steep spectral index for the peak component (see Figure V.5), thus likely associated to a non-thermal origin. We consider the emission at both bands as measured from the region delimited by the 5σ L-band emission, i.e., using S_{tot} for L-band, and S_{match} for C-band, and the same linear size for both. *Column* (2) Brightness temperature calculated using as the source' solid angle $\Omega_{\mathrm{s}} = \pi(4\log 2)^{-1} (\Theta_{\mathrm{M}} \times \Theta_{\mathrm{m}})$ for the VLA and MERLIN (Table V.4); for the EVN no reliable Gaussian fit can be made to the source (especially in the L-band map) in order to find its deconvolved size, and we have used instead $\Omega_{\mathrm{s}} = \pi(4\log 2)^{-1} (\mathrm{FWHM}_{\mathrm{M}} \times \mathrm{FWHM}_{\mathrm{m}})$, where $\mathrm{FWHM}_{\mathrm{M}}$ and $\mathrm{FWHM}_{\mathrm{m}}$ are the major and minor synthesized beam fitted FWHM. *Column* (3) Monochromatic luminosity at the frequency ν. *Column* (4) Two-point peak pixel-to-pixel spectral index determined from the pixel-to-pixel spectral index distribution obtained with AIPS. *Column* (5) Two-point total spectral index determined between the L- and C-band flux densities ($S_{\mathrm{tot}} \propto \nu^{\alpha_{\mathrm{tot}}^{\mathrm{L\text{-}C}}}$). *Column* (6) Integrated isotropic radio luminosity, considering that the spectral behaviour of the source is straight between L- and C-band. *Column* (7) Equipartition magnetic field. *Column* (8) Characteristic lifetime of electrons subject to B_{eq}, undergoing radiative synchrotron losses.

Label	$\log T_{\mathrm{B}}$ (K)	L_ν ($10^{29}\,\mathrm{erg\,s^{-1}\,Hz^{-1}}$)	$\alpha_{\mathrm{p\text{-}p}}^{\mathrm{L\text{-}C}}$	$\alpha_{\mathrm{tot}}^{\mathrm{L\text{-}C}}$	L_{R} ($10^{39}\,\mathrm{erg\,s^{-1}}$)	B_{eq} (μG)	τ_{syn} (Myr)
(1)	(2)	(3)	(4)	(5)	(6)	(7)	(8)
VL	4.45 ± 0.02	19.11 ± 0.97	-0.46 ± 0.06	-0.69 ± 0.06	4.1	18.4	11.4
VC	3.61 ± 0.02	8.21 ± 0.41				18.1	6.2
ML	5.42 ± 0.02	10.55 ± 0.55	-0.66 ± 0.13	-0.89 ± 0.07	2.0	77.1	1.1
MC	3.96 ± 0.03	3.95 ± 0.24				90.8	0.6
EL	6.81 ± 0.02	4.94 ± 0.25	0.52 ± 0.13	-0.59 ± 0.06	1.1	174.7	0.4
EC	5.57 ± 0.02	2.58 ± 0.13				174.7	0.2
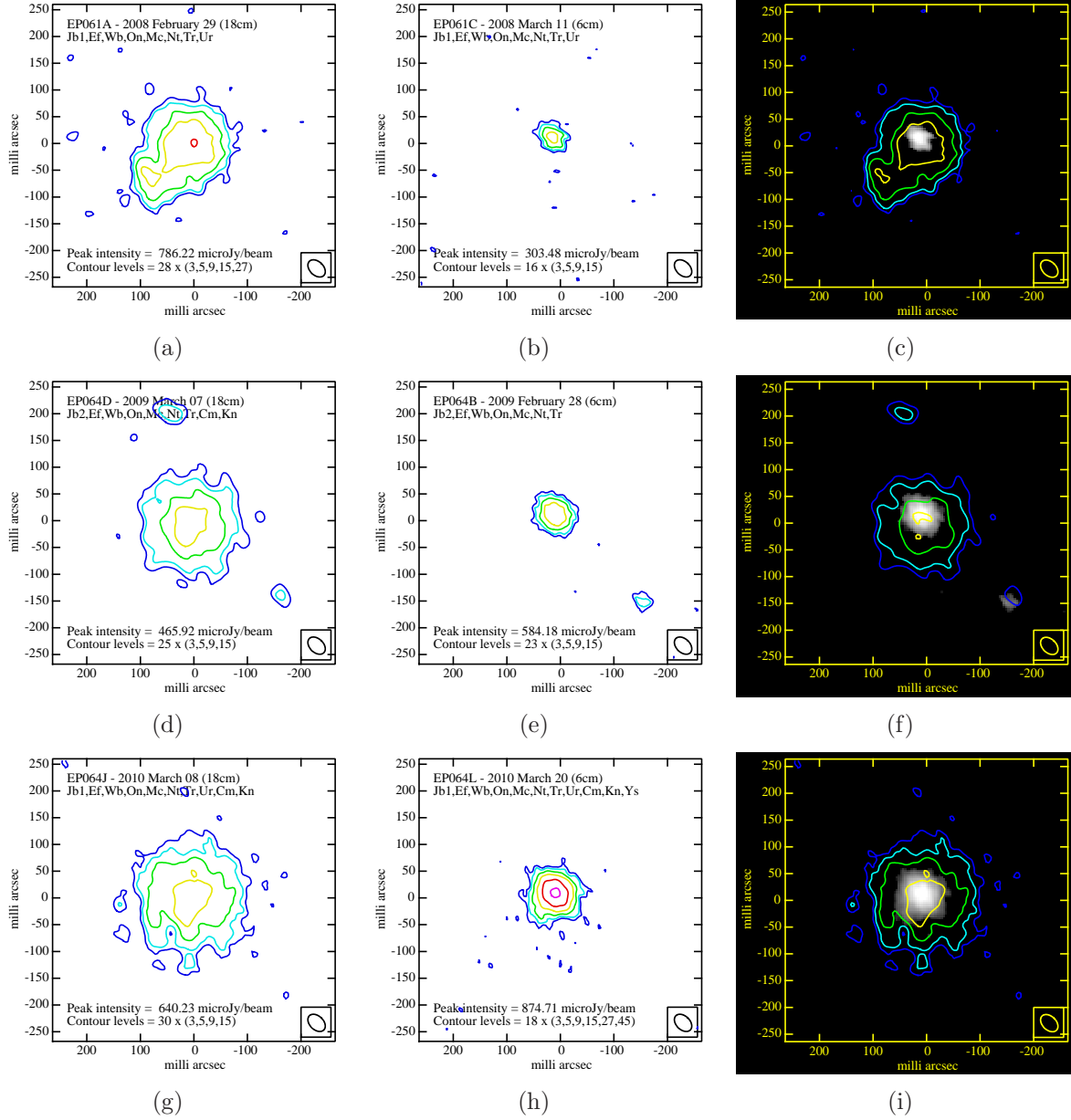
FIGURE V.3: IRAS 23365 at L-band (left: (a), (d), (g)), C-band (middle: (b), (e), (h)), and L-band contours overlaid on grey scale C-band images (right: (c), (f), (i)), in three different epochs (top to bottom). All the images have been degraded to the epoch with lowest resolution (L2, following the labels in Table V.2), being therefore convolved with the same beam size: $26 \times 38 \, \mathrm{mas}^2$ at $46°$. The maps are centred at $23^h39^m01^s.29$, $+36°21'08''.59$ (J2000). In the upper left corner of each image, we provide the EVN project code, observation date, observed wavelength and the list of antennas used for mapping. In the lower left corner we show the peak intensity, noise and contour levels information. The size of the nuclear region seems to increase from one epoch to another at both frequencies, although images from the same frequency were convolved with the same beam. We consider that this is an effect of the difference in the arrays used, rather than being an intrinsic change in the source, albeit this possibility cannot be ruled out. It is worth noting that the size of the nuclear zone is consistently larger at L-band than its counterpart at C-band. This can be explained by the longer lifetime at lower frequencies of the electrons being accelerated in the innermost nuclear regions.

nuclear (with the EVN). We used the third epoch of EVN observations to compare with the VLA and MERLIN images, since that was the epoch with the best compromise between angular resolution and sensitivity (see §V.2.1 for details).

At galactic scales, the emission at both L- and C-bands is unresolved and appears concentrated in a zone of ~ 4.5 kpc in size. At circumnuclear scales, the emission is concentrated in the inner 0.5 kpc region and displays an unresolved component on top of extended structure.

At the highest resolution in L-band, the nuclear region has a size $\gtrsim 200$ pc at all the EVN epochs (see Table V.3), and shows variations in its morphology (see Figure V.3). At C-band, the emitting region is about 100 pc and its structure remains quite compact in the first two epochs, whilst some more extended emission is traced in the third epoch (see Figure V.3). A single Gaussian fit is inaccurate for obtaining the deconvolved size of the emitting region, at least for the emission at L-band, due to the wealth of extended emission. We thus characterize the area of the emitting region with the size of the source in both the right ascension and declination axes, R_α and R_δ, respectively (Table V.3). There are some features outside the nuclear regions that, while having peaks slightly above 5σ in our second epoch (Figures V.3(d) and V.3(e)), are not seen neither in our first epoch, nor in our third observing epoch. While these could be real features (in particular, the compact source detected at both frequencies with $\Delta\alpha$, $\Delta\delta \sim 150$ mas), we conservatively consider them as tentative detections (see §V.2.1 for details) and therefore are not discussed here.

We note that the size of the emission area increases with time through the different EVN epochs at both frequencies (see Table V.3), and also displays different morphology (see Figure V.3), especially at L-band. Whereas sensitivity does not seem to vary drastically among epochs, the observations were performed at different hour angles and thus the uv-plane was sampled at different orientations. In the first epoch, the short and intermediate baselines resulted in a better uv-coverage in the North-South direction, thus making the array more sensitive to extended structure in the East-West direction. In the second and third epochs, the array was more sensitive to the extended structure in the NE-SW and NW-SE directions, respectively. Hence, the differences in size and morphology could have been affected by the different uv-coverages.

Regardless of the used array (i.e., VLA, MERLIN or EVN), and albeit of using matched baselines (at least for VLA and MERLIN), the emission in L-band consistently occupies a larger extension than that at C-band, around a factor of 2 in the case of the EVN, as seen in Figure V.4, where we show for comparison the VLA, MERLIN and EVN (third epoch) images. This can be explained by the longer lifetime of accelerated electrons emitting synchrotron radiation at lower frequencies (see §V.4.4).

We also note that the peak positions at the two different frequencies are not coincident neither for MERLIN nor for the EVN. In the case of the VLA, we do not have the needed angular resolution to confirm any shift; however, at the higher resolution provided by both MERLIN and EVN, a shift of the C-band peak towards the North-East direction is evident, while that at L-band is shifted towards the South-West (see Tables V.3 and V.4 and Figure V.4). This result is consistent for all the epochs and at the different angular resolutions provided by EVN and MERLIN. We interpret those shifts of the emission peaks as evidence for at least two different populations of radio emitters being present in the nuclear region, emitting the bulk of their energy at different frequencies (see §V.4.2). Furthermore, the peak component is variable both in position and in intensity among EVN epochs, and in each epoch, being also different between frequencies. These facts give evidence of the source variability within the innermost nuclear region.

V.4.2   The radio emission and radio spectrum at different scales

We mentioned in the previous section that the radio emission at different frequencies seen at the different resolutions (except perhaps for the VLA), peaks at different positions. Thus, a peak spectral index defined as $S_{\text{peak}} \propto \nu^{\alpha_{\text{peak}}^{\text{L-C}}}$ would me meaningless. We use instead the peak of the pixel-to-pixel spectral index distribution ($\alpha_{\text{p-p}}^{\text{L-C}}$) as obtained with AIPS.

The radio emission of both galactic and circumnuclear regions of IRAS 23365 mapped with the VLA and MERLIN, respectively, is stronger at L-band than at C-band (see columns 7 and 8 in Table V.4). Consequently both total spectral indices ($S_{\text{tot}} \propto \nu^{\alpha_{\text{tot}}^{\text{L-C}}}$) and peak pixel-to-pixel spectral indices ($\alpha_{\text{p-p}}^{\text{L-C}}$) are steep, as shown in columns 4 and 5 of Table V.5. Steep spectral indices are an indication of non-thermal emission. We note however that the T_{B} values (column 2 in Table V.5) at galactic (L- and C-bands) and circumnuclear (C-band) scales, are in principle consistent with either thermal emission, or with synchrotron emission suppressed by free-free absorption from e.g., HII regions. The calculated value for the free-free opacity (τ_{ff}) implies that thermal emission should be optically thick. Therefore, the bulk of emission at L- and C-bands correspond to optically thin non-thermal synchrotron emission, slightly affected by free-free absorption at galactic ($\tau_{\text{ff}} \approx 0.02$) and circumnuclear ($\tau_{\text{ff}} \approx 0.20$) scales.

Regarding the nuclear region (mapped with the EVN), the large T_{B} values imply a non-thermal origin for the radio emission. The attained angular resolution and the presence of strong extended (a few mJy; see Tables V.3, and V.4) radio emission prevents us from directly detecting individual faint (see Table V.1) compact sources, e.g. SNe. However, we note that S_{peak} and S_{tot} show variations at both frequencies during our EVN monitoring
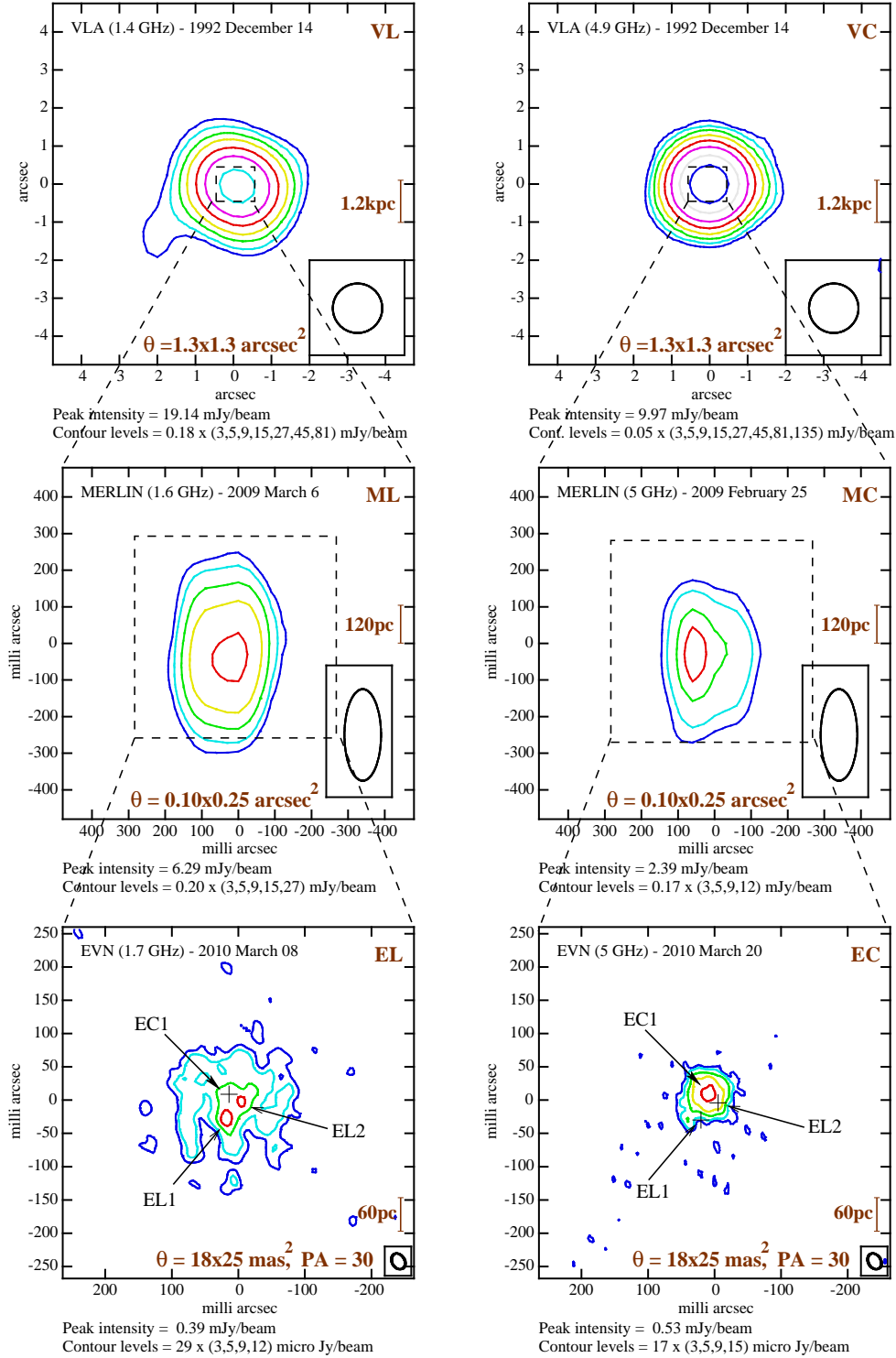
FIGURE V.4: IRAS 23365 as seen at different frequencies and resolutions (higher resolution from top to bottom; and higher frequency from left to right, see labels). All the maps are centred at $23^h39^m01^s29$, $+36°21'08''59$ (J2000). The cross in the EL image indicates the peak position (EC1) as measured from the EC image, and the crosses in the EC image indicate the positions of components EL1 and EL2. The non-coincidence of the peaks at the two different frequencies (see also ML and MC images), indicates the presence of distinct population of sources in the innermost nuclear region. We note that at C-band, IRAS 23365 remains practically unresolved, whilst L-band images show more extended structure.

83

campaign (see Table V.3). Whereas in C-band, S_{peak} and S_{tot} increase with time, in L-band these diminish in the second epoch, and then increase in the third one, thus indicating the variability of sources and/or the appearance of new ones within the nucleus, e.g., new SNe, accounting to the expected SN rate ($\approx 2.4\,\mathrm{yr}^{-1}$). This non-correlated behaviour at both frequencies is indicative of nuclear activity that becomes transparent at different frequencies (first at C-band and later at L-band) and different times.

V.4.3 Spectral index distribution at mas-scales

Let us now concentrate in the spectral indices corresponding to the EVN images. Considering the total flux densities as measured from the region within the 5σ L-band emission (i.e. L-band flux from column 6, and C-band flux from column 7 in Table V.3), the total spectral indices ($\alpha_{\mathrm{tot}}^{\mathrm{L\text{-}C}}$) are steep for all the epochs. However, the situation is different for the peak pixel-to-pixel spectral index ($\alpha_{\mathrm{p\text{-}p}}^{\mathrm{L\text{-}C}}$), which is evolving with time. The distribution of $\alpha_{\mathrm{p\text{-}p}}^{\mathrm{L\text{-}C}}$ is shown in Figure V.5 for the three EVN epochs. In the first epoch of EVN observations, $\alpha_{\mathrm{p\text{-}p}}^{\mathrm{L\text{-}C}}$ is steep, then it becomes inverted in our second epoch, and starts to decrease (although being still inverted) in the third epoch to presumably become steep again. This is clear evidence of the variation in flux of sources within the innermost nuclear regions, and/or appearance of new sources (e.g., SNe) which would be seen first at higher frequencies and later on at lower frequencies (Weiler *et al.*, 2002), in agreement with our results. We also note that for the three EVN epochs, $\alpha_{\mathrm{p\text{-}p}}^{\mathrm{L\text{-}C}}$ (which is given pixel by pixel as shown in Figure V.5), becomes steeper as measured towards the edges of the C-band emission, where the noise at C-band starts to dominate, whilst there is still extended emission detected at L-band. This is a consequence of the ageing of the population of electrons radiating synchrotron emission (see §V.4.4).

V.4.4 The magnetic field in the energy budget of IRAS 23365

In previous sections, we have gathered information about the ongoing non-thermal activity of IRAS 23365 at different scales. In a ULIRG environment, we expect SNe, SNRs and/or an AGN to be the engines responsible for producing high energy particles which will interact with the galactic magnetic field, thus generating synchrotron radiation (dominating at $\nu \lesssim 30\,\mathrm{GHz}$; Condon, 1992). The energy thus produced, will be present in the form of relativistic particles and magnetic field. In the following, we investigate the energy budget (due to synchrotron radiation) of IRAS 23365 at different scales, i.e., as estimated from observations with different arrays (EVN, MERLIN and VLA). We only consider the third epoch of observations with the EVN, to compare with the results from
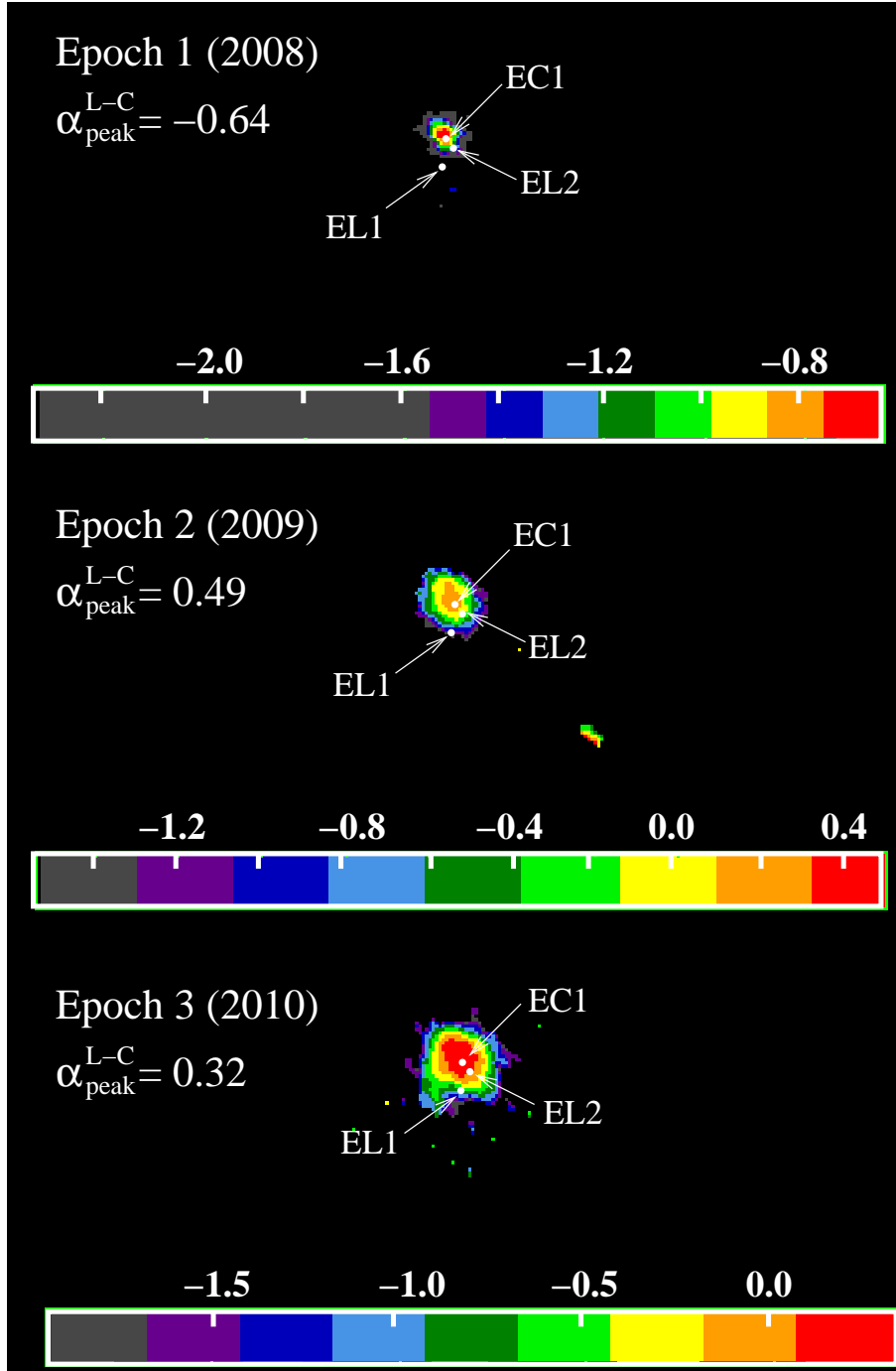
FIGURE V.5: Evolution of the spectral index distribution ($S_{\text{pixel}} \sim \nu^{\alpha_{\text{p-p}}^{\text{L-C}}}$), given pixel by pixel (as obtained from AIPS) in the nuclear zone, which we expect to be composed by non-thermal sources (e.g. SNe and AGN). Note that while the peak of the spectral index distribution varies in the very central region, it becomes steeper towards the edges, due to the longer lifetime of the electrons at lower frequencies. The sources EC1, EL1 and EL2 are marked with white filled circles (see Section V.4.5).

the VLA and MERLIN, since this epoch was the one which had the least imaging problems (see §V.2.1).

We can estimate the average equipartition magnetic field based on the radio emission of IRAS 23365 as follows (see Pacholczyk, 1970),

$$\left(\frac{B_{\text{eq}}}{\mu\text{G}}\right) \approx 8.1 \left[\frac{(1+k)}{\phi}\left(\frac{c_{12}}{10^7}\right)\left(\frac{R}{1\,\text{kpc}}\right)^{-3}\left(\frac{L_{\text{R}}}{10^{39}\,\text{erg s}^{-1}}\right)\right]^{2/7} \tag{V.1}$$

where ϕ is the filling factor of fields and particles, k is the ratio of heavy particle energy to electron energy, and c_{12} is a function that depends on the minimum and maximum frequencies considered, and of the two-point spectral index, $\alpha_{\text{tot}}^{\text{L-C}}$, which is estimated based on those two frequencies (see Pacholczyk, 1970):

$$c_{12} = \frac{c_1^{1/2}}{c_2}\frac{2\alpha - 2}{2\alpha - 1}\frac{\nu_1^{(1-2\alpha)/2} - \nu_2^{(1-2\alpha)/2}}{\nu_1^{1-\alpha} - \nu_2^{1-\alpha}} \quad \text{g}^{3/4}\text{cm}^{-3/4}\,\text{s}^{-1/2},$$

with

$$c_1 = \frac{3e}{4\pi m^3 c^5} = 6.27 \times 10^{18} \quad \text{g}^{-5/2}\,\text{cm}^{-7/2}\,\text{s}^4 \qquad \text{and}$$

$$c_2 = \frac{2e^4}{3m^4 c^7} = 2.37 \times 10^{-3} \quad \text{g}^{-2}\,\text{cm}^{-1}\,\text{s}^3.$$

L_{R} is the integrated isotropic radio luminosity between the minimum and maximum frequencies used, and R is the linear size occupied by the emission, taken as the larger value between R_α and R_δ in each case (see column 10 in Table V.4 for the VLA and MERLIN). For the third EVN epoch, we determined a maximum linear size $R \approx 0.2\,\text{kpc}$ with TVDIST within AIPS. For simplicity, we consider $\phi = 0.5$ and $k = 100$ (see e.g., Pérez-Torres and Alberdi, 2007).

In Table V.5 we show the average values for $\alpha_{\text{tot}}^{\text{L-C}}$, L_{R} and B_{eq}, obtained within the emission regions sampled by the different instruments. In the innermost nuclear region (imaged with the EVN), the strength of the magnetic field is larger than the one measured at lower resolutions. This is expected, since the plasma in the central regions should be denser than in the outer regions, and thus the magnetic field lines therein, frozen within the plasma, should be more concentrated. The average magnetic field under energy equipartition, for the emission measured with the VLA, MERLIN and the EVN, would be 18, 84 and 175 μG respectively. The latter value represents the peak of B_{eq} coming from the very central region. If the synchrotron spectrum holds beyond the C-band frequencies, e.g. to 20 GHz, the estimated values for B_{eq}, would only be $\sim 15\%$ larger.

Our obtained B_{eq} value at galactic scales is consistent with that of a galaxy in advanced interaction state, probably close to nuclear coalescence, according to VLA studies

of interacting galaxies by Drzazga *et al.* (2011). Likewise, the B_{eq} value at nuclear scales is similar to that found through VLBI studies of the ULIRG IRAS 17208-0014 (144 μG; Momjian *et al.*, 2003), which is also an advanced merger.

Considering the obtained values for B_{eq}, and following Pacholczyk (1970), we can calculate the lifetime of the electrons with energy E_{min}, which move in a magnetic field of strength B_{eq}, thus emitting synchrotron radiation around a critical frequency ν_c. This is,

$$\tau_{syn} = \frac{E_{min}}{|-\frac{dE}{dt}|} = \frac{1}{c_2 E_{min} B_{eq}^2},$$

$$\Rightarrow \left(\frac{\tau_{syn}}{Myr}\right) \approx 1.06 \times 10^3 \left[\left(\frac{\nu_c}{GHz}\right)\left(\frac{B_{eq}}{\mu G}\right)^3\right]^{-1/2} \tag{V.2}$$

From §V.4.1, we know that the radio emission at L- and C-bands has a different extent and peaks at different positions within the nuclear region, which strongly suggests the presence of different populations of particles. This is more evident in the nuclear region mapped with the EVN: in the innermost region, where there is an overlap between the emission at the two different frequencies, there would be a concentration of very energetic, short-lived particles, whereas the outer region would be populated by less energetic, long-lived particles, which have had time to diffuse from the inner regions into the outer ones. In Table V.5 we show the values for τ_{syn}, assuming that the critical frequency is either that of the L-band or the C-band. In all cases we see that the L-band emission is tracing the emission from an older population of electrons (regardless of the resolution) than the one emitting at C-band frequencies. The putative AGN together with an ensemble of SNe, for which evidence has been found in other studies (see §V.1.1), must be located within the C-band emission region as seen with the EVN, where the magnetic field strength is larger, and where a composite spectrum (which varies with time) has been found (§V.4.2).

We note that the radio lifetime of the emitting source is not only determined by τ_{syn}. The lifetime of relativistic electrons might also be affected by Compton losses given by

$$\tau_C = \frac{25.2}{U_{rad} E_{min}},$$

(following Pacholczyk, 1970) since the electrons are immersed in a radiation field,

$$U_{rad} = \frac{4\pi}{c}\frac{L_{bol}}{\Omega_s},$$

for which we take L_{IR} as a good approximation to the bolometric luminosity L_{bol}. U_{rad} varies from $\approx 2.5 \times 10^{-7}$ erg cm^{-3} at galactic scales, up to $\approx 2.8 \times 10^{-4}$ erg cm^{-3} at nuclear

scales. To compare the different losses, we calculate their ratio,

$$\frac{\tau_{\mathrm{C}}}{\tau_{\mathrm{syn}}} = \frac{25.2 c_2 B_{\mathrm{eq}}^2}{U_{\mathrm{rad}}}.$$

We note that at all scales (nuclear, circumnuclear and galactic) and at both L- and C-band, we obtain $\tau_{\mathrm{syn}} \gg \tau_{\mathrm{C}}$, with a ratio ranging between 6.5×10^{-6} (nuclear scales) and 8.8×10^{-5} (galactic scales); i.e., the energy density of the radiation field, greatly exceeds the magnetic energy density. Radiative losses are thus important and we argue that there is need for injection of new electrons or a continuous acceleration to halt the energy depletion, otherwise radio emission would not be visible.

The re-acceleration or injection of new electrons in a (U)LIRG environment, is very likely provided in SN-shells and SNRs by first order Fermi acceleration. The presence of SNe, SNRs and a strong magnetic field in IRAS 23365, agrees with this scenario.

V.4.5   The nuclear region in the third EVN epoch

Among the EVN observing epochs, the third one benefited from a better uv-coverage, and thus resulted in a smaller natural beam ($19 \times 25 \,\mathrm{mas}^2$ at $30°$). The L-band map (Figure V.4, bottom-left) shows the presence of two compact sources (EL1 and EL2) within the nuclear region, without counterparts at C-band. On the other hand, the compact source that dominates the emission at C-band, labelled as EC1 (Figure V.4, bottom-right), has no compact counterpart at L-band, although it is embedded within the diffuse emission at L-band.

To obtain EC1, EL1 and EL2 peak intensities, we first need to estimate the background emission where these compact sources lay. We have solved for the 'zero level' emission ($S_{\mathrm{bg}} \sim 179 \pm 24 \,\mu\mathrm{Jy}$ at C-band and $S_{\mathrm{bg}} \sim 211 \pm 12 \,\mu\mathrm{Jy}$ at L-band) using the task IMFIT within AIPS. We have then subtracted this value from the maximum intensity found at the positions of each compact source, in order to obtain their S_{peak}. In Table V.6 we give the positions for EC1, EL1 and EL2, their peak intensities, as well as their estimated L_ν and T_{B}, which are indicative of a non-thermal origin.

EC1 lays on a region where $\alpha_{\mathrm{p\text{-}p}}^{\mathrm{L\text{-}C}}$ changes with time, suggesting variability within this region. We note that EC1 is confined to a small area in the first epoch, and then appears to increase in size, as we have mentioned in Section V.4.1. Whilst EL1 lays in a region which maintains a very steep $\alpha_{\mathrm{p\text{-}p}}^{\mathrm{L\text{-}C}}$ through time, EL2 is found in a region with varying $\alpha_{\mathrm{p\text{-}p}}^{\mathrm{L\text{-}C}}$ (Figure V.5). We cannot rule out that the $\alpha_{\mathrm{p\text{-}p}}^{\mathrm{L\text{-}C}}$ variations at EL2, are affected by the fact that more extended emission is being traced from the first epoch to the third one.

TABLE V.6: Parameters derived for the compact components EC1, EL1 and EL2 found within the extended emission in the third epoch of EVN observations (Figure V.4). *Columns* (2) and (3) Coordinates of the peak position, given with respect to $\alpha(J2000) = 23^{\mathrm{h}}39^{\mathrm{m}}01\overset{\mathrm{s}}{.}0000$ and $\delta(J2000) = 36°21'08\overset{''}{.}000$. *Column* (4) Peak intensity corrected by the zero level emission. *Column* (5) Monochromatic luminosity. *Column* (6) Brightness temperature, considering that the solid angle subtended by the source is that subtended by the synthesized beam (as in Table V.5).

Label	$\Delta\alpha$(J2000)	$\Delta\delta$(J2000)	S_{peak}	L_ν	$\log T_{\mathrm{B}}$
	$(^{\mathrm{s}})$	$('')$	(μJy/beam)	(10^{28} erg s^{-1} Hz^{-1})	(K)
(1)	(2)	(3)	(4)	(5)	(6)
EC1	0.2608 (0.4)	0.599 (0.4)	352 ± 35	2.67 ± 0.26	4.56 ± 0.04
EL1	0.2597 (1.7)	0.586 (1.7)	150 ± 32	1.14 ± 0.24	5.15 ± 0.09
EL2	0.2616 (1.4)	0.561 (1.4)	184 ± 33	1.39 ± 0.25	5.23 ± 0.08

In the case of EC1, both the variability of the radio emission (see §V.4.2) and of the spectral index distribution (see §V.4.3 and Figure V.5), are indicative of recent non-thermal activity (probably due to SNe and AGN activity). EL1 and EL2 display brightness temperatures similar to those expected from either type II SNe or SNRs. We note that the maximum linear size for EL1 and EL2 is set by the beam size to $\sim 30\,\mathrm{pc}$, which is too large for characterising either an individual SN or a SNR. A scenario in which EL1 and EL2 are clusters of SNe is difficult to reconcile with the absence of peaks of emission at C-band in all the EVN observing epochs, and with the behaviour of $\alpha_{\mathrm{p\text{-}p}}^{\mathrm{L\text{-}C}}$ at both EL1 and EL2. These facts suggest that there is no recent activity from young SNe in those regions, and favour an scenario in which EL1 and EL2 are dominated by an old population of radio emitters.

CHAPTER VI

DISCOVERY OF THE STARBURST-AGN NUCLEUS IN IC 883

IC 883 is a LIRG at a distance of 100 Mpc (1 mas $\approx$ 0.48 pc), with IR luminosity ($L_{\rm IR} = L[8\text{–}1000\ \mu{\rm m}]$) $\sim 4.7 \times 10^{11}$ L$_\odot$ (Sanders *et al.*, 2003). Taking $L_{\rm IR}$ as a measure of the rate at which massive stars are formed, we find a corresponding CCSN rate, $\nu_{\rm SN}$, of $\sim 1.3\,{\rm yr}^{-1}$ for this LIRG (assuming the empirical relation obtained by Mattila and Meikle, 2001, equation I.1 in this thesis.).

Optical spectroscopic studies by Veilleux *et al.* (1995) have led to the classification of IC 883 as a LINER. However, Yuan *et al.* (2010) have recently reclassified this galaxy as a composite starburst-AGN based on the revised optical diagnostic diagrams by Kewley *et al.* (2006). It is then expected that an AGN is contributing to the total $L_{\rm IR}$ in IC 883, thus implying that the $\nu_{\rm SN}$ should be lower than $1.3\,{\rm yr}^{-1}$.

The ongoing program "An Altair study of Supernovae in Luminous Infrared Galaxies" (PI: S. Ryder), using Gemini-North laser guide star AO, has yielded the discovery of two CCSNe in IC 883 within the last year: SN 2010cu (24 Feb. 2010, Ryder *et al.*, 2010a) and PSN J13203538+3408222 (11 Feb. 2011, Kankare *et al.*, 2011b), which we refer to as SN 2011xx henceforth. Kankare *et al.* (2011a) report the discovery in the NIR of both SNe, and their NIR follow-up (see Figure VI.1).

Note that the discovery of two SNe in one year results in $\nu_{\rm SN} \approx 2^{+2.6}_{-1.3}\,{\rm yr}^{-1}$ (using the upper and lower Poisson 1σ uncertainties for two events given by Gehrels, 1986), which matches within the uncertainties the expected $L_{\rm IR}$-based CCSN rate of the galaxy.

In Sections VI.1.1 and VI.1.2 we give details of our radio observations towards the nuclear and circumnuclear regions of IC 883, and in Section VI.2 we present our results and discussion.
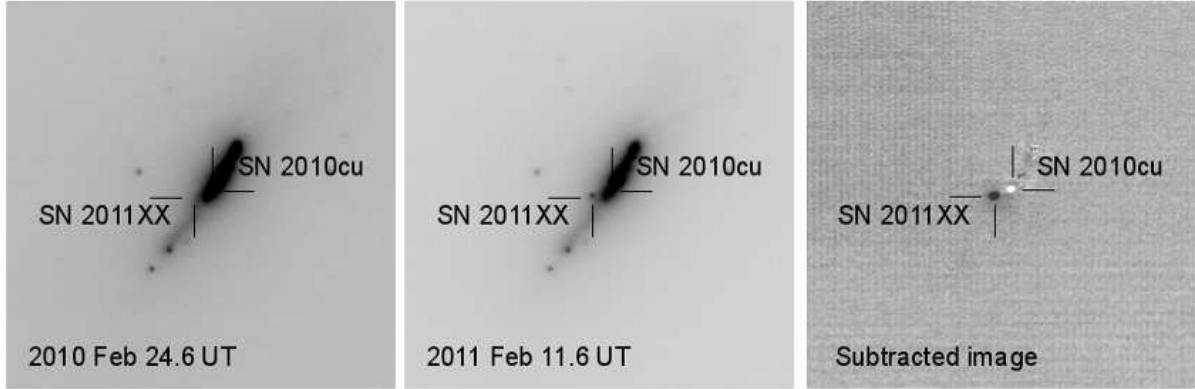
FIGURE VI.1: Detection images at $2.2\,\mu\mathrm{m}$ of SN 2010cu (left) and SN 2011xx (middle) obtained with the NIRI and the ALTAIR laser-guide-star adaptive-optics system on the Gemini-North Telescope on 24 February 2010 and on 11 February 2011, respectively. In the subtracted image (right panel), SN 2011xx is clearly visible, whilst SN 2010cu seems to have faded below the NIR detection limit. The FOV in each image is $10'' \times 10''$. Credit: Kankare *et al.* (2011a).

VI.1   Observations

VI.1.1   e-EVN observations and data reduction

We observed IC 883 on 23 March 2011 (project: RR006, ToO; PI: C. Romero-Cañizales) at 5 GHz, with the e-EVN, which included the following antennas (diameter, location): Ef-Effelsberg (100 m, Germany), Jb2-Mark II (25 m, UK), Mc-Medicina (32 m, Italy), On-Onsala (25 m, Sweden), Tr-Torun (32 m, Poland), Wb-Westerbork array (14×25 m, NL) and Ys-Yebes (40 m, Spain).

RR006 was a 2 hr experiment ($\sim$1.3 hr, total time on source), recorded at 1024 Mbps using eight subbands, each of 16 MHz and dual polarisation. The data were correlated at the EVN MkIV Data Processor at JIVE with an averaging time of 2 s. The point-like source J1159+2914 (2.45 Jy at 5 GHz) was used as a fringe finder and bandpass calibrator. J1317+3425 (0.35 Jy at 5 GHz), at $\sim 0.7°$ angular distance from IC 883, served as phase reference source. 3.4 min scans on IC 883 were alternated with 1.2 min scans on J1317+342. The data were analysed using AIPS. We also used DIFMAP to image the calibrators and to assess the antennas performance.

The SN 2011xx coordinates derived from the NIR images were used for pointing and correlation. A local rms of $\sim 30\ \mu$Jy/beam was achieved at the pointing centre. Since no radio source was detected above 3σ at that position, we corrected the visibility data with the task *UVSUB* in AIPS, to account for the correlation offset from the position of the strongest source in the field, i.e., to the radio nucleus of IC 883. The shift of ~ 0.8 arcsec
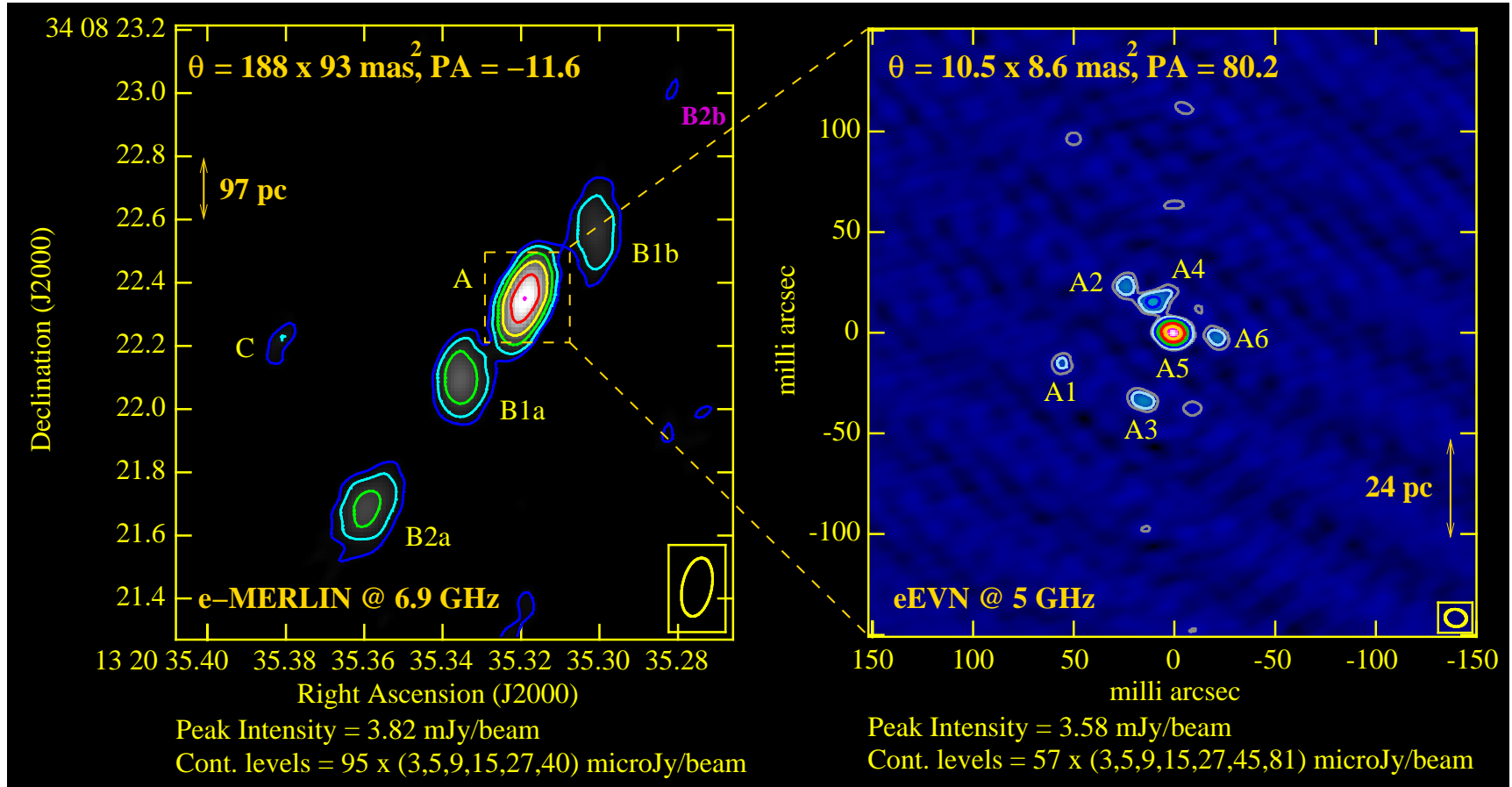
FIGURE VI.2: IC 883 contour images at 6.9 GHz with e-MERLIN (left), and at 5 GHz with the e-EVN (right). The rms noise in each image is 95 and 57 μJy/beam, respectively. Note that the brightest component at e-MERLIN scales is dominated by a compact source seen at mas scales with the e-EVN. A 3σ source (B2b) detected in the e-MERLIN image is shown in magenta (see Section VI.2.1 for details).

is well within the primary beam of each antenna. We achieved a final thermal rms in the map of 57 μJy/beam, for a beam size of 10.49×8.55 mas^2 at 80.2°(see Figure VI.2, right panel). The image was made within AIPS, using natural weighting and ROBUST=0.

VI.1.2   e-MERLIN observations and data reduction

We carried out e-MERLIN observations of IC 883 at 6.9 GHz (median central frequency) on 24 March 2011. These were director's discretionary time (DDT) observations within the commissioning phase of e-MERLIN, which included the following 25 m diameter antennas: Mark II, Defford, Knockin, Darnhall and Pickmere. The observations lasted ∼ 24 hr, from which approximately 20 were spent on target and 10 hr were ultimately usable after editing. Four subbands (512 channels each) with dual polarisation were used, accounting for a total bandwidth of 512 MHz.

We analysed the data within AIPS. 3C286 set the absolute flux density scale following an iterative process. The flux estimated for 3C286 in the shortest baseline (Mark II-Pickmere), at the centre of the different subbands, was on average 5.56 Jy. We then calibrated the amplitude of DA 193, which is a bright and unresolved source as seen by all e-MERLIN baselines, resulting in an average flux of 3.72 Jy. Finally, we used DA 193 to set the flux density of the phase reference source, 1324+363, which resulted in an average flux density of 68.25 mJy. We performed a series of phase-only self-calibration iterations of the phase reference source, before phase-calibrating the target source. We achieved a thermal rms noise in the IC 883 map of 95 μJy/beam, for a beam size of 188×93 mas^2 at −11.6° (see left panel in Figure VI.2), obtained with natural weighting and ROBUST=1 within AIPS.

VI.2   Results and discussion

The e-EVN and e-MERLIN images of IC 883 are shown in Figure VI.2. In Table VI.1 we report the estimated parameters for the $> 5\sigma$ detected sources in both images, as well as a 3σ e-MERLIN source (B2b) which is useful in light of the studies by Clemens and Alexander (2004) (see Section VI.2.1).

VI.2.1   Starburst-AGN nature and radio structure of IC 883

The quest for SN 2011xx has brought the opportunity to unveil different facets of IC 883. First of all, our e-EVN observations (see right panel in Figure VI.2) reveal the presence of at least six compact sources above 5σ in the innermost nuclear region of IC 883, one of

TABLE VI.1: Estimated parameters of the radio emitting sources imaged with the e-EVN (upper panel) and e-MERLIN (lower panel) arrays. *Columns*: (1) Source names corresponding to those in Figure VI.2. (2–3) Coordinates given with respect to $\alpha(J2000) = 13^h20^m35\overset{s}{.}0$ and $\delta(J2000) = 34°08'22\overset{''}{.}0$. Position uncertainties in mas, within parentheses, are given by FWHM/($2 \times SNR$), where SNR is the signal to noise ratio, and FWHM was taken as the projection of the beam major axis on both α and δ axes. The thermal rms is 57 and 95 μJy/beam in the e-EVN and in the e-MERLIN image, respectively. (4) Measured flux density (also corresponding to the peak intensities). We estimated the uncertainties by adding in quadrature the rms noise in the map plus a 5% uncertainty in the point source flux density calibration. (5) Monochromatic luminosity at the observed frequency ($\nu = 5\,$GHz for the e-EVN, and $\nu = 6.9\,$GHz for e-MERLIN). (6) Deconvolved major and minor axes, obtained by fitting a Gaussian to each source. (7) Brightness temperature lower limits. For most of the sources it was not possible to obtain deconvolved sizes, therefore we have used instead the solid angle subtended by the synthesised beam, for calculating lower limits of T_B in all cases, i.e., $\Omega_s = \pi(4\log2)^{-1}$ (FWHM$_M \times$ FWHM$_m$), with FWHM$_M$ and FWHM$_m$, the major and minor synthesised beam fitted FWHM, respectively ($10.5 \times 8.6\,$mas^2 for the e-EVN, and $188 \times 93\,$mas^2 for e-MERLIN). (8) Projected distance from each component to the strongest source in each map (A5 for the e-EVN image, and A for e-MERLIN).

Source name	$\Delta\alpha$(J2000)	$\Delta\delta$(J2000)	S_ν (mJy)	L_ν (10^{27} erg s^{-1} Hz^{-1})	$\Theta_M \times \Theta_m$ (mas^2)	$\log T_B >$ (K)	D_{sc} (pc)
A1	0.3230 (0.9)	0.337 (0.2)	0.33 ± 0.06	3.97 ± 0.71	$5.4 \times \cdots$	5.17 ± 0.08	28
A2	0.3204 (0.6)	0.375 (0.1)	0.45 ± 0.06	5.43 ± 0.73	$7.0 \times \cdots$	5.31 ± 0.06	16
A3	0.3203 (0.6)	0.312 (0.1)	0.48 ± 0.06	5.76 ± 0.74	$7.5 \times \cdots$	5.33 ± 0.06	22
A4	0.3194 (0.5)	0.367 (0.1)	0.62 ± 0.06	7.47 ± 0.78	11.6×3.2	5.44 ± 0.05	9
A5	0.3186 (0.1)	0.352 ($\sim$0.0)	3.58 ± 0.19	42.87 ± 2.25	$\cdots \times \cdots$	6.20 ± 0.02	0
A6	0.3168 (0.7)	0.350 (0.1)	0.42 ± 0.06	5.07 ± 0.73	$6.1 \times \cdots$	5.28 ± 0.06	11
A	0.319 ($<$1)	0.35 (2)	3.82 ± 0.21	45.73 ± 2.55	$99.8 \times \cdots$	3.45 ± 0.02	0
B1a	0.336 (1)	0.09 (6)	1.36 ± 0.12	16.22 ± 1.40	99.2×63.1	3.00 ± 0.04	159
B1b	0.301 (2)	0.56 (10)	0.84 ± 0.10	10.00 ± 1.24	180.5×77.4	2.79 ± 0.05	150
B2a	0.360 (2)	0.69 (8)	1.06 ± 0.11	12.73 ± 1.30	152.2×74.9	2.89 ± 0.04	404
B2b	0.282 (6)	0.00 (28)	0.31 ± 0.10	3.75 ± 1.15	$77.6 \times \cdots$	2.36 ± 0.13	388
C	0.381 (4)	0.23 (18)	0.49 ± 0.10	5.81 ± 1.17	$78.2 \times \cdots$	2.55 ± 0.09	377

them (A5) being approximately 10 times more luminous than the remainder (see upper panel in Table VI.1). The high brightness temperatures and high luminosities of sources A1–A6, suggest a non-thermal origin for all of them.

The brightest component in our e-MERLIN image (A) has a peak intensity similar to that of A5 and their positions are highly coincident (despite of the use of different phase reference sources). Hence, A5 must be the main powering source for the radio emission of component A. In fact, Smith *et al.* (1998a) and Parra *et al.* (2010) have found evidence of compact AGN activity through VLBI studies, which we identify here as component A5.

Further evidence for an obscured AGN in IC 883 can be inferred from the ratio of radio to hard X-ray luminosity ($R_{\mathrm{X}} = \nu L_\nu(5\,\mathrm{GHz})/L_{\mathrm{HX}}$; Terashima and Wilson, 2003). Iwasawa *et al.* (2011) report a hard X-ray luminosity ($L_{\mathrm{HX}} = L[2\text{–}10\,\mathrm{keV}]$) of 6.4×10^{40} erg s^{-1} for IC 883. Considering the luminosity at 5 GHz of A5 (see Table VI.1), we calculate $R_{\mathrm{X}} \approx 3.4\times10^{-3}$, which is consistent with a LLAGN, as inferred from figure 4 of Terashima and Wilson (2003).

With the identification of A5 as an AGN, the rest of the non-thermal compact sources in the nucleus likely make IC 883 a new supernova factory, one of the few imaged so far with VLBI, e.g., Arp 220 and Arp 299-A (Batejat *et al.*, 2011; Pérez-Torres *et al.*, 2009b, and references therein). The composite starburst-AGN nature of IC 883, revealed previously by optical spectroscopy (see e.g., Yuan *et al.*, 2010), is now supported by our VLBI studies for the first time. Recently approved EVN observations at different frequencies will allow unequivocally the characterisation of each one of the mas compact components.

The e-MERLIN image reveals a structure with an approximate extent of 1.9 arcsec ($\lesssim$ 1 kpc), at a position angle of 144°(Figure VI.2). This inclination matches that previously found in other radio (e.g., Condon *et al.*, 1991; Parra *et al.*, 2010) and NIR studies (e.g., Smith *et al.*, 1995). The NIR elongated structure is thought to be the disk of IC 883 (Scoville *et al.*, 2000). However, a study of the molecular and atomic gas towards IC 883 carried out by Clemens and Alexander (2004), favours the presence of a dusty rotating ring (from South-East towards North-West) rather than a disk. In this scenario, component A, dominated by a LLAGN, would be at the centre of the ring, whereas B1a, B2a (approaching components) and B1b, B2b (receding components) would be part of the ring itself. B2b is only a 3σ source, but in light of the results by Clemens and Alexander (2004), it is likely a high-velocity component of the rotating ring.

From the values in Table VI.1, we note that the approaching components (B1a and B2a) have a slightly larger flux than the receding components (B1b and B2b), and are also placed slightly farther away from A. We also note that B1a-B1b and B2a-B2b do not lie on the same line that joins them to component A. This is evidence of the ring being warped,

probably due to the interaction with the dense ISM.

VI.2.2   The radio quiet SNe 2010cu and 2011xx

There are no radio sources detected with the e-EVN above 3σ at/around the reported positions for either SN 2010cu, or SN 2011xx. Therefore, the 3σ upper limit for both SNe at 5 GHz corresponds approximately to 2×10^{27} erg s^{-1} Hz^{-1}.

SN 2010cu, discovered in February 2010 at NIR wavelengths, has been found to be consistent with a CCSN (Ryder *et al.*, 2010a). If this SN is a type II, its non-detection at 5 GHz is likely to be an indication of the following scenarios: i) the radio emission at 5 GHz has entered the optically thin part of its evolution, now having a luminosity well below 2×10^{27} erg s^{-1} Hz^{-1}, and/or, ii) this SN is intrinsically fainter than other well known RSNe at their maximum radio brightness (e.g., SN 1979C). SN 2010cu is also not detected in our e-MERLIN observations, supporting the same scenarios.

SN 2011xx, discovered in February 2011 at NIR wavelengths, was also not detected in our 6.9 GHz e-MERLIN observations. We detect a $\sim 5.2\sigma$ source (C) close to the position of SN 2011xx reported in Kankare *et al.* (2011b), however these are not coincident according to the revised astrometry of the NIR images (Kankare *et al.*, 2011a).

The radio non-detection of SN 2011xx a few months after its explosion is consistent with the following scenarios (see e.g., figure 2 in Chevalier *et al.*, 2006): i) if SN 2011xx is a type Ib/c SN, it became radio faint on very short time scales (a few months at most); ; ii) alternatively, if it is a Type II SN the radio emission of SN 2011xx at both 5 and 6.9 GHz is still optically thick, iii) being a type II, SN 2011xx is intrinsically a low-luminosity radio supernova (e.g. a type IIP such as SN 1999em) and thus more sensitive observations are required for its detection. Note that the occurrence of SN 2011xx outside the dusty ring (see Figure VI.2), explains its estimated extremely low-extinction (Kankare *et al.*, 2011a).

CHAPTER VII

CONCLUSIONS & PROSPECTIVES

The work presented in this thesis deals with the study of luminous (LIRGs: $L_{\rm IR} >$ 10^{11} $L_\odot$) and ultra luminous (ULIRGs: $L_{\rm IR} > 10^{12}$ $L_\odot$) infrared galaxies. We have exploited the capabilities of current instruments to obtain high angular resolution, high sensitivity radio observations. Our studies have yielded important results which contribute significantly to the general knowledge of (U)LIRGs.

Radio observations towards nearby galaxies profit from the high angular resolution provided by interferometric techniques. We have studied the early merger system Arp 299 ($L_{\rm IR} \approx 6.7 \times 10^{11}$ $L_\odot$ at 44.8 Mpc), whose brightest nucleus (Arp 299-A=IC 694) is revealed in our observations as a very prolific SN factory. Within the 150 pc diameter innermost region, we found a rich cluster of 26 compact radio emitting sources, most of them young RSNe and SNRs. The luminosities for the SN candidates, range between $\approx 3 \times 10^{26}$ and $\approx 2 \times 10^{27}$ erg s^{-1} Hz^{-1} (typical of type IIb, IIP and IIL SNe). A LLAGN is found in coexistence with the intense starburst in Arp 299-A, and in fact, the star formation activity is dominating over the AGN activity in this nucleus. Regarding its $L_{\rm IR}$, Arp 299 is placed half-way between the starburst galaxy M82 (3.6×10^{10} $L_\odot$ at 3.6 Mpc) and the ULIRG Arp 220 (1.6×10^{12} $L_\odot$ at 79.9 Mpc), and so it is its star formation activity. These were, until very recently, the only known cases in the literature where a starburst could be directly mapped with high angular resolution radio observations, and thus represented unique cases to study the star formation properties in extreme environments.

We have also discovered a new likely case of a LIRG in the local Universe hosting a SN factory: IC 883 (4.7×10^{11} $L_\odot$ at 100 Mpc). Our observations reveal the presence of at least six non-thermal compact components within the innermost 100 pc diameter region. This galaxy, being less luminous but farther away than Arp 299 and in a much more advanced merger stage, contains also a LLAGN, which seems to be powering the radio luminosity in this LIRG. Our results suggest that both the merger stage and the infrared luminosity are the main ingredients to distinguish the dominant mechanism of energy in LIRGs. In fact, this picture for LIRGs matches with the evolutionary scenario proposed by Yuan *et al.*

(2010), in which ULIRGs are dominated by starburst activity at an early merger stage; at intermediate stages, ULIRGs would be powered by a composite of starburst-AGN activity; and finally, at later stages, an AGN would dominate the emission.

At a larger distance (252 Mpc) we have studied the radio emission at galactic, circumnuclear and nuclear scales of the ULIRG IRAS 23365+3604 (1.4×10^{12} L$_\odot$). The direct detection of a starburst and/or an AGN in this galaxy has proved to be very challenging, even at the high angular resolution provided by current instruments. We then used different indicators to unveil the nature of this source, such as its morphology, spectral index and magnetic field. We found that the nuclear region has a composite nature: starburst and/or an AGN in the innermost 100 pc region, and clumps of SNRs in the outskirts of the nucleus. The equivalent magnetic field strength at galactic (mapped with the VLA) and nuclear scales (mapped with the EVN), 18 and 175 μG, respectively, correspond to that of a galaxy in an advanced stage of interaction (e.g., Drzazga et al., 2011; Momjian et al., 2003). Radiative losses are important, so re-acceleration and/or replenishment of new electrons is necessary. The SNe and SNRs, for which we have found evidence, are likely providing the mechanism of re-acceleration, or replenishment of new electrons that is needed to halt the radio energy depletion. Our study of IRAS 23365+3604 (at $z \sim 0.06$) has shown that high angular resolution, high sensitivity observations are needed if we intend to make a significant improvement in the detailed understanding of nuclear and circumnuclear starbursts in the local Universe. At higher redshifts it will not be possible to resolve individual compact sources (e.g., SNe, SNRs, AGN) from each other, within the nuclear region of (U)LIRGs; yet, we could infer the activity of such compact sources, by carefully monitoring variations of the total flux density and spectral index distribution.

We have tested a technique on Arp 299 to indirectly detect SN activity through the monitoring of radio flux density variations. We have been able to estimate a RSN rate for the nucleus B1 in Arp 299 of $> 0.28^{+0.27}_{-0.15}$ yr^{-1}, from the indirect detection of three SNe. This estimate is in good agreement with the IR luminosity-based SN rate estimate, and also with values obtained with other methods at radio wavelengths. The technique is somehow limited by the background emission of the galaxy itself, as well as by the sensitivity of the instrument used. Nevertheless, this technique offers the opportunity to study the SFR in CCSN host galaxies which cannot be resolved with the current achievable resolution (milliarcsec), such as in the case of IRAS 23365+3604.

Our work has emphasized the importance of extinction-free measurements of the SN activity within the innermost nuclear regions of (U)LIRGs. The detection of SNe in the innermost nuclear regions of (U)LIRGs with optical and NIR studies is not possible due to the high extinction therein and the lack of sufficient angular resolution. We have shown that at radio frequencies, with relatively high angular resolution, it is possible to detect

SNe buried deep in LIRG nuclei. This is of great relevance for determining the complete CCSN rates in local LIRGs and also for interpreting the result of the CCSN searches at higher redshifts used to trace the star formation rates as a function of redshift. Upcoming facilities such as Square Kilometre Array (SKA) will allow us to obtain an unprecedented high sensitivity, and thus will be of great use to study the SFR at higher redshifts.

For galaxies in which the highest resolution observations are able to resolve out their diffuse emission, thus revealing compact sources (e.g., AGN, SNe and SNRs), high sensitivity is a priority. High angular resolution, low sensitivity observations have been used in previous studies to infer AGN activity in a number of (U)LIRGs. However, only the identification of both SF and AGN activity can provide us with an understanding of the starburst-AGN connection in (U)LIRGs.

The work presented in this thesis will continue with the termination of the project presented in Chapter V (halted due to the difficulty of the data reduction). Although the sample is small, we would possibly be able to draw some general properties, for example, regarding the energy depletion, composite nature, etc., in the extreme environment of (U)LIRGs. VLBI observations are expensive and thus, it is not feasible to devote great amounts of time to study in detail a large sample of galaxies. The study of statistically significant samples of nearby starburst galaxies in moderate amounts of time will be soon possible with the advent of e-MERLIN, which is now a reality (see the results for IC 883 in Chapter VI of this thesis). The e-MERLIN legacy project entitled "Luminous Infrared Galaxy Inventory" (LIRGI; PIs: John Conway & M. A. Pérez-Torres), pursues the ambitious goal of characterising the nuclear and circumnuclear radio emission of 42 of the most luminous northern (U)LIRGs up to a distance of 260 Mpc, with angular resolution of 50 mas at 6 cm (linear resolution of 25 pc for a distance of 100 Mpc). This project, in which I am a collaborator, will contribute to the understanding of the physics of these local objects, while giving new light to studies aiming at tracing the star formation history of the Universe at higher redshifts.

Publications included in this thesis

The results of the thesis have been included in their majority in four publications. In the following I present the conclusions and discussions of each paper and describe my contributions to each publication.

Paper I - **"An extremely prolific supernova factory in the buried nucleus of the starburst galaxy IC 694" by Pérez-Torres, M. A., Romero-Cañizales, C., Alberdi, A. & Polatidis, A. 2009b**, *A&A* **507, L17.**

e-EVN observations show that Arp 299-A hosts an extremely prolific supernova factory, with radio luminosities typical of Type IIb, IIP, and IIL. We find evidence for at least three slowly-evolving, long-lasting, non-standard RSNe, thus indicating that the local CSM conditions are playing a main role in determining the radio behaviour of the exploding SNe. Our current monitoring of Arp 299-A with the e-EVN at 5 GHz, which is scheduled to continue until the end of 2010, should allow us to detect any new RSN and to monitor the flux density evolution of those already detected. We will be able to test whether the IMF in Arp 299-A is top-heavy, in contrast with the normally assumed Salpeter (Salpeter, 1955), or Kroupa (Kroupa, 2001) IMFs, where the production of massive stars ($M \gtrsim 8$ M$_\odot$) that eventually result in CCSNe is low compared to the production of less massive stars. There seems to be evidence that this might also be the case of M 82 (Doane and Mathews, 1993) and Arp 220 (Parra *et al.*, 2007). Theoretically it is expected that in the warm, dense, ISM conditions within a (U)LIRG, the IMF should indeed be top-heavy because of a higher Jeans mass (Klessen *et al.*, 2007).

Paper II - **"The core-collapse supernova rate in Arp 299 revisited", by Romero-Cañizales, C., Mattila, S., Alberdi, A., Pérez-Torres, M. A., Kankare, E. & Ryder, S. D., 2011**, *MNRAS* **415, 2688.**

We have used VLA archival data to estimate the radio SN rate in the nearby LIRG Arp 299. The wealth of data available for Arp 299 in the VLA archive, makes this galaxy a unique target to perform such studies.

We have used the variability of the nuclear radio flux density to probe the RSN activity

103

in the absence of high angular resolution VLBI observations. The radio flux densities of the nuclei A and B1 within Arp 299, result from the contribution of several compact sources located in the innermost nuclear regions, along with diffuse emission. In the case of nucleus A, the diffuse emission is dominant and we see that its flux density remains constant within the observational uncertainties throughout the time interval we have studied here. This is consistent with Ulvestad (2009) claim that for this nucleus, the integrated flux density of the compact sources within the nucleus, is only about 20% of the total flux density seen at lower resolution. The rest is diffuse emission, mainly synchrotron, of the galaxy itself.

In the B1-nucleus, small variations in flux density due to new SNe can be distinguished from the total nuclear flux density at VLA resolution. In fact, the SNe can even dominate it, as seen in the case of the 2005 event. We have been able to indirectly detect three radio luminous SNe within the B1-nucleus, thus estimating a radio SN rate for B1 of $\nu_{\mathrm{SN}} > 0.28^{+0.27}_{-0.15} \, \mathrm{yr}^{-1}$. This estimate is in good agreement with the IR luminosity-based SN rate estimate, and also with values obtained with other methods at radio wavelengths. The remarkable difference between our estimate and those obtained in other studies is that here, we have estimated the SN rate by directly identifying the RSN activity within the B1-nucleus, which is only possible at radio wavelengths. Note that the fact that any putative AGN is extremely weak (as suggested by VLBI observations), allow us to interpret flux density variations as being due to (recently) exploded SNe and marginally trace their light curve evolution.

Although our flux density variation method is not very sensitive in the case of bright nucleus such as Arp 299-A, where the diffuse emission dominates the overall radio flux density, it is well suited to be applied to sources like Arp 299-B1, which at a distance of $44.8 \, \mathrm{Mpc}$ has a luminosity around $2.4 \times 10^{28} \, \mathrm{erg \, s^{-1} \, Hz^{-1}}$, thus being bright enough to provide a high RSN rate, but faint enough to enable their detection through flux density variations.

The detection of new SNe in Arp 299-A through this method (based on VLA measurements) is a challenging task: i) given the expected IR luminosity based SN rate, a fine sampling of the light curve is needed; ii) due to the brightness of the nucleus, new RSNe should have $L_{\mathrm{peak}} > 3.1 \times 10^{28} \, \mathrm{erg \, s^{-1} \, Hz^{-1}}$ to become 5σ detections.

Moreover, in the case of the A-nucleus, the expected typical RSN flux densities are comparable with the uncertainties in the total flux density of the nuclear region, making the SN detection impossible, unless very bright SNe (such as powerful type IIn or 1998bw-like events) occur. To overcome this situation, we have also tested the possibility of using high angular resolution NIR AO observations for the detection of SNe within the innermost nuclear regions of Arp 299-A. However, we were unable to detect any new SNe. Our estimated limiting magnitude for the SN detection at $\sim 300 \, \mathrm{mas}$ (or $70 \, \mathrm{pc}$ projected

distance) from the centre of the nucleus A would allow the detection of typical CCSNe suffering from extinctions of A_V up to ~ 15 mag. At a larger offset from the nucleus (of 1 arcsec, or 200 pc projected distance) our observations were sensitive to typical CCSNe with A_V up to ~ 30 mag.

The VLA epochs included in our sample were observed for different purposes and thus have different quality (i.e., sensitivity and resolution). Hence, a variability test that yields proper SN identifications through a correct light curve sampling has not been possible. The ideal case would be to have a specific observing program which provides homogeneity in the observed frequency, resolution, and a regular time span between observations of the same source. The EVLA represents a very good instrument to achieve these goals. However, its changing configuration represents a changing angular resolution with time, and thus a finer sampling that allows the identification of type Ib/c SNe is again compromised. The upcoming e-MERLIN, with a very high sensitivity and resolution, provides the best option to carry out this kind of studies.

PAPER III - **"EVN observations of the farthest and brightest ULIRGs in the local Universe: the case of IRAS 23365+3604", by Romero-Cañizales, C., Pérez-Torres, M. A. & Alberdi, A. 2011, submitted to** *MNRAS*.

We have presented state-of-the-art radio interferometric images of IRAS 23365, one of the brightest and farthest ULIRGs in the local Universe ($z < 0.1$).

Our images reveal the presence of a nuclear region, possibly a starburst-AGN composite, with an approximate size of 200 pc in L-band, and about 100 pc in C-band. We find that the L- and C-band radio emission peak at different positions, thus suggesting that the nuclear region is composed of at least two different emitting regions, dominated by distinct populations of radio emitters.

In the region where the L- and C-band emission overlap, there is evidence for ongoing non-thermal activity, characterised by very energetic, short-lived particles . During our EVN monitoring of IRAS 23365, we have found flux density variability in the overlapping region, thus resulting in a variation of the spectral index. This can be explained by the flux density variations of sources therein (SNe, AGN, etc.) and/or by the appearance of new sources (e.g., SNe) which would be seen first at higher frequencies and later at lower frequencies (Weiler *et al.*, 2002). The edges of the overlapping region characterised by less energetic, long-lived particles, would be dominated by an old population of radio emitters, probably clumps of SNRs, for which we have found two candidates in one of our L-band EVN epochs. These facts agree with the classification of IRAS 23365 as a composite system, made by Yuan *et al.* (2010).

The radio source lifetime at different scales (as seen with the VLA, MERLIN and the EVN arrays) and at both L- and C-bands, is limited by Compton losses. The SNe and SNRs, for which we have found evidence, are likely providing the mechanism of re-acceleration, or replenishment of new electrons that is needed to halt the radio energy depletion.

We have found that the equivalent magnetic field strength at galactic (mapped with the VLA) and nuclear scales (mapped with the EVN), 18 and $175\,\mu$G, respectively, correspond to that of a galaxy in an advanced stage of interaction (Drzazga $et\ al.$, 2011; Momjian $et\ al.$, 2003). The magnetic field in both nuclear and circumnuclear regions is stronger than at galactic scales, thus implying that the lifetime of the electrons undergoing synchrotron losses is shorter ($\lesssim 1\,$Myr) in the innermost nuclear regions (with linear size $R \lesssim 0.5\,$kpc) of IRAS 23365, and larger ($\gtrsim 1\,$Myr) in the outer regions ($R \gtrsim 4\,$kpc).

Our study of IRAS 23365 (at $z \sim 0.06$) has shown that high angular resolution, high sensitivity observations are needed if we intend to make a significant improvement in the detailed understanding of nuclear and circumnuclear starbursts in the local Universe. The resolution we attained using a maximum baseline length of approximately 7,000 km, is not enough to resolve individual compact sources (e.g., SNe, SNRs, AGN) from each other, within the nuclear region of IRAS 23365; yet, it could be possible to infer the activity of such compact sources, by carefully monitoring variations of the total flux density and spectral index distribution. In the case of IRAS 23365, where a large number of SNe are expected each year, several observations per year would be needed to perform such an indirect study of the SN population in its nuclear region, provided that we are able to distinguish between AGN outbursts and SN explosions.

IRAS 23365 is a good example of the situation to be faced when observing galaxies at higher redshifts. It is expected that the SKA, with a maximum baseline length $\approx 3,000\,$km, will allow the detection of sources as faint as 50 nJy, e.g. CCSNe, exploding at $z \sim 5$ (see e.g., Lien $et\ al.$, 2011). However, the angular resolution will be a strong limiting factor. In those cases where the nuclear and even the circumnuclear regions (i.e., where we expect most of the SN activity to occur) of the host galaxy cannot be resolved out into their different components, SKA's high sensitivity might be of great use to indirectly detect SN activity through the monitoring of flux density variations.

PAPER IV - "**The starburst-AGN nucleus in the luminous infrared galaxy IC 883: A new supernova factory revealed by e-EVN observations**", by Romero-Cañizales, C., Pérez-Torres, M. A., Alberdi, A., Argo, M. K., Beswick, R. J., Efstathiou, A., Garrington, S. T., Kankare, E., Mattila, S., Muxlow, T. W. B., Ryder, S. D. & Väisänen, P. 2011, submitted to *A&A* letters

We have imaged the nuclear and circumnuclear regions of the LIRG IC 883 at radio wavelengths. Our e-EVN observations reveal the presence of at least six non-thermal compact components, likely constituting a supernova factory in coexistence with a LLAGN, like the case in Arp 299-A, where the long-sought AGN, also a low-luminosity one, was embedded within the nuclear starburst. In view of the very few radio SN factories discovered in the local Universe (M82, Arp 299 and Arp 220) the addition of a new factory for future detailed studies at high angular resolution is of much relevance.

Our e-MERLIN observations evidence the presence of a warped ring structure in the innermost regions of the LIRG IC 883, in agreement with previous studies on the interstellar medium of this galaxy. The source we identify with the LLAGN is powering the radio emission in IC 883, and yet, as observed at both radio and NIR wavelengths, this LIRG displays very active star formation. None of the SNe detected at NIR wavelengths within the last year are detected in our radio observations.

My contribution to the publications included in this thesis

For **Paper I**, I was responsible of the schedule preparation, data reduction, and the writing of parts of the Appendix. I also participated in the discussions. For **Paper II**, I was responsible of the radio data reduction and analysis, the data reduction and astrometry of the NIR images, and the writing of the manuscript. For **Paper III**, I was responsible of the preparation of the schedule of the EVN observations, data reduction and analysis, and the writing of the manuscript. For **Paper IV**, I was responsible of writing the proposals to obtain observing time, as well as for the data reduction and analysis and the writing of the manuscript.

Additional publications

As a part of my PhD training, I have also contributed to two publications which are not included in this thesis, but whose results are mentioned.

- "Discovery of a very highly extinguished supernova in a luminous infrared galaxy", by Kankare, E., Mattila, S., Ryder, S. D., Pérez-Torres, M. A., Alberdi, A., Romero-Cañizales, C., Díaz-Santos, T. Väisänen, P., Efstathiou, A., Alonso-Herrero, A. Colina, L., & Kotilainen, J. 2008, *ApJ* 689, L97. For this paper I was responsible for reducing the radio data and participated in the discussion of the results.

- "Serendipitous discovery of the long-sought active galactic nucleus in Arp 299-A", by Pérez-Torres, M. A., Alberdi, A., Romero-Cañizales, C. & Bondi, M., 2010, *A&A* 519, L5+. For this paper I was responsible for double-checking every estimate and participated actively in the scientific discussions.

Appendix A

Radiative transfer

In this appendix, I show a formulation of the radiative transport equation (RTE), which is important for understanding the propagation of radio waves.

A.1   Intensity

The intensity of the radiation (I_ν) emitted by a source in thermodynamic equilibrium is given by the Planck's law for a blackbody,

$$I_\nu = \frac{2h\nu^3}{c^2} \frac{1}{e^{h\nu/kT} - 1} \quad (\,\mathrm{erg\,s^{-1}\,cm^{-2}\,sr^{-1}\,Hz^{-1}}).$$

Such situation does not hold in general, but we can always define a temperature that depends on the frequency, so that the intensity can still be written in terms of the Planck's law, i.e., defining a situation of local thermodynamic equilibrium (LTE). Then,

$$I_\nu = \frac{2h\nu^3}{c^2} \frac{1}{e^{h\nu/kT_\mathrm{B}} - 1} \tag{A.1}$$

where T_B[1] is the brightness temperature, dependent on frequency.

At radio frequencies, the Rayleigh−Jeans approximation ($h\nu \ll kT$) is valid, therefore,

$$e^{h\nu/kT} = \sum_{n=1}^{\infty} \frac{(h\nu/kT)^n}{n!} \simeq 1 + \frac{h\nu}{kT} \ .$$

---

[1]The brightness temperature is also called radiation temperature, T_R, when the Rayleigh-Jeans approximation holds.

Using this approximation in Eq. A.1, we have

$$I_\nu = \frac{2h\nu^3}{c^2} \frac{1}{e^{h\nu/kT_{\mathrm{B}}} - 1} \simeq \frac{2h\nu^3}{c^2} \frac{1}{1 + h\nu/kT_{\mathrm{B}} - 1} = \frac{2h\nu^3}{c^2} \frac{1}{h\nu/kT_{\mathrm{B}}}$$

$$\Rightarrow \quad I_\nu = \frac{2\nu^2}{c^2} kT_{\mathrm{B}} \ , \tag{A.2}$$

which I will be using along this thesis (see also Appendix B).

A.2 Radiative Transport Equation

The radiation from an emitting source interacts with the matter that encounters in its way to the observer. To account for the variation of the intensity per unit length, l, we consider two phenomena: the attenuation due to the absorption of radiation by the traversed matter, and the intensity that the same absorbing matter will generate. These situations are described by the absorption coefficient κ_ν (attenuation per unit length at the frequency ν) and the emission coefficient j_ν (generated intensity per unit length). Hence, the variation in intensity is described by the following equation

$$\frac{dI_\nu}{dl} = -\kappa_\nu I_\nu + j_\nu$$

which is known as the RTE.

It is convenient to write this equation in a more practical way. For doing so, let us introduce the quantities $\mathbb{S}_\nu = j_\nu/\kappa_\nu$ and $d\tau_\nu = \kappa_\nu dl$. The former quantity is called the source function, while the latter one is the optical depth, which is a factor related with the background intensity that we can detect.

After these definitions, the RTE can be written as

$$\frac{dI_\nu}{dl} = -\frac{d\tau_\nu}{dl}I_\nu + \mathbb{S}_\nu\frac{d\tau_\nu}{dl}$$

$$\Rightarrow \quad \frac{dI_\nu}{d\tau_\nu} = -I_\nu + \mathbb{S}_\nu \ .$$

We can solve the differential equation, and assuming that the source function is constant within the region traversed by the radiation, we obtain

$$I_\nu(\tau_\nu) = I_\nu(0)e^{-\tau_\nu} + \mathbb{S}_\nu \left(1 - e^{-\tau_\nu}\right) \tag{A.3}$$

which is the best known form of the RTE. Here, the measured intensity is given by $I_\nu(\tau_\nu)$,

the background intensity is given by $I_\nu(0)$, and the attenuation factor is given by $e^{-\tau_\nu}$.

We can write the equation A.3 in terms of temperatures. We define the excitation temperature $(T_{\mathrm{ex}})^2$ as the temperature at which the source function is described by a Planck function. Likewise we did in §A.1, we can express $\mathbb{S}_\nu$ as if it were proportional to T_{ex}, i.e.,

$$\mathbb{S}_\nu = \frac{2\nu^2}{c^2}\, kT_{\mathrm{ex}}$$

and we do something similar for the background intensity if we consider a background temperature, T_{bg}, this is

$$I_\nu(0) = \frac{2\nu^2}{c^2}\, k\, T_{\mathrm{bg}}\ .$$

If we also take into account equation A.2, we can rewrite equation A.3 as

$$T_{\mathrm{B}} = T_{\mathrm{bg}}\, e^{-\tau_\nu} + T_{\mathrm{ex}} \left(1 - e^{-\tau_\nu}\right) \tag{A.4}$$

If $\tau_\nu \ll 1$, the medium is optically thin to the emission observed at the frequency ν, and the background intensity can be observed without attenuation. When $\tau_\nu \gg 1$, the medium is optically thin to the emission observed at the frequency ν, and we lose all the information from the background radiation, because it has been absorbed by the traversed medium, and thus we can only detect the radiation from the outer layers of the intervening matter.

A.3   Line emission

Let us now consider the case of spectral lines. The intensity we observe is given by equation A.3, so we can use I_ν^{obs} instead of I_ν. We know that I_ν^{obs} has a contribution from the line and also from the continuum of the background radiation, given by $I_\nu(0)$. We thus write

$$I_\nu^{\mathrm{obs}} = I_\nu^{\mathrm{L}} + I_\nu(0) \Rightarrow\ \ I_\nu^{\mathrm{L}} = I_\nu^{\mathrm{obs}} - I_\nu(0)\ .$$

Substituting here the expression for I_ν^{obs} given by equation A.3, we have that

$$I_\nu^{\mathrm{L}} = [\mathbb{S}_\nu - I_\nu(0)] \left(1 - e^{-\tau_\nu}\right)\ .$$

We now know that both $\mathbb{S}_\nu$ and $I_\nu(0)$ can be expressed in temperature units, so we

---

[2]Physically, T_{ex} determines the relative population of two energy levels of a system, governed by the Boltzmann distribution of energy.

only need to recognise that the same applies to the line intensity, which can be expressed as a line temperature, T_{L}^0 (where the superscript stands for the value at the centre of the line). This consideration yields a new and more convenient form of the RTE given by

$$T_{\mathrm{L}}^0 = (T_{\mathrm{ex}} - T_{\mathrm{bg}}) \left(1 - e^{-\tau_0}\right) \tag{A.5}$$

Appendix B

Brightness temperature: some approximations

When observing a radiation source, the telescope intercepts the intensity that comes from a solid angle (Ω) subtended by the source, such that the measured flux density is the following,

$$S_\nu \propto I_\nu \, \Omega$$

$$\Rightarrow \quad T \approx \frac{c^2}{2k\nu^2} \frac{S_\nu}{\Omega}, \tag{B.1}$$

following equation A.2. The energy density per unit frequency, per unit intercepting area, per unit integration time (S_ν), is measured in jansky units ($1\,\mathrm{Jy} = 10^{-23}\ \mathrm{erg\,s^{-1}\,cm^{-2}\,Hz^{-1}}$) for convenience.

In the literature, we can find different approximations for Ω. Here I show the one I use throughout this thesis, which is based on the assumption of a Gaussian shape for a brightness distribution $B(l,m)$ of the radiation (with l and m, the direction cosines). In this case, we have,

$$\Omega = \int_{m=-\infty}^{\infty} \int_{l=-\infty}^{\infty} B(l,m)\,\mathrm{d}l\,\mathrm{d}m = \int_{m=-\infty}^{\infty} \int_{l=-\infty}^{\infty} \exp\left[-\left(\frac{l^2}{2\sigma_x^2} + \frac{m^2}{2\sigma_y^2}\right)\right]\,\mathrm{d}l\,\mathrm{d}m.$$

To solve this, let

$$x = \frac{l}{\sqrt{2}\sigma_x} \quad \Rightarrow \quad \mathrm{d}l = \sqrt{2}\sigma_x\,\mathrm{d}x, \quad \text{and}$$

$$y = \frac{m}{\sqrt{2}\sigma_y} \quad \Rightarrow \quad \mathrm{d}m = \sqrt{2}\sigma_y\,\mathrm{d}y.$$

Thus,

$$\Omega = \sqrt{2}\sigma_x\sqrt{2}\sigma_y \int_{x=-\infty}^{\infty} \int_{y=-\infty}^{\infty} \exp\left[-\left(x^2 + y^2\right)\right]\,\mathrm{d}x\,\mathrm{d}y$$

$$\Rightarrow \quad \Omega = 2\,\sigma_x\,\sigma_y \left[2\int_0^{\infty} e^{-x^2}\,\mathrm{d}x\right]\left[2\int_0^{\infty} e^{-y^2}\,\mathrm{d}y\right],$$

113

which can be solved with a change of coordinates. Let

$$x = r \, \cos(\theta) \quad \text{and} \quad y = r \, \sin(\theta)$$

$$\Rightarrow \quad \mathrm{d}x \, \mathrm{d}y = r \, \mathrm{d}r \, \mathrm{d}\theta,$$

then,

$$\Omega = 8 \, \sigma_x \, \sigma_y \int_0^{\pi/2} \int_0^\infty e^{-r^2} r \, \mathrm{d}r \, \mathrm{d}\theta,$$

which can be solved introducing one more change of variables, i.e.,

$$u = -r^2 \quad \Rightarrow \quad \mathrm{d}u = -2 \, r \, \mathrm{d}r,$$

thus resulting in

$$\Omega = 2 \, \pi \, \sigma_x \, \sigma_y.$$

Finally, relating σ_x and σ_y to the FWHM, in both x and y directions, namely Θ_x and Θ_y (or the major and minor axes of a Gaussian), we obtain,

$$\left(\frac{\Omega}{\mathrm{sr}} \right) = \frac{\pi \, \Theta_x \, \Theta_y}{4 \ln 2}, \tag{B.2}$$

We can consider instead the antenna pattern, $P(l, m)$, which is sensitive to only a small region in the sky. In that case, we would be solving for an approximation of the subtended solid angle of the beam, at the coordinates where the radiation source is placed.

B.1 Different forms of the brightness temperature

Using equation B.1, we can define the main beam brightness temperature (T_{MB}), as the intensity emitted per time, per bandwidth and per collecting area, measured by the main beam of the antenna pattern, i.e.,

$$T_{\mathrm{MB}} = \frac{c^2}{2k\nu^2} \frac{S_\nu}{\Omega_{\mathrm{MB}}}.$$

Now, if considering Gaussian sources and Gaussian beams, the observed source size (Θ_{obs}) is related to the actual source size (Θ_{s}, also called deconvolved size) and to the beam size (Θ_{b}, given by the main beam' size of the antenna pattern) through,

$$\Theta_{\mathrm{obs}}^2 = \Theta_{\mathrm{s}}^2 + \Theta_{\mathrm{b}}^2$$

(see e.g., Rohlfs and Wilson, 2004).

Then, the brightness temperature we measure, $T_{\rm B}$, is related to $T_{\rm MB}$, through

$$T_{\rm B} = T_{\rm MB}\, \frac{\Omega_{\rm obs}}{\Omega_{\rm s}} = T_{\rm MB}\, \frac{\Theta_{\rm s}^2 + \Theta_{\rm b}^2}{\Theta_{\rm s}^2}$$

From here, we have two possible cases:

i) Unresolved source ($\Theta_{\rm s} < \Theta_{\rm b}$): $\Theta_{\rm obs}^2 \rightsquigarrow \Theta_{\rm b}^2$

$$\Rightarrow T_{\rm B} \simeq T_{\rm MB}\, \frac{\Theta_{\rm b}^2}{\Theta_{\rm s}^2} = T_{\rm s},$$

where $T_{\rm s}$, is the actual source brightness temperature; and

ii) Resolved source ($\Theta_{\rm s} > \Theta_{\rm b}$): $\Theta_{\rm obs}^2 \rightsquigarrow \Theta_{\rm s}^2$

$$\Rightarrow T_{\rm B} \simeq T_{\rm MB}\, \frac{\Theta_{\rm s}^2}{\Theta_{\rm s}^2} = T_{\rm MB}.$$

Making use of equations B.1 and B.2, we have,

$$T_{\rm B} = \frac{c^2}{2k\nu^2}\frac{S_\nu}{\Omega_{\rm s}} \simeq \frac{c^2}{2k\nu^2}\,\frac{4\ln 2}{\pi}\,\frac{S_\nu}{\Theta_{\rm s}^2},$$

for the unresolved case; and,

$$T_{\rm B} = \frac{c^2}{2k\nu^2}\frac{S_\nu}{\Omega_{\rm MB}} \simeq \frac{c^2}{2k\nu^2}\,\frac{4\ln 2}{\pi}\,\frac{S_\nu}{\Theta_{\rm b}^2},$$

for the resolved case.

Should the situation arise in the unresolved case that it is not possible to fit a Gaussian to the emitting source, and hence no deconvolved size can be obtained, we can use $T_{\rm B} \simeq T_{\rm MB}$ as a lower limit for the source brightness temperature.

References

Aalto, S., Radford, S. J. E., Scoville, N. Z. and Sargent, A. I. 1997, Variation of Molecular Line Ratios and Cloud Properties in the ARP 299 Galaxy Merger, *ApJL* **475**, L107+.

Alard, C. and Lupton, R. H. 1998, A Method for Optimal Image Subtraction, *ApJ* **503**, 325.

Alberdi, A., Colina, L., Torrelles, J. M., Panagia, N. *et al.* 2006, Evolution of the Circumnuclear Radio Supernova SN 2000ft in NGC 7469, *ApJ* **638**, 938.

Alonso-Herrero, A., Rieke, G. H., Colina, L., Pereira-Santaella, M. *et al.* 2009, The Extreme Star Formation Activity of Arp 299 Revealed by Spitzer IRS Spectral Mapping, *ApJ* **697**, 660.

Alonso-Herrero, A., Rieke, G. H., Rieke, M. J. and Scoville, N. Z. 2000, Extreme Star Formation in the Interacting Galaxy Arp 299 (IC 694+NGC 3690), *ApJ* **532**, 845.

Anderson, J. P., Habergham, S. M. and James, P. A. 2011, On the multiple supernova population of Arp 299: constraints on progenitor properties and host galaxy star formation characteristics, *MNRAS* **416**, 567.

Baan, W. A. and Haschick, A. 1990, H I absorption and OH emission in IC 694/NGC 3690, *ApJ* **364**, 65.

Baan, W. A. and Klöckner, H.-R. 2006, Radio properties of FIR-megamaser nuclei, *A&A* **449**, 559.

Baars, J. W. M., Genzel, R., Pauliny-Toth, I. I. K. and Witzel, A. 1977, The absolute spectrum of CAS A - an accurate flux density scale and a set of secondary calibrators, *A&A* **61**, 99.

Ballo, L., Braito, V., Della Ceca, R., Maraschi, L. *et al.* 2004, Arp 299: A Second Merging System with Two Active Nuclei?, *ApJ* **600**, 634.

Batejat, F., Conway, J. E., Hurley, R., Parra, R. *et al.* 2011, Resolution of the Compact Radio Continuum Sources in Arp220, *ApJ* **740**, 95.

Berger, E., Kulkarni, S. R. and Chevalier, R. A. 2002, The Radio Evolution of the Ordinary Type Ic Supernova SN 2002ap, *ApJL* **577**, L5.

Bianchi, S., Chiaberge, M., Piconcelli, E., Guainazzi, M. *et al.* 2008, Chandra unveils a binary active galactic nucleus in Mrk 463, *MNRAS* **386**, 105.

Bloom, J. S., Kulkarni, S. R., Harrison, F., Prince, T. *et al.* 1998, Expected Characteristics of the Subclass of Supernova Gamma-Ray Bursts, *ApJL* **506**, L105.

Braatz, J. A. and Gugliucci, N. E. 2008, The Discovery of Water Maser Emission from Eight Nearby Galaxies, *ApJ* **678**, 96.

Braatz, J. A., Wilson, A. S. and Henkel, C. 1996, A Survey for H 2O Megamasers in Active Galactic Nuclei. I. Observations, *ApJS* **106**, 51.

Braatz, J. A., Wilson, A. S. and Henkel, C. 1997, A Survey for H 2O Megamasers in Active Galactic Nuclei. II. A Comparison of Detected and Undetected Galaxies, *ApJS* **110**, 321.

Burke, B. and Graham-Smith, F. 2010, *An introduction to Radio Astronomy*, Cambridge University Press, 3rd ed.

Calzetti, D., Kennicutt, R. C., Engelbracht, C. W., Leitherer, C. *et al.* 2007, The Calibration of Mid-Infrared Star Formation Rate Indicators, *ApJ* **666**, 870.

Caputi, K. I., Lagache, G., Yan, L., Dole, H. *et al.* 2007, The Infrared Luminosity Function of Galaxies at Redshifts z = 1 and z ~ 2 in the GOODS Fields, *ApJ* **660**, 97.

Carilli, C. L. and Taylor, G. B. 2000, The Extreme Compact Starburst in Markarian 273, *ApJL* **532**, L95.

Casoli, F., Willaime, M., Viallefond, F. and Gerin, M. 1999, Molecular gas in the system of merging galaxies ARP 299, *A&A* **346**, 663.

Charmandaris, V., Stacey, G. J. and Gull, G. 2002, Resolving the Buried Starburst in Arp 299, *ApJ* **571**, 282.

Chevalier, R. A. 1982, The radio and X-ray emission from type II supernovae, *ApJ* **259**, 302.

Chevalier, R. A. and Fransson, C. 2001, The Nature of the Compact Supernova Remnants in Starburst Galaxies, *ApJL* **558**, L27.

Chevalier, R. A., Fransson, C. and Nymark, T. K. 2006, Radio and X-Ray Emission as Probes of Type IIP Supernovae and Red Supergiant Mass Loss, *ApJ* **641**, 1029.

Churchwell, E., Witzel, A., Huchtmeier, W., Pauliny-Toth, I. *et al.* 1977, Detection of H2O maser emission in the Galaxy M 33, *A&A* **54**, 969.

Clemens, M. S. and Alexander, P. 2004, A high-resolution study of the interstellar medium in the luminous IRAS galaxy Arp 193, *MNRAS* **350**, 66.

Colina, L., Alberdi, A., Torrelles, J. M., Panagia, N. *et al.* 2001, Discovery of a Bright Radio Supernova in the Circumnuclear Starburst of the Luminous Infrared Seyfert 1 Galaxy NGC 7469, *ApJL* **553**, L19.

Condon, J. J. 1992, Radio emission from normal galaxies, *Annual Review of Astronomy and Astrophysics* **30**, 575.

Condon, J. J., Cotton, W. D., Greisen, E. W., Yin, Q. F. *et al.* 1998, The NRAO VLA Sky Survey, *AJ* **115**, 1693.

Condon, J. J., Helou, G., Sanders, D. B. and Soifer, B. T. 1990, A 1.49 GHz atlas of the IRAS Bright Galaxy Sample, *ApJS* **73**, 359.

Condon, J. J., Helou, G., Sanders, D. B. and Soifer, B. T. 1996, A 1.425 GHz Atlas of the IRAS Bright Galaxy Sample, Part II, *ApJS* **103**, 81.

Condon, J. J., Huang, Z.-P., Yin, Q. F. and Thuan, T. X. 1991, Compact starbursts in ultraluminous infrared galaxies, *ApJ* **378**, 65.

Corbett, E. A., Norris, R. P., Heisler, C. A., Dopita, M. A. *et al.* 2002, First Results from the COLA Project: The Radio-Far-Infrared Correlation and Compact Radio Cores in Southern COLA Galaxies, *ApJ* **564**, 650.

Di Matteo, P., Combes, F., Melchior, A.-L. and Semelin, B. 2007, Star formation efficiency in galaxy interactions and mergers: a statistical study, *A&A* **468**, 61.

Diehl, R., Halloin, H., Kretschmer, K., Lichti, G. G. *et al.* 2006, Radioactive ^{26}Al from massive stars in the Galaxy, *Nature* **439**, 45.

Doane, J. S. and Mathews, W. G. 1993, Stellar Evolution in the Starburst Galaxy M82: Evidence for a Top-heavy Initial Mass Function, *ApJ* **419**, 573.

Drzazga, R. T., Chyży, K. T., Jurusik, W. and Wiórkiewicz, K. 2011, Magnetic field evolution in interacting galaxies, *A&A* **533**, A22+.

Elitzur, M. 1992, *Astronomical Masers*, Kluwer Academic Publishers.

Farrah, D., Afonso, J., Efstathiou, A., Rowan-Robinson, M. *et al.* 2003, Starburst and AGN activity in ultraluminous infrared galaxies, *MNRAS* **343**, 585.

Farrah, D., Rowan-Robinson, M., Oliver, S., Serjeant, S. *et al.* 2001, HST/WFPC2 imaging of the QDOT ultraluminous infrared galaxy sample, *MNRAS* **326**, 1333.

Fixsen, D. J., Cheng, E. S., Gales, J. M., Mather, J. C. *et al.* 1996, The Cosmic Microwave Background Spectrum from the Full COBE FIRAS Data Set, *ApJ* **473**, 576.

Forti, G., Boattini, A., Tombelli, M., Herbst, W. *et al.* 1993, Supernova 1993G in NGC 3690, *IAU Circ.* **5719**, 3.

Gallais, P., Charmandaris, V., Le Floc'h, E., Mirabel, I. F. *et al.* 2004, Dust enshrouded star-forming activity in Arp 299, *A&A* **414**, 845.

Gallimore, J. F., Henkel, C., Baum, S. A., Glass, I. S. *et al.* 2001, The Nature of the Nuclear H_2O Masers of NGC 1068: Reverberation and Evidence for a Rotating Disk Geometry, *ApJ* **556**, 694.

Gehrels, N. 1986, Confidence limits for small numbers of events in astrophysical data, *ApJ* **303**, 336.

González-Martín, O., Masegosa, J., Márquez, I., Guainazzi, M. *et al.* 2009, An X-ray view of 82 LINERs with Chandra and XMM-Newton data, *A&A* **506**, 1107.

Greenhill, L. J. 2007, Masers in AGN environments, in J. M. Chapman & W. A. Baan (editor), *IAU Symposium*, vol. 242 of *IAU Symposium*, pp. 381–390.

Greenhill, L. J., Booth, R. S., Ellingsen, S. P., Herrnstein, J. R. *et al.* 2003, A Warped Accretion Disk and Wide-Angle Outflow in the Inner Parsec of the Circinus Galaxy, *ApJ* **590**, 162.

Hagiwara, Y., Diamond, P. J. and Miyoshi, M. 2002, A search for extragalactic H_2O maser emission towards IRAS galaxies. Detection of a maser from an infrared-luminous merger, NGC 6240, *A&A* **383**, 65.

Heger, A., Fryer, C. L., Woosley, S. E., Langer, N. *et al.* 2003, How Massive Single Stars End Their Life, *ApJ* **591**, 288.

Helou, G., Soifer, B. T. and Rowan-Robinson, M. 1985, Thermal infrared and nonthermal radio - Remarkable correlation in disks of galaxies, *ApJL* **298**, L7.

Henkel, C., Peck, A. B., Tarchi, A., Nagar, N. M. *et al.* 2005, New H2O masers in Seyfert and FIR bright galaxies, *A&A* **436**, 75.

Huang, Z. P., Condon, J. J., Yin, Q. F. and Thuan, T. X. 1990, Probable Radio Supernova in NGC 3690, *IAU Circ.* **4988**, 1.

Imanishi, M. and Nakanishi, K. 2006, Infrared 2-4 Micrometer Spectroscopy and Millimeter Interferometric HCN and HCO$^+$ Observations of the Individual Merging Components of Arp 299, *Publications of the ASJ* **58**, 813.

Iwasawa, K., Sanders, D. B., Teng, S. H., U, V. *et al.* 2011, C-GOALS: Chandra observations of a complete sample of luminous infrared galaxies from the IRAS Revised Bright Galaxy Survey, *A&A* **529**, A106+.

Jha, S., Garnavich, P., Challis, P., Kirshner, R. *et al.* 1999, Supernova 1999D in NGC 3690, *IAU Circ.* **7089**, 2.

Kankare, E., Mattila, S., Ryder, S., Pérez-Torres, M. *et al.* 2008, Discovery of a Very Highly Extinguished Supernova in a Luminous Infrared Galaxy, *ApJL* **689**, L97.

Kankare, E., Mattila, S., Ryder, S. D., Väisänen, P. *et al.* 2011a, Discovery of two concurrent supernovae in the nuclear regions of the luminous infrared galaxy IC 883 (submitted to ApJ).

Kankare, E., Ryder, S. and Mattila, S. 2011b, Possible supernova in IC 883, *The Astronomer's Telegram* **3245**, 1.

Keel, W. C. and Wu, W. 1995, The Local Merger Rate of Disk Galaxies, *AJ* **110**, 129.

Kennicutt, Jr., R. C. 1983, The rate of star formation in normal disk galaxies, *ApJ* **272**, 54.

Kennicutt, Jr., R. C. 1998, Star Formation in Galaxies Along the Hubble Sequence, *Annual Review of Astronomy and Astrophysics* **36**, 189.

Kewley, L. J., Groves, B., Kauffmann, G. and Heckman, T. 2006, The host galaxies and classification of active galactic nuclei, *MNRAS* **372**, 961.

Kewley, L. J., Heisler, C. A., Dopita, M. A., Sutherland, R. *et al.* 2000, Compact Radio Emission from Warm Infrared Galaxies, *ApJ* **530**, 704.

Klaas, U. and Elsaesser, H. 1991, Optical structure of infrared-luminous galaxies, *A&AS* **90**, 33.

Klessen, R. S., Spaans, M. and Jappsen, A.-K. 2007, The stellar mass spectrum in warm and dusty gas: deviations from Salpeter in the Galactic centre and in circumnuclear starburst regions, *MNRAS* **374**, L29.

Komossa, S., Burwitz, V., Hasinger, G., Predehl, P. *et al.* 2003, Discovery of a Binary Active Galactic Nucleus in the Ultraluminous Infrared Galaxy NGC 6240 Using Chandra, *ApJL* **582**, L15.

Kraus, A. 2009, *Calibration of the Effelsberg 100m telescope*.

Kroupa, P. 2001, On the variation of the initial mass function, *MNRAS* **322**, 231.

Lai, O., Rouan, D., Rigaut, F., Doyon, R. *et al.* 1999, Adaptive optics observations of luminous infrared galaxies. II. Imaging of the merging galaxy Arp 299, *A&A* **351**, 834.

Le Floc'h, E., Papovich, C., Dole, H., Bell, E. F. *et al.* 2005, Infrared Luminosity Functions from the Chandra Deep Field-South: The Spitzer View on the History of Dusty Star Formation at $0 \lesssim z \lesssim 1$, *ApJ* **632**, 169.

Leonard, D. C. and Cenko, S. B. 2005, Type Refinement for SN 2005U in Arp 299, *The Astronomer's Telegram* **431**, 1.

Li, W., Leaman, J., Chornock, R., Filippenko, A. V. *et al.* 2011, Nearby supernova rates from the Lick Observatory Supernova Search - II. The observed luminosity functions and fractions of supernovae in a complete sample, *MNRAS* **412**, 1441.

Li, W., Li, C., Wan, Z., Filippenko, A. V. *et al.* 1998, Supernova 1998T in IC 694, *IAU Circ.* **6830**, 1.

Lien, A., Chakraborty, N., Fields, B. D. and Kemball, A. 2011, Radio Supernovae in the Great Survey Era, *ApJ* **740**, 23.

Lilly, S. J., Eales, S. A., Gear, W. K. P., Hammer, F. *et al.* 1999, The Canada-United Kingdom Deep Submillimeter Survey. II. First Identifications, Redshifts, and Implications for Galaxy Evolution, *ApJ* **518**, 641.

Lo, K. Y. 2005, Mega-Masers and Galaxies, *Annual Review of Astronomy and Astrophysics* **43**, 625.

Lonsdale, C. J., Diamond, P. J., Thrall, H., Smith, H. E. *et al.* 2006, VLBI Images of 49 Radio Supernovae in Arp 220, *ApJ* **647**, 185.

Lonsdale, C. J., Lonsdale, C. J., Smith, H. E. and Diamond, P. J. 2003, VLBI Imaging of Luminous Infrared Galaxies: Active Galactic Nucleus Cores in Markarian 231, UGC 5101, and NGC 7469, *ApJ* **592**, 804.

Madau, P., della Valle, M. and Panagia, N. 1998, On the evolution of the cosmic supernova rates, *MNRAS* **297**, L17+.

Maiolino, R., Vanzi, L., Mannucci, F., Cresci, G. *et al.* 2002, Discovery of two infrared supernovae: A new window on the SN search, *A&A* **389**, 84.

Marchili, N., Martí-Vidal, I., Brunthaler, A., Krichbaum, T. P. *et al.* 2010, The radio lightcurve of SN 2008iz in M82 revealed by Urumqi observations, *A&A* **509**, A47+.

Mattila, S. and Kankare, E. 2010, Supernova 2010P in Arp 299, *Central Bureau Electronic Telegrams* **2145**, 1.

Mattila, S., Kankare, E., Datson, J. and Pastorello, A. 2010, Supernovae 2010O and 2010P, *Central Bureau Electronic Telegrams* **2149**, 1.

Mattila, S. and Meikle, W. P. S. 2001, Supernovae in the nuclear regions of starburst galaxies, *MNRAS* **324**, 325.

Mattila, S., Monard, L. A. G. and Li, W. 2005, Supernovae 2005Q, 2005R, 2005S, 2005T, 2005U, *IAU Circ.* **8473**, 2.

Mattila, S., Väisänen, P., Farrah, D., Efstathiou, A. *et al.* 2007, Adaptive Optics Discovery of Supernova 2004ip in the Nuclear Regions of the Luminous Infrared Galaxy IRAS 18293-3413, *ApJL* **659**, L9.

Minkowski, R. 1941, Spectra of Supernovae, *Public. of the Astron. Soc. Pac.* **53**, 224.

Miyoshi, M., Moran, J., Herrnstein, J., Greenhill, L. *et al.* 1995, Evidence for a black hole from high rotation velocities in a sub-parsec region of NGC4258, *Nature* **373**, 127.

Modjaz, M., Kirshner, R., Challis, P. and Berlind, P. 2005, Supernova 2005U in Arp 299, *IAU Circ.* **8475**, 2.

Momjian, E., Romney, J. D., Carilli, C. L., Troland, T. H. *et al.* 2003, Very Long Baseline Array Continuum and H I Absorption Observations of the Ultraluminous Infrared Galaxy IRAS 17208-0014, *ApJ* **587**, 160.

Montes, M. J., Weiler, K. W., Van Dyk, S. D., Panagia, N. *et al.* 2000, Radio Observations of SN 1979C: Evidence for Rapid Presupernova Evolution, *ApJ* **532**, 1124.

Moustakas, J., Kennicutt, Jr., R. C. and Tremonti, C. A. 2006, Optical Star Formation Rate Indicators, *ApJ* **642**, 775.

Murphy, E. J., Condon, J. J., Schinnerer, E., Kennicutt, R. C. *et al.* 2011, Calibrating Extinction-free Star Formation Rate Diagnostics with 33 GHz Free-free Emission in NGC 6946, *ApJ* **737**, 67.

Nagar, N. M., Falcke, H., Wilson, A. S. and Ulvestad, J. S. 2002, Radio sources in low-luminosity active galactic nuclei. III. "AGNs" in a distance-limited sample of "LLAGNs", *A&A* **392**, 53.

Neff, S. G., Ulvestad, J. S. and Teng, S. H. 2004, A Supernova Factory in the Merger System Arp 299, *ApJ* **611**, 186.

Neugebauer, G., Habing, H. J., van Duinen, R., Aumann, H. H. *et al.* 1984, The Infrared Astronomical Satellite (IRAS) mission, *ApJL* **278**, L1.

Newton, J., Puckett, T. and Orff, T. 2010, Supernova 2010O in NGC 3690, *Central Bureau Electronic Telegrams* **2144**, 2.

Osorio, M. 2000, *Hot Molecular Cores and the Formation of Massive Stars*, PhD thesis, Instituto de Astronomia, UNAM Apartado Postal 3-72 (Xangari) 58089 Morelia Michoacan Mexico.

Pacholczyk, A. G. 1970, *Radio Astrophysics: Nonthermal processes in galactic and extra-galactic sources*, W. H. Freeman and Company.

Panagia, N., Van Dyk, S. D., Weiler, K. W., Sramek, R. A. *et al.* 2006, A Search for Radio Emission from Type Ia Supernovae, *ApJ* **646**, 369.

Parra, R., Conway, J. E., Aalto, S., Appleton, P. N. *et al.* 2010, COLA. III. Radio Detection of Active Galactic Nucleus in Compact Moderate Luminosity Infrared Galaxies, *ApJ* **720**, 555.

Parra, R., Conway, J. E., Diamond, P. J., Thrall, H. *et al.* 2007, The Radio Spectra of the Compact Sources in Arp 220: A Mixed Population of Supernovae and Supernova Remnants, *ApJ* **659**, 314.

Peeters, E., Spoon, H. W. W. and Tielens, A. G. G. M. 2004, Polycyclic Aromatic Hydrocarbons as a Tracer of Star Formation?, *ApJ* **613**, 986.

Pereira-Santaella, M., Diamond-Stanic, A. M., Alonso-Herrero, A. and Rieke, G. H. 2010, The Mid-infrared High-ionization Lines from Active Galactic Nuclei and Star-forming Galaxies, *ApJ* **725**, 2270.

Pérez-Torres, M., Romero, C., Alberdi, A., Colina, L. *et al.* 2008, Supernova 2008cs in IRAS 17138-1017, *Central Bureau Electronic Telegrams* **1392**, 2.

Pérez-Torres, M. A., Alberdi, A., Colina, L., Torrelles, J. M. *et al.* 2009a, Radio monitoring of NGC 7469: late-time radio evolution of SN 2000ft and the circumnuclear starburst in NGC 7469, *MNRAS* **399**, 1641.

Pérez-Torres, M. A., Alberdi, A., Romero-Cañizales, C. and Bondi, M. 2010, Serendipitous discovery of the long-sought active galactic nucleus in Arp 299-A, *A&A* **519**, L5+.

Pérez-Torres, M. A., Mattila, S., Alberdi, A., Colina, L. *et al.* 2007, Radio Detection of Supernova 2004ip in the Circumnuclear Region of the Luminous Infrared Galaxy IRAS 18293-3413, *ApJL* **671**, L21.

Pérez-Torres, M. A., Romero-Cañizales, C., Alberdi, A. and Polatidis, A. 2009b, An extremely prolific supernova factory in the buried nucleus of the starburst galaxy IC 694, *A&A* **507**, L17.

Pérez-Torres, M. A. and Alberdi, A. 2007, Radio emission from the Sy 1.5 galaxy NGC 5033, *MNRAS* **379**, 275.

Pindao, M., Schaerer, D., González Delgado, R. M. and Stasińska, G. 2002, VLT observations of metal-rich extra galactic H II regions. I. Massive star populations and the upper end of the IMF, *A&A* **394**, 443.

Polatidis, A. G. and Aalto, S. 2001, Atomic and molecular gas in the merger Arp 299, in R. T. Schilizzi (editor), *Galaxies and their Constituents at the Highest Angular Resolutions*, vol. 205 of *IAU Symposium*, pp. 198–+.

Prosperi, E. 1999, Supernovae 1998es and 1999D, *IAU Circ.* **7094**, 2.

Qiu, Y. L., Qiao, Q. Y., Hu, J. Y. and Li, W. 1999, Supernova 1999D in NGC 3690, *IAU Circ.* **7088**, 2.

Ramolla, M., Haas, M., Bennert, V. N. and Chini, R. 2011, Megamaser detection and nuclear obscuration in Seyfert galaxies, *A&A* **530**, A147+.

Rastorgueva, E. A., Wiik, K. J., Bajkova, A. T., Valtaoja, E. *et al.* 2011, Multi-frequency VLBA study of the blazar S5 0716+714 during the active state in 2004. II. Large-scale jet kinematics and the comparison of the different methods of VLBI data imaging as applied to kinematic studies of AGN, *A&A* **529**, A2+.

Readhead, A. C. S. 1994, Equipartition brightness temperature and the inverse Compton catastrophe, *ApJ* **426**, 51.

Robitaille, T. P. and Whitney, B. A. 2010, The Present-Day Star Formation Rate of the Milky Way Determined from Spitzer-Detected Young Stellar Objects, *ApJL* **710**, L11.

Rohlfs, K. and Wilson, T. 2004, *Tools of Radio Astronomy*, Germany: Springer−Verlag, 4$^{\text{th}}$ ed.

Romero-Canizales, C., Pérez-Torres, M. A. and Alberdi, A. 2008, EVN observations of the Ultra Luminous Infrared Galaxies IRAS 23365+3604 and IRAS07251-0248, in *The role of VLBI in the Golden Age for Radio Astronomy*.

Romero-Cañizales, C., Mattila, S., Alberdi, A., Pérez-Torres, M. A. *et al.* 2011, The core-collapse supernova rate in Arp 299 revisited, *MNRAS* **415**, 2688.

Rosa-González, D., Terlevich, E. and Terlevich, R. 2002, An empirical calibration of star formation rate estimators, *MNRAS* **332**, 283.

Ryder, S., Kankare, E. and Mattila, S. 2010a, Supernova 2010cu in IC 883 = Psn K1002-1, *Central Bureau Electronic Telegrams* **2286**, 1.

Ryder, S., Mattila, S., Kankare, E. and Pérez-Torres, M. A. 2010b, Supernova 2010P, *Central Bureau Electronic Telegrams* **2189**, 1.

Salpeter, E. E. 1955, The Luminosity Function and Stellar Evolution., *ApJ* **121**, 161.

Sanders, D. B., Mazzarella, J. M., Kim, D., Surace, J. A. *et al.* 2003, The IRAS Revised Bright Galaxy Sample, *AJ* **126**, 1607.

Sanders, D. B. and Mirabel, I. F. 1996, Luminous Infrared Galaxies, *Annual Review of Astronomy and Astrophysics* **34**, 749.

Sanders, D. B., Soifer, B. T., Elias, J. H., Neugebauer, G. *et al.* 1988, Warm ultraluminous galaxies in the IRAS survey - The transition from galaxy to quasar?, *ApJL* **328**, L35.

Scoville, N. Z., Evans, A. S., Thompson, R., Rieke, M. *et al.* 2000, NICMOS Imaging of Infrared-Luminous Galaxies, *AJ* **119**, 991.

Shepherd, M. C., Pearson, T. J. and Taylor, G. B. 1995, DIFMAP: an interactive program for synthesis imaging., in B. J. Butler & D. O. Muhleman (editor), *Bulletin of the American Astronomical Society*, vol. 27 of *Bulletin of the American Astronomical Society*, pp. 903–+.

Shlosman, I., Begelman, M. C. and Frank, J. 1990, The fuelling of active galactic nuclei, *Nature* **345**, 679.

Smartt, S. J. 2009, Progenitors of Core-Collapse Supernovae, *Annual Review of Astronomy and Astrophysics* **47**, 63.

Smith, D. A., Herter, T., Haynes, M. P., Beichman, C. A. *et al.* 1995, The luminous starburst galaxy UGC 8387, *ApJ* **439**, 623.

Smith, H. E., Lonsdale, C. J. and Lonsdale, C. J. 1998a, The Starburst-AGN Connection. II. The Nature of Luminous Infrared Galaxies as Revealed by VLBI, VLA, Infrared, and Optical Observations, *ApJ* **492**, 137.

Smith, H. E., Lonsdale, C. J., Lonsdale, C. J. and Diamond, P. J. 1998b, A Starburst Revealed—Luminous Radio Supernovae in the Nuclei of ARP 220, *ApJL* **493**, L17.

Smith, N., Li, W., Filippenko, A. V. and Chornock, R. 2011, Observed fractions of core-collapse supernova types and initial masses of their single and binary progenitor stars, *MNRAS* **412**, 1522.

Smith, N., Li, W., Foley, R. J., Wheeler, J. C. *et al.* 2007, SN 2006gy: Discovery of the Most Luminous Supernova Ever Recorded, Powered by the Death of an Extremely Massive Star like η Carinae, *ApJ* **666**, 1116.

Soifer, B. T., Neugebauer, G. and Houck, J. R. 1987, The IRAS view of the extragalactic sky, *Annual Review of Astronomy and Astrophysics* **25**, 187.

Soifer, B. T., Neugebauer, G., Matthews, K., Egami, E. *et al.* 2001, High-Resolution Mid-Infrared Imaging of Infrared-Luminous Starburst Galaxies, *AJ* **122**, 1213.

Soifer, B. T., Rowan-Robinson, M., Houck, J. R., de Jong, T. *et al.* 1984, Infrared galaxies in the IRAS minisurvey, *ApJL* **278**, L71.

Sopp, H., Alexander, P. and Riley, J. 1990, Binary Starbursts in Normal and Colour Selected IRAS Galaxies, *MNRAS* **246**, 143.

Tarchi, A., Castangia, P., Henkel, C. and Menten, K. M. 2007, The water megamaser in the merger system Arp 299, *New Astronomy Review* **51**, 67.

Tarchi, A., Castangia, P., Henkel, C., Surcis, G. *et al.* 2011, New H_2O masers in Seyfert and FIR bright galaxies. IV. Interferometric follow-ups, *A&A* **525**, A91+.

Tarchi, A., Neininger, N., Greve, A., Klein, U. *et al.* 2000, Radio supernovae, supernova remnants and H bt II regions in NGC 2146 observed with MERLIN and the VLA, *A&A* **358**, 95.

Terashima, Y. and Wilson, A. S. 2003, Chandra Snapshot Observations of Low-Luminosity Active Galactic Nuclei with a Compact Radio Source, *ApJ* **583**, 145.

Thompson, A. R., Moran, J. M. and Swenson Jr., G. W. 2004, *Interferometry and Synthesis in Radio Astronomy*, Wiley-VCH Verlag GmbH & Co. KGaA, Germany, 2nd ed.

Treffers, R. R., Leibundgut, B., Filippenko, A. V. and Richmond, M. W. 1993, Supernova 1993G in NGC 3690, *IAU Circ.* **5718**, 1.

Tsvetkov, D. Y. 1994, Observations of supernovae 1992G, 1992H, and 1993G, *Astronomy Letters* **20**, 374.

Turatto, M. 2003, Classification of Supernovae, in K. Weiler (editor), *Supernovae and Gamma-Ray Bursters*, vol. 598 of *Lecture Notes in Physics, Berlin Springer Verlag*, pp. 21–36.

Ulvestad, J. S. 2009, Radio Emission from Young Supernovae and Supernova Remnants in Arp 299, *AJ* **138**, 1529.

van Buren, D., Jarrett, T., Terebey, S., Beichman, C. *et al.* 1994, Supernova 1992bu in NGC 3690, *IAU Circ.* **5960**, 2.

van Dyk, S. D., Weiler, K. W., Sramek, R. A. and Panagia, N. 1993, SN 1988Z: The Most Distant Radio Supernova, *ApJL* **419**, L69+.

Veilleux, S., Kim, D.-C., Sanders, D. B., Mazzarella, J. M. *et al.* 1995, Optical Spectroscopy of Luminous Infrared Galaxies. II. Analysis of the Nuclear and Long-Slit Data, *ApJS* **98**, 171.

Veron, P., Goncalves, A. C. and Veron-Cetty, M.-P. 1997, AGNs with composite spectra., *A&A* **319**, 52.

Weidner, C. and Kroupa, P. 2004, Evidence for a fundamental stellar upper mass limit from clustered star formation, *MNRAS* **348**, 187.

Weiler, K. W., Panagia, N., Montes, M. J. and Sramek, R. A. 2002, Radio Emission from Supernovae and Gamma-Ray Bursters, *Annual Review of Astronomy and Astrophysics* **40**, 387.

Weiler, K. W. and Sramek, R. A. 1988, Supernovae and supernova remnants, *Annual Review of Astronomy and Astrophysics* **26**, 295.

Weingartner, J. C. and Draine, B. T. 2001, Dust Grain-Size Distributions and Extinction in the Milky Way, Large Magellanic Cloud, and Small Magellanic Cloud, *ApJ* **548**, 296.

Wilson, A. S., Helfer, T. T., Haniff, C. A. and Ward, M. J. 1991, The starburst ring around the Seyfert nucleus in NGC 7469, *ApJ* **381**, 79.

Wood, D. O. S. and Churchwell, E. 1989, The morphologies and physical properties of ultracompact H II regions, *ApJS* **69**, 831.

Yamaoka, H., Kato, T., Filippenko, A. V., van Dyk, S. D. *et al.* 1998, Supernova 1998T in NGC 3690, *IAU Circ.* **6859**, 1.

Yuan, T.-T., Kewley, L. J. and Sanders, D. B. 2010, The Role of Starburst-Active Galactic Nucleus Composites in Luminous Infrared Galaxy Mergers: Insights from the New Optical Classification Scheme, *ApJ* **709**, 884.

Yun, M. S., Reddy, N. A. and Condon, J. J. 2001, Radio Properties of Infrared-selected Galaxies in the IRAS 2 Jy Sample, *ApJ* **554**, 803.

Zezas, A., Ward, M. J. and Murray, S. S. 2003, Chandra Observations of the X-Ray-luminous Star-forming Galaxy Merger Arp 299, *ApJL* **594**, L31.